

UC Riverside

UC Riverside Electronic Theses and Dissertations

Title

Ultraviolet Communication Network Modeling and Analysis

Permalink

<https://escholarship.org/uc/item/8n04x3q6>

Author

Wang, Leijie

Publication Date

2011

Peer reviewed|Thesis/dissertation

UNIVERSITY OF CALIFORNIA
RIVERSIDE

Ultraviolet Communication Network Modeling and Analysis

A Dissertation submitted in partial satisfaction
of the requirements for the degree of

Doctor of Philosophy

in

Electrical Engineering

by

Leijie Wang

August 2011

Dissertation Committee:

Dr. Zhengyuan Xu, Chairperson
Dr. Albert Wang
Dr. Jianlin Liu

The Dissertation of Leijie Wang is approved:

Committee Chairperson

University of California, Riverside

Acknowledgments

Though I am the only author of this dissertation, a great many people have contributed to its production. I would like to thank all those people who have made this dissertation possible and because of whom my graduate experience has been one that I will cherish forever.

My deepest gratitude is to my advisor, Professor Zhengyuan Xu. I have been amazingly fortunate to have an advisor who gave me the freedom to explore on my own, and in the meantime the guidance when I felt lost. He taught me how to think with questions and express ideas. His patience and support helped me overcome many crisis situations and finish this dissertation.

I am grateful to the members of my doctoral committee, Professor Albert Wang and Professor Jianlin Liu, for reading the drafts of this dissertation and providing valuable comments and suggestions that improved the presentation and content of this dissertation.

Dr. Srikanth V. Krishnamurthy's insightful guidance and constructive criticisms at different stages of my research were thought-provoking and they helped me step in a new area. I am grateful to him for setting a high bar in research for me and helping me achieve it, and thus teaching me how to do research.

I am also thankful to Dr. Brian M. Sadler in the Army Research Lab (ARL) for his various forms of support, input and feedback on my research.

I would like to acknowledge all the members of the research group, Dr. Gang Chen, Dr. Ning Liu, Qunfeng He, Haipeng Ding, Kaiyun Cui, Zongyu Dong and Bo Bai, for their friendship, numerous discussions, and help on field experiments on a great many cold weekend nights.

Many friends have helped me stay sane through these difficult years. Their support and care helped me overcome setbacks and stay focused on my graduate study. I greatly value their friendship and I deeply appreciate their belief in me.

Most importantly, none of this would have been possible without the love and patience of my family. I especially thank my mother, Lihua Sun, for her continuous support and understanding for almost thirty years. My family to whom this dissertation is dedicated to, has been a constant source of love, concern, support and strength all these years. Last, but not the least, I would like to express my heart-felt gratitude to my wife, Yiyang Li. I warmly appreciate the generosity and understanding from her for the past six years.

To my family.

ABSTRACT OF THE DISSERTATION

Ultraviolet Communication Network Modeling and Analysis

by

Leijie Wang

Doctor of Philosophy, Graduate Program in Electrical Engineering
University of California, Riverside, August 2011
Dr. Zhengyuan Xu, Chairperson

With recent advances in ultraviolet (UV) sources and detectors, UV communication and networking has received increasing interest for diverse applications. This thesis studies corresponding non-line-of-sight (NLOS) scattering channels, UV system and network performance, neighbor discovery and network connectivity issues.

Based on NLOS communication link geometry and UV signal interaction with the atmosphere, the author develops two analytical channel models that describe the path loss in an integral form and closed-form respectively. Utilizing curve-fitting with field measurements, an easy-to-use empirical model is further developed. The results are then applied to study performance of a NLOS UV network, from outage probability to transmission throughput and network connectivity in a multi-user interference environment. Different UV transceiver structures and pointing geometry are incorporated, and fundamental relations of network k-connectivity with network parameters such as network scale and node density are studied. Subsequently, a neighbor discovery protocol for UV communication networks is proposed, using a novel handshake mechanism and direction synchronization technique. The protocol is further improved in terms of significantly reduced neighbor discovery time by assigning a leader node for node coordination. Meanwhile, the author also investigates the effects of channel delay spread on

communication quality, i.e., data rate limitation from the induced self inter-symbol interference. These analyses and results provide valuable guidance for UV system and network design in a real environment.

Contents

List of Figures	xi
List of Tables	xiii
1 Introduction	1
1.1 Background	1
1.1.1 UV Transmission Devices	2
1.1.2 UV Detection Devices	4
1.1.3 UV Communication Modulation Schemes	4
1.1.4 UV Channel Modeling	6
1.2 Motivations	7
1.3 Contributions and Outline of the Thesis	7
2 Non-Line-of-Sight Ultraviolet Link Loss in Non-Coplanar Geometry	9
2.1 An Analytical Single Scattering Model with Receiver Vertical Pointing	11
2.1.1 Introduction	11
2.1.2 Development	11
2.1.3 Numerical Results	17
2.2 An Approximate Closed-form Single Scattering Model with Arbitrary Pointing	18
2.2.1 Introduction	18
2.2.2 Development	19
2.2.3 Numerical Results	24
2.3 An Empirical Model Incorporating Multiple Scattering	25
2.4 Full Link Duplexing	28
2.5 Summary	30
3 Performance of LED-Based M-PPM Receivers in NLOS Delay Spread Channels	33
3.1 Introduction	34
3.2 System Architecture and NLOS UV Communication System Model	34
3.2.1 System Architecture	34
3.2.2 System Model	34
3.3 Performance of PMT Based Receivers without ISI	35
3.4 Performance of PMT Based Receivers with ISI	37
3.5 Numerical Analysis	40
3.6 Summary	41

4	Wireless UV Network Models and Performance in Non-coplanar Geometry	43
4.1	Introduction	43
4.2	Channel Model	45
4.3	Network Model	45
4.3.1	Stochastic Geometry	45
4.3.2	Distribution of Distance and Off-axis Angle	46
4.4	Network Performance	46
4.4.1	Outage Probability	47
4.4.2	Transmission Throughput	48
4.5	Numerical Results	49
4.6	Summary	53
5	A Leadership-based Neighbor Discovery Protocol for UV Wireless Networks	54
5.1	Introduction	54
5.2	Related work	56
5.3	UV Communication Link and Transceiver Models	57
5.4	Leadership-based Neighbor Discovery Protocol	58
5.5	Improving fairness	65
5.6	Termination of Neighbor Discovery	74
5.7	Summary	77
6	Connectivity of Wireless Ultraviolet Networks	79
6.1	Introduction	80
6.2	Path Loss and Network Models	81
6.2.1	Path Loss Model	82
6.2.2	Distribution of Node Location	83
6.2.3	Distribution of Distance and Off-axis Angle	83
6.3	Connectivity Modeling	84
6.3.1	Scenario I	85
6.3.2	Scenario II	90
6.3.3	Scenario III	94
6.3.4	Scenario IV	96
6.4	Summary	99
7	Conclusions	100
	Bibliography	102

List of Figures

1.1	Optical wavelength range.	2
1.2	Potential application scenarios.	3
2.1	UV NLOS communication system model in coplanar geometry.	10
2.2	System geometry and ray pointing.	12
2.3	Path loss per cm^2 versus off-axis angle.	18
2.4	(a) The transmit beam and receiver FOV intersection changes as the Tx beam deviates from a coplanar geometry; (b) The relationship between ϕ'_1 and α . . .	20
2.5	Coordinate system rotation.	22
2.6	Comparison of proposed model and model [1].	25
2.7	Common (overlap) volume between transmission beam and receiving FOV [2].	26
2.8	Exponential curve fitting (FOV, beam angle and pointing angle).	27
2.9	Exponential curve fitting (Geometry: pointing angle 15° , distance 15m). . . .	29
2.10	An illustration of off-axis angle ϕ . Tx represents a transmitter with four directions; Rx represents an omni-directional receiver.	30
2.11	The impact of the pointing angle on off-axis angle exponent factor b (distance 30m).	31
2.12	The impact of distance on off-axis angle exponent factor b (pointing angle 30°).	31
2.13	Illustration of constraints on the pointing angle at different distance to achieve full-duplex.	32
3.1	UV NLOS communication system model in coplanar geometry.	35
3.2	Impulse responses of a UV NLOS channel in four different transmit/receive geometries at 100m.	36
3.3	BER performance of 4-PPM receiver in ISI NLOS UV channel.	41
3.4	BER versus Power in both ISI and non-ISI NLOS UV channel with 4PPM employed.	42
4.1	Transmission throughput and its lower bound against β for given λ and p	50
4.2	Normalized lower bound of transmission throughput and outage probability against λ for given β and p	51
4.3	Normalized lower bound of transmission throughput and outage probability against p for given λ and β	51
5.1	A UV transceiver with 4 (left) and 6 (right) transmission directions. Dots on the side facets are the directional LED transmitters; each dot on the top facet is the omni-directional photon receiver.	58

5.2	Comparison between leadership-based algorithm and credit-collection algorithm proposed in [3].	65
5.3	Comparison between schemes with or without fairness consideration.	71
5.4	The time taken for neighbor discovery varies with number of nodes. The time shown is when 95% of neighbors are discovered.	72
5.5	The time taken for neighbor discovery varies with number of nodes – a comparison of the leadership-based algorithm and the credit-collection algorithm. The time shown is when 70% of the neighbors are discovered, on average.	73
5.6	Performance with different numbers of directions. 20 nodes in total are distributed in the network.	74
5.7	Illustrating the termination process. Solid line shows how the percentage of discovered neighbors increases with time; ‘*’s represent the instances when the node starts serving as the leader.	76
5.8	Illustration of the performance of the termination process with different node densities. All the nodes in the network find 100% of their neighbors.	78
6.1	$\Pr[d_{min} > k]$ versus node density λ with OOK modulation in Scenario I.	89
6.2	Effect of transmission probability on $\Pr[d_{min} > k]$ in Scenario I.	90
6.3	$\Pr[d_{min} > k]$ versus node density λ with OOK modulation in both Scenarios I and II.	93
6.4	The shape of the coverage area with Tx pointing angle 60°	95
6.5	$\Pr[d_{min} > k]$ versus node density λ with OOK modulation in Scenarios I, II and III.	96
6.6	$\Pr[d_{min} > k]$ versus N_t with OOK modulation.	98

List of Tables

2.1	Experimental settings	28
4.1	Parameters settings for numerical evaluation	50
5.1	Parameters settings in simulations	64
5.2	Records of being the leader (time length = 3 secs)	66
5.3	Records of being the leader (time length = 0.54 secs)	67
5.4	Records of being the leader (time length = 3 secs)	69
5.5	Records of being the leader (time length = 0.42 secs)	70
5.6	Leader records after finding 100% neighbors	77
6.1	Scenario I parameter settings	88
6.2	Scenario II parameter settings	92

Chapter 1

Introduction

1.1 Background

In the 1960's and 1970's, ultraviolet (UV) communication was explored by [4, 5]. Then the research became stagnant due to limitations of devices. The available UV sources at that time could not meet the need of potential applications because of their large size, high power consumption and unaffordable cost. Thanks to DARPA's SUVOS program launched in 2002, small size, low power and low cost UV LEDs were developed recently. This progress revived UV communication research and enriched UV applications in other areas as well such as sensing and water purification.

The UV spectrum is huge and unregulated. It can be divided into three regions as shown in Figure 1.1, from 10 nm to 280 nm named by UVC, from 280 nm to 320 nm called by UVB and from 320 nm to 400 nm referred as UVA. Within UVC, a section between 200 nm and 280 nm is defined as the solar blind section. In this band, most of solar radiation is absorbed by the ozone layer in the upper atmosphere, leading to a nearly zero background noise condition for UV communication. Utilizing this property, we can adopt detectors with relatively large field-of-view (FOV) without introducing high background noise like in traditional infrared communication.

Meanwhile, UV photons, once emitted from a UV source, interact with molecules and aerosols in the atmosphere intensively along their path to a receiver. The strong scattering effect results in the feasibility of NLOS communication on-the-move. This distinguishes UV communication from infrared communication which typically requires alignment between a transmitter (Tx) and receiver (Rx). Due to this useful feature, communication is feasible even when a line-of-sight (LOS) link does not exist. Much relaxed pointing of a Tx to a Rx allows easy network configuration in diverse settings. For example, in forest or a metropolitan environment, UV communication is capable of maintaining a reliable link between nodes. Meanwhile, various degrees of freedom from pointing provide significant spatial diversity and channel reuse. On the other hand, the strong absorption in the UV band ensures secured communication within a predefined area since the detector beyond certain physical distance is difficult to receive the signal. With above advantages, the UVC spectrum becomes a valuable resource for many applications (refer to Figure 1.2) in the civilian and military domains [6, 7, 8], like environment sensing, unattended ground sensor networks, and inter-soldier communication in a battlefield.

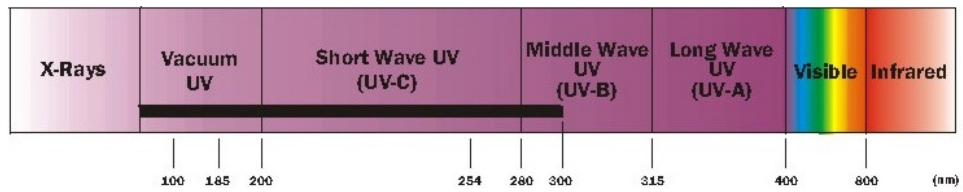


Figure 1.1: Optical wavelength range.

1.1.1 UV Transmission Devices

Mercury lamp, solid state laser, laser diode, and light emitting diode (LED) are typical types of UV sources. Most early prototypes employed mercury lamp as the source which has moderately high optical power, but it is fragile, sensitive to temperature variation, has high



Figure 1.2: Potential application scenarios.

power consumption, low modulation rate and short lifetimes [9]. UV solid state laser can provide high peak optical power, narrow spectral width, and a narrow beam. However, it is relatively expensive, power hungry, bulky, and requires optical lens to diverge beam if wide beam angle is needed. UV laser diode is a small semiconductor device, and has a high modulation rate. But it still remains in the research stage, and no commercial products are available. For different lasers, safety regulation is more restrictive due to their narrow beam and high peak power. Thanks to DARPA SUVOS program initiated in 2002, a variety of UV LED sources are commercially available since then. They are of low power consumption and small size. The current commercial LED source supports up to 50 MHz modulation bandwidth. The drawback of a LED is that its average transmission power and power efficiency are low. The power however can be increased using a arrayed packaging of multiple LED chips, bringing up to 100mW even though each LED can only provide up to 0.5mW optical power. Therefore, a UV laser or a LED array could be employed for long distance free-space UV communication, while LEDs are good transmitters for short-range NLOS communication with much relaxed safety require-

ments. Most link measurements and demo systems including the one adopted in this research are based on deep UV LEDs.

1.1.2 UV Detection Devices

To date, two mainstream photodetectors are photomultiplier tube (PMT) and avalanche photodiode (APD). The parameters that are important to the evaluation of the performance of photodetectors are detection area, responsivity, gain, quantum efficiency, bandwidth, dark current and dark count. PMTs have large detection area (on the order of several cm^2) and high multiplication gains up to 10^7 . The bandwidth is roughly 50 MHz, corresponding to response time of 20 ns. Dark current and dark count are also very low. APD is an alternative choice of photodetector. The detection area and gain of APD are relatively small compared to those of PMT, but it has much higher bandwidth and quantum efficiency and also single photon sensitivity [10]. PMT is relatively more mature than APD which is currently only available in specialized application test such that most current experiments and demo systems are based on PMTs. We believe more and more advanced APDs will become commercially available after the completion of DARPA's Deep Ultraviolet Avalanche Photodetectors (DUVAP) program in the near future.

1.1.3 UV Communication Modulation Schemes

There are various modulation techniques in radio frequency (RF) communications. However, only limited choices can be made towards UV communication due to the following reasons. At present, the optical spectrum of the signals emitted by UV LEDs is relatively wide, so carrier modulation is not applicable. As such, the UV communication can be considered as baseband communication. LEDs emit non-coherent unipolar optical signal, different from that in RF communication. The output of a photodetector is proportional to the power of received

optical signal. Thus this energy-based reception cannot capture the phase information of the signal. Therefore, the most viable modulation/detection scheme in UV communication is intensity modulation and direction detection (IM/DD) [11].

Several possible modulation schemes are discussed by Kahn and Barry in infrared communication. They are on-off keying (OOK), pulse-position modulation (PPM) and binary phase shift keying (BPSK) subcarrier [11]. Popoola and Ghassemlooy further discussed BPSK subcarrier intensity modulation (SIM) in free-space optical communication using laser diode [12]. Since optical signal cannot be negative, a DC is required to make sure the driving current of a laser diode always be greater than zero. This scheme may not be appropriate when a UV LED source is adopted because of the limited power by a LED. The major considerations in choosing an appropriate modulation scheme are bandwidth, data rate, and power requirement. The simplest intensity modulation is OOK which uses two quantization levels to represent bit "0" and bit "1". More quantization levels can be employed but with a higher signal-to-noise ratio (SNR) requirement. In general, higher transmission power will lead to better BER performance. However, NLOS UV link path loss is very high [2], causing difficulties in achieving satisfied performance with OOK modulation. At the detector side, OOK signal requires a threshold-based decision scheme to detect where the optimal threshold needs to be adapted to SNR. This requirement results in a complex receiver design [13, 14]. Meanwhile, a possibly long zero data stream may cause the receiver to lose synchronization. PPM allows low average power and high peak power which agree with the characteristics of a LED. PPM transmits information by allocating a pulse in a time slot of a symbol interval. It always ensures one pulse is transmitted in each symbol, thus time synchronization becomes easier. The order of PPM can be adjusted to adaptively accommodate different channel conditions. Signal detection can rely on a ML detector to achieve optimal performance easily [15].

1.1.4 UV Channel Modeling

In the beginning of rebirth of UV communication research, Shaw et al. made valuable contributions to this field from concept introduction, link measurement, testbed implementation to performance evaluation and range extension [16, 17, 18, 19, 20, 9]. Kedar analyzed multiple access interference in a NLOS UV sensor network [21]. Chen et al. further evaluated LED-based UV communication links experimentally [10, 2].

Reilly derived a single scattering UV path loss model analytically in [4] and an impulse response model in [22] using a prolate-spheroidal coordinate system. The results were evaluated numerically. Xu et al. made a high-fidelity approximation to attain a closed-form solution [23]. The model was further extended to accommodate multiple scattering events for sensor network and communication channel modeling [2, 24, 25], similar to backscattering lidar [26]. Ding et al. proposed a parametric single scattering channel model for both impulse response and path loss [27].

All above channel models assumed a coplanar geometry in which transmitter beam axis and receiver FOV axis are on the same plane. In most application scenarios, each communication unit connects with others in a network manner, either centralized or ad hoc. Considering a network with multiple nodes, it is reasonable to assume that transmitters point to intended receivers to achieve a high SNR, i.e., transmitters and receivers are coplanar. It is however not plausible to require an interferer also to point to the receiver. Thus, usually the intended receiver and interference transmitters are in non-coplanar geometry. It is of interest to develop UV channel models in non-coplanar geometry.

1.2 Motivations

NLOS UV communication technology by atmospheric scattering is promising for civilian and military applications [8]. The leading motivation of the research of UV communication is to find out a systematic solution to realize high-quality communication. Specifically, accurate prediction of link loss is the basis of system design. For system and network analysis, the link loss models in very simple forms are desirable and thus developed in this work. One of the most promising applications of UV communications is, for example, ad hoc sensor network. The throughput evaluates the network capability in information exchange and is studied in this thesis. Before a network is operational, the nodes in the network should have knowledge about their neighbor nodes. This requires proper neighbor discovery protocols to be implemented. Thus the thesis presents two neighbor discovery protocols to solve this issue. Moreover, before nodes discover their neighbors, how well the network is connected potentially should be investigated. Otherwise, if two nodes are out of the transmission range of each other, even the best neighbor discovery protocol cannot make them connected directly. Therefore, the thesis also investigates the connectivity issue for UV networks and reveals how it heavily depends on different choices of transceiver design and other system parameters.

1.3 Contributions and Outline of the Thesis

The thesis consists of six chapters and the rest chapters are organized as follows:

Chapter 2 develops three channel models for NLOS UV communications. The first model is an analytical path loss model which extends an existing coplanar geometry model into the non-coplanar geometry scenario. The second model relaxes the assumption to be applicable to a more general scenario in which both transmitter and receiver can orient to any directions. The model is developed to a simplified form without multiple integrals such that the computa-

tional complexity is much lower. The last proposed model is an empirical model which reflects multiple scattering effects under the non-coplanar geometry assumption as well. The form of this model is much simpler than the previous two, and is particularly appropriate for further of system and network design and performance assessment rather than link budget prediction only.

Chapter 3 analyzes the effect of channel delay spread on receiver performance. To the best of my knowledge, all the previous literatures ignore the effect of channel introduced inter-symbol interference (ISI) in UV communication. The thesis incorporates ISI effect into link performance evaluation and shows how data rate and transmission power affect bit error rate (BER).

Chapter 4 investigates the throughput of UV communication network and studies how three important factors, nodes spatial density, transmission probability and modulation scheme, affect the throughput.

Chapter 5 first briefly introduces a credit-collection based neighbor discovery protocol, which was co-designed by the author, and then develops a novel leadership based neighbor discovery protocol, which provide full knowledge for each node about its neighbor nodes more efficiently and effectively.

Chapter 6 investigates the connectivity issue of UV networks. Different transceiver designs lead to different interference patterns. Thus this chapter studies how the connectivity probability varies with transceiver structure.

Chapter 2

Non-Line-of-Sight Ultraviolet Link

Loss in Non-Coplanar Geometry

Link modeling for NLOS UV communications is fundamental for system and network design, and performance analysis. However, modeling NLOS atmospheric scattering is challenging, and complicated by the need to include optical link geometry and atmospheric conditions. The UV photons undergo atmospheric scattering. A point of view is that the photons may be only scattered once between reaching the Rx. This case is called single scattering. When the optical length, which is defined as the product of actual distance between the Tx and Rx and scattering coefficient, is relatively short, single scattering assumption is a reasonable approximation [2]. As optical length grows, multiple scattering occurs and its effects may become dominant, in which photons are scattered more than once.

If Tx and Rx point to each other, i.e., the transmission beam axis and the Rx FOV axis are on the same plane, this geometry is named as coplanar geometry. Coplanar path loss models have been developed in the literature. Reilly et al. proposed a single scattering analytical model

in a prolate-spheroidal coordinate system [22, 28], and Xu et al. made a high-fidelity approximation to attain a closed-form solution [23]. The model was further extended to accommodate multiple scattering events for communications channel modeling [2, 24], similar to backscattering lidar [26]. However, sometimes Tx and Rx are not in coplanar geometry because of a pointing error or limited tracking ability. Meanwhile, the interference nodes typically would not be in coplanar geometry with the Rx of interest. Thus for network research, the model developed based on the coplanar geometry assumption is inadequate. It is of interest to generalize to non-coplanar transmit and receive pointing, e.g., in the context of mobile ad hoc or multi-user communications.

Figure 2.1 depicts the transmit/receive geometry and the block diagram of a UV communication system which is composed of a modulator, LED array, channel, photodetector, integrator and decision maker [15] in coplanar geometry. Parameters of this Tx and Rx configuration are stated as follows: θ_1 and φ_1 are the Tx apex and full beam divergence, and θ_2 and φ_2 are the Rx apex and field-of-view, respectively. r is the baseline separation between Tx and Rx.

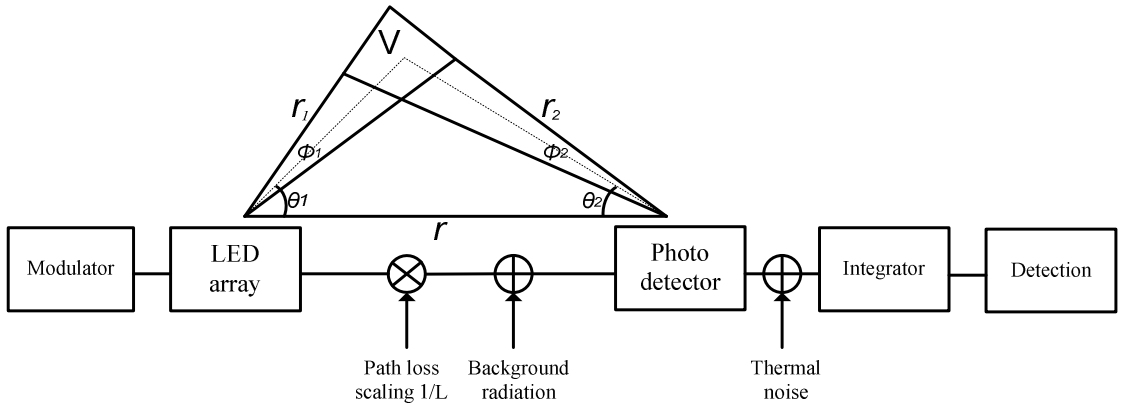


Figure 2.1: UV NLOS communication system model in coplanar geometry.

2.1 An Analytical Single Scattering Model with Receiver Vertical Pointing

2.1.1 Introduction

Various path loss models have been developed for solar blind NLOS UV communication links under an assumption of coplanar source beam axis and receiver pointing direction. In this section, I further extend an existing analytical single scattering coplanar analytical model [22] to non-coplanar geometry by applying trigonometry. The model assumes a short-range scenario with negligible turbulence. It characterizes varying geometry by source beam divergence angle and apex angle, receiver field-of-view (FOV) and apex angle, source-receiver baseline distance, and more importantly the off-axis angle that describes offset of the transmitter pointing direction away from the plane of FOV axis and baseline. The model also reflects atmospheric conditions via scattering and extinction coefficients. I consider the case of vertical receiver pointing and arbitrary transmitter orientation. This scenario meets the needs of many practical communication applications and leads to more tractable analysis. I defer arbitrary receiver orientation to the next section.

2.1.2 Development

A transmission beam may fully, partially, or not intersect with the FOV. We consider an infinitesimal solid angle element within the beam, called a ray for simplicity. Similar to the coplanar approach [22], I first calculate the contribution of a single ray to the received energy among only those rays intersecting with the FOV, and then evaluate the total beam contribution by integration. In order to clearly bound the integration through lower and upper limits, different ray pointing scenarios are discussed in accordance with varying geometry. With double intersections such as at a small ray pointing angle, a ray intersects the FOV boundary twice by

entrance and departure. As the angle increases, transition to single intersection occurs, and the ray remains in the FOV after entering. With no intersection the ray does not enter the FOV. I provide explicit expressions of corresponding limits that lead to easy integration, and an example shows predicted path loss for a varying non-coplanar geometry as a function of off-axis angle.

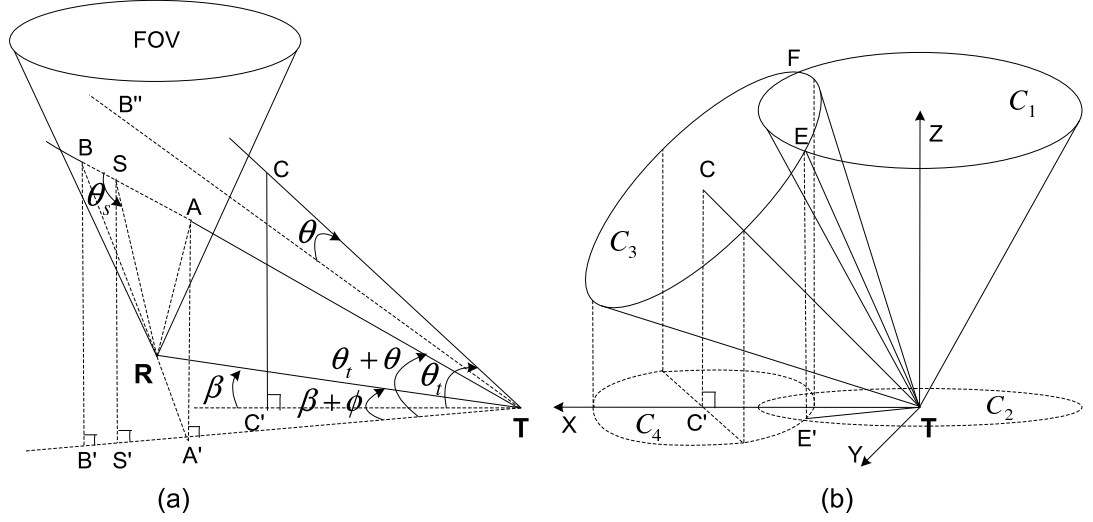


Figure 2.2: System geometry and ray pointing.

Figure 2.2(a) depicts transmit/receive geometry. A transmitter with beam angle φ_t at point T has apex angle θ_t , $\angle CTC'$ between beam axis TC and its projection onto the ground TC' . A receiver with FOV φ_r at point R has apex angle $\theta_r = 90^\circ$ (vertical pointing). A ray within the beam intersects the FOV boundary at entrance point A and departure point B . Photons within the FOV are scattered once and those with proper orientation are captured by the receiver. For a typical scattering point S on AB , scattering angle $\theta_s = \angle BSR$ is between the photon forward direction SB and scattered direction SR (segment length L). Projections of A , S , and B onto the ground are A' , S' and B' , respectively. The lengths of TA (l_{min}) and TB (l_{max}) specify the lower and upper limits of TS (l) that photons have to travel before being scattered.

Let \mathcal{F} represent the plane of the FOV axis and baseline TR . Hence I can define off-

axis angle β as the angle between \mathcal{F} and TC' , which is also the angle between TR and TC' , so $\beta \in [-\pi, \pi]$. Moving TC' from TR (counterclockwise) yields a positive β , and negative otherwise. Under these definitions, (θ_t, β) uniquely specifies the beam axis direction. To specify the direction of the ray, I use two angles. One is the angle ϕ between ray projection TA' and beam axis projection TC' (counterclockwise from TC' is the positive direction). The other angle is obtained as follows and illustrated by Figure 2.2(b). Assume the ray is on the surface of a cone centered at the ground with the normal direction originated at T . The cone (called the equal- θ cone) intersects with the plane $C'TC$ at TB'' . Then the angle θ between TB'' and the beam axis uniquely specifies the cone where the ray lies. θ is positive if taken clockwise from the beam axis, and negative otherwise. Thus the pointing angle of the ray is $\theta'_t = \theta_t + \theta$. Therefore, θ'_t and $\beta + \phi$ uniquely describe the direction of each ray, with θ and ϕ as two important variables. The maximal possible range for $\beta + \phi$ is assumed within $[-\pi, \pi]$. Although I only illustrate the double intersection case in Figure 2.2, other intersection cases can be similarly explained with corresponding notation defined.

Following the propagation theory in [22] and referring to [23], the energy contributed by a single ray to the unit area detector is

$$E_o = \int_{l_{min}}^{l_{max}} E_t \frac{e^{-\sigma_e(l+L)} \sigma_s P(\theta_s) \cos(\zeta) dV}{\Omega l^2 L^2} I, \quad (2.1)$$

where $\Omega = 2\pi(1 - \cos \varphi_r/2)$, $dV = l^2 \cos(\theta'_t) dl d\phi d\theta$, E_t is the beam energy, σ_s is the atmospheric scattering coefficient, σ_e is the extinction coefficient, and $P(\theta_s)$ is the scattering phase function as a combination of Rayleigh and Mie scattering phase functions [23]. I is a dimensionless indicator function depending on whether the ray has intersected the FOV based on $|\beta + \phi|$, and will be discussed later. In Eq. (2.1), ζ is the angle between the FOV axis and SR , which equals $\angle RSS'$. It can be found easily as shown below. Note that the side $S'R$ belongs to two triangles $\triangle TRS'$ and $\triangle SRS'$ in Figure 2.2(a), and $SS' = l \sin(\theta'_t)$, $TS' = l \cos(\theta'_t)$.

Applying the cosine rule gives

$$\begin{aligned}(S'R)^2 &= r^2 + l^2 \cos^2(\theta'_t) - 2rl \cos(\theta'_t) \cos(\beta + \phi) \\ &= L^2 + l^2 \sin^2(\theta'_t) - 2Ll \sin(\theta'_t) \cos \zeta.\end{aligned}\quad (2.2)$$

Therefore

$$\cos(\zeta) = \frac{L^2 - l^2 \cos(2\theta'_t) - r^2 + 2rl \cos(\theta'_t) \cos(\beta + \phi)}{2Ll \sin(\theta'_t)}.\quad (2.3)$$

After some algebraic manipulations, Eq. (2.1) becomes

$$E_o = \frac{E_t I \cos(\theta'_t) \sigma_s d\phi d\theta}{2\pi(1 - \cos \frac{\varphi_t}{2})} \int_{l_{min}}^{l_{max}} \frac{P(\theta_s) \cos(\zeta) dl}{L^2 \exp[\sigma_e(l+L)]}.\quad (2.4)$$

To account for the total contribution of the entire beam, further integration over both θ and ϕ are necessary. Assume $\theta \in [\theta_{min}, \theta_{max}]$ and $\phi \in [\phi_{min}, \phi_{max}]$. Thus the received energy contributed by the entire beam is

$$E_r = \frac{E_t \sigma_s \int_{\theta_{min}}^{\theta_{max}} \cos(\theta'_t) \int_{\phi_{min}}^{\phi_{max}} I \int_{l_{min}}^{l_{max}} \frac{P(\theta_s) \cos(\zeta)}{L^2 \exp[\sigma_e(l+L)]} dl d\phi d\theta}{2\pi(1 - \cos \frac{\varphi_t}{2})},\quad (2.5)$$

where L and θ_s are functions of l , ϕ and θ shown later. If the detector area is A_r , path loss can be obtained as $PL = \frac{E_t}{A_r E_r}$.

Next, I will find the integration limits for l , ϕ and θ , indicator function I , as well as L and θ_s , to fulfill the integration in (2.5). I find l_{min} and l_{max} first, where different ray pointing angles lead to different cases.

Case 1: Double intersection

When $\theta'_t < \pi/2 - \varphi_r/2$, the ray will both enter and exit the FOV with intersecting points A and B. So $l_{min} = TA$ and $l_{max} = TB$, and thus both of them are finite. Denote the length of TA' as x . Since the side RA' belongs to the two triangles $\triangle RAA'$ ($\angle RAA'$ is $\psi_r/2$) and $\triangle RTA'$, applying the cosine rule to $\triangle RTA'$ and laws of trigonometry to triangles $\triangle TAA'$ and

$\triangle RAA'$, both sides of the following equation represent $(RA')^2$ as

$$x^2 \tan^2(\theta'_t) \tan^2 \frac{\psi_r}{2} = x^2 + r^2 - 2xr \cos(\beta + \phi), \quad (2.6)$$

from which x can be obtained. In fact, the above equation also holds for the length of TB' . Its two roots are

$$x_{1,2} = r \frac{\cos(\beta + \phi) \pm \sqrt{\cos^2(\beta + \phi) - \Lambda}}{\Lambda}, \quad (2.7)$$

where $\Lambda = 1 - \tan^2(\theta'_t) \tan^2 \frac{\varphi_r}{2}$, $x_1 = TB'$ corresponds to the “+” term in (2.7), $x_2 = TA'$ corresponds to “−”, and $x_1 > x_2$. Then, l_{max} and l_{min} are given by

$$l_{max} = x_1 / \cos(\theta'_t), \quad l_{min} = x_2 / \cos(\theta'_t). \quad (2.8)$$

There will be an upper bound α_{max} for $|\beta + \phi|$ to ensure the intersection. When this bound is achieved, points A and B coincide and $l_{min} = l_{max}$ holds, which requires $x_1 = x_2$ or equivalently $\Lambda = \cos^2(\beta + \phi)$. Substituting this expression for Λ , I find

$$\alpha_{max} = \arcsin[\tan(\theta'_t) \tan \frac{\varphi_r}{2}]. \quad (2.9)$$

Case 2: Transition to single intersection

When $\theta'_t = \pi/2 - \varphi_r/2$, the ray enters the FOV and remains therein without departure. There exists only one intersecting point A, while B approaches infinity, so $l_{max} = \infty$. Now $\Lambda = 0$, and (2.6) becomes $2xr \cos(\beta + \phi) = r^2$. Thus $x_2 = \frac{r}{2 \cos(\beta + \phi)}$. Then l_{min} is found from x_2 according to Eq. (2.8), and α_{max} equals $\frac{\pi}{2}$ according to (2.9).

Case 3: Single intersection

When $\pi/2 - \varphi_r/2 < \theta'_t < \pi/2$, l_{min} is finite and $l_{max} = \infty$. No matter what the value of $\beta + \phi$ is, the ray always intersects with the FOV, so α_{max} reaches π . In this case, x_2 is obtained from Eq. (2.7) and l_{min} follows (2.8).

Case 4: Extreme single intersection

If $\theta'_t = \pi/2$, $\tan(\theta'_t)$ does not exist, nor does Λ . So x_2 cannot be calculated according to Eq. (2.7). In this case, I still have $l_{max} = \infty$, but need to find l_{min} differently. Now the ray becomes vertical, and the projection of point A becomes T . From triangle $\triangle ATR$ in Figure 2.2(a), l_{min} can be easily found to be

$$l_{min} = r / \tan(\varphi_r/2). \quad (2.10)$$

In addition to the limits l_{min} and l_{max} , other quantities are also required in (2.5). The indicator function I takes the form

$$I = \begin{cases} 1, & |\beta + \phi| \leq \alpha_{max} \\ 0, & \text{otherwise} \end{cases}. \quad (2.11)$$

Applying the cosine rule to triangles $\triangle TSR$ and $\triangle ASR$, I obtain two equations for L and θ_s

$$l^2 + L^2 + 2Ll \cos \theta_s = r^2, \quad (2.12)$$

$$(l - l_{min})^2 + L^2 + 2(l - l_{min})L \cos \theta_s = \left[\frac{l_{min} \sin(\theta'_t)}{\cos \frac{\varphi_r}{2}} \right]^2, \quad (2.13)$$

where I have replaced the length of AR by $l_{min} \sin(\theta'_t) / \cos(\varphi_r/2)$ based on triangles $\triangle TAA'$ and $\triangle RAA'$, and applied the identity $\cos(\pi - \theta_s) = -\cos \theta_s$. Solving these for L and θ_s gives

$$L = \sqrt{l\{l - l_{min} + l_{min} \left[\frac{\sin(\theta'_t)}{\cos \frac{\varphi_r}{2}} \right]^2\}} - \frac{l - l_{min}}{l_{min}} r^2, \quad (2.14)$$

$$\theta_s = \arccos\left(\frac{r^2 - l^2 - L^2}{2Ll}\right). \quad (2.15)$$

Next I will determine ϕ_{min} and ϕ_{max} . The range for ϕ is symmetric about zero, (i.e., $\phi_{min} = -\phi_{max}$) since the beam is symmetric about its axis. Referring to Figure 2.2(b), consider the bottom sides of the equal- θ cone (C_1) and beam cone (C_3), both of which intersect with points E and F (TE and TF represent the rays with ϕ_{max} and ϕ_{min} , respectively). Their projections onto the ground are a circle C_2 and ellipse C_4 described respectively by

$$x^2 + y^2 = \left[D \sin\left(\frac{\pi}{2} - \theta'_t\right) \right]^2, \quad (2.16)$$

$$\frac{(x - D \cos \frac{\varphi_t}{2} \cos \theta_t)^2}{[D \sin \frac{\varphi_t}{2} \cos(\frac{\pi}{2} - \theta_t)]^2} + \frac{y^2}{(D \sin \frac{\varphi_t}{2})^2} = 1, \quad (2.17)$$

where D is the length of TE , a dummy variable to be cancelled later on. Solving x first, and choosing a proper solution that ensures positive y^2 , I begin with

$$x_{E'} = D \frac{\cos \frac{\varphi_t}{2} - \sin \theta_t \sin(\theta'_t)}{\cos \theta_t}, \quad (2.18)$$

that serves as the x-coordinate of E' (projection of E onto the ground). Substituting $x_{E'}$ into Eq. (2.16), I find the positive solution $y_{E'}$ for y , and then $\phi_{max} = \arctan(y_{E'}/x_{E'})$, independent of D . The result is valid under an assumption that C_2 and C_4 intersect. When $\pi/2 - \theta'_t \leq \theta_t + \varphi_t/2 - \pi/2$, there is no intersection between them, and $\phi_{max} = \pi$.

The range for θ can be found as follows. Firstly, $\theta \in [-\frac{\varphi_t}{2}, \frac{\varphi_t}{2}]$ since the ray must be within the beam. Also θ should satisfy $\theta_t + \theta \leq \frac{\pi}{2}$ according to the pointing geometry. Combining these two conditions, I have

$$\theta_{min} = -\frac{\varphi_t}{2}, \quad \theta_{max} = \min(\frac{\varphi_t}{2}, \frac{\pi}{2} - \theta_t). \quad (2.19)$$

This completes the derivations of variables required for evaluation of path loss equation (2.5).

2.1.3 Numerical Results

Numerical evaluations show that our non-coplanar model agrees with [22] when in coplanar geometry. As an example, I consider the link path loss per unit area cm^2 versus off-axis angle β under different non-coplanar geometric settings $(\theta_t, \theta_r, \varphi_t, \varphi_r)$ with $r = 50\text{m}$. Results are shown in Figure 2.3. The scattering and extinction coefficients are chosen as in [23]. Path loss increases slowly and approximately linearly when β is relatively small, as all rays within the beam contribute to the received energy through single scattering within the FOV. When β increases such that there is only partial beam intersection with the FOV, the path loss grows almost exponentially. The critical point, from linear to exponential variation, depends on the

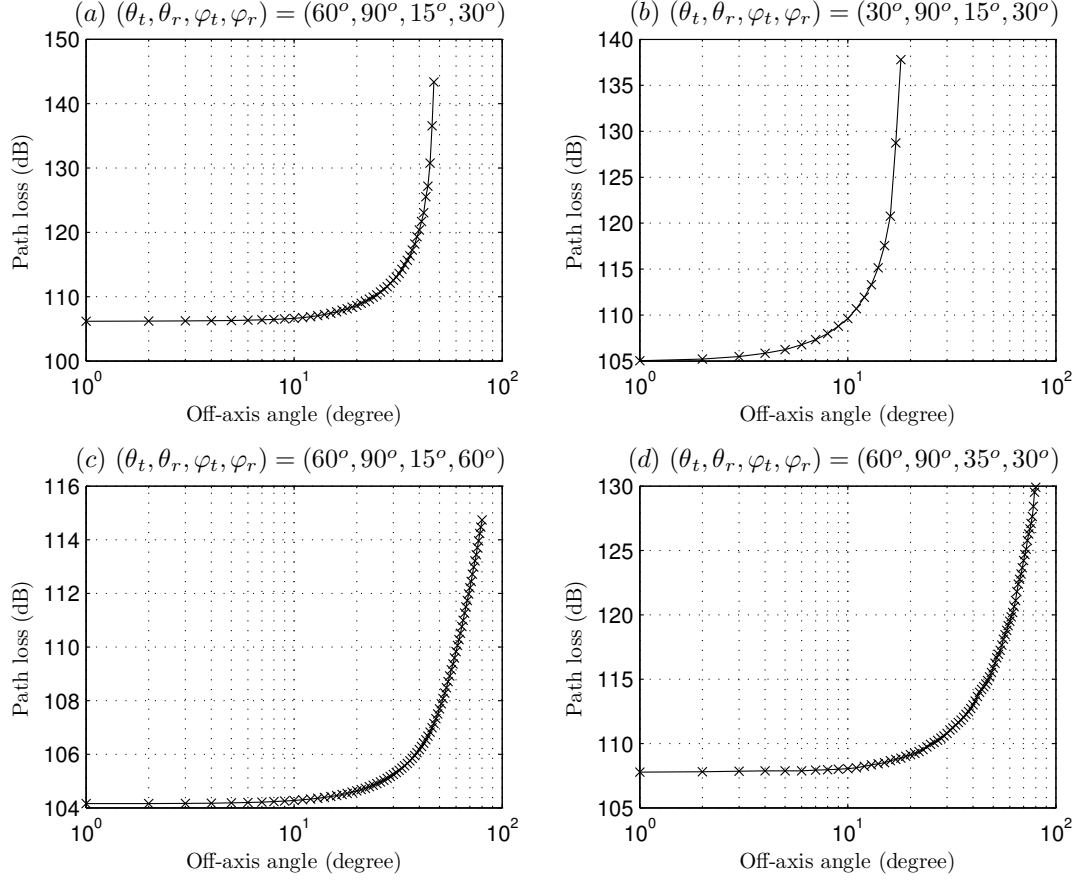


Figure 2.3: Path loss per cm^2 versus off-axis angle.

geometry. For example, θ_t decreases from 60° to 30° from Figure 2.3(a) to Figure 2.3(b), and the critical value for β decreases from 20° to 7° . Similar evaluation reveals the effects of the beam widths, range, and so on.

2.2 An Approximate Closed-form Single Scattering Model with Arbitrary Pointing

2.2.1 Introduction

NLOS UV communication link path loss models have been explored for both coplanar and non-coplanar geometries, and these typically require numerical evaluation. In this section, I

apply single-scattering propagation theory and trigonometry to develop a simple closed-form model suitable for non-coplanar geometry with arbitrary pointing. For simplicity, I treat the overlap volume as a frustum of a cone as in [23] instead of an irregular polyhedron, and approximate its contribution proportional to volume, rather than using triple integrals to evaluate the contribution as in [1]. The model fits varying non-coplanar geometries and incorporates atmospheric effects via scattering and extinction coefficients. In common with the UV communication link models cited, I assume short-range and ignore turbulence.

2.2.2 Development

A typical coplanar link geometry is explained by Figure 2.1. I largely follow [23], although non-coplanar direction offset requires new notations. Let r denote the baseline separation between the Tx and Rx, V the beam and FOV overlap volume, and r'_1 and r'_2 the distances of the volume center to Tx and Rx, respectively. Let φ'_1 be the Tx beam divergence angle and φ'_2 the Rx FOV angle, and let θ'_1 and θ'_2 describe the apex angles of Tx and Rx, respectively.

In order to make the non-coplanar model development easy to follow, I first consider a simple case in which the Rx FOV always faces towards the Tx, i.e., the projection of the FOV axis onto the horizontal plane overlaps the baseline connecting the Tx and Rx. Within this restriction the Tx beam axis direction is arbitrary and generally non-coplanar. Also I assume the Tx beam angle is smaller than the FOV angle while noting that, similar to [1], our model can easily accommodate the alternative case of a larger beam angle with smaller FOV. The model accuracy is reduced when the overlap volume becomes large, corresponding to large FOV at both Tx and Rx, similar to [23].

Figure 2.4(a) is a 3-dimensional non-coplanar pictorial view with the Tx beam axis offset from coplanar direction TA_c to an arbitrary non-coplanar direction TA_n , with offset angle α .

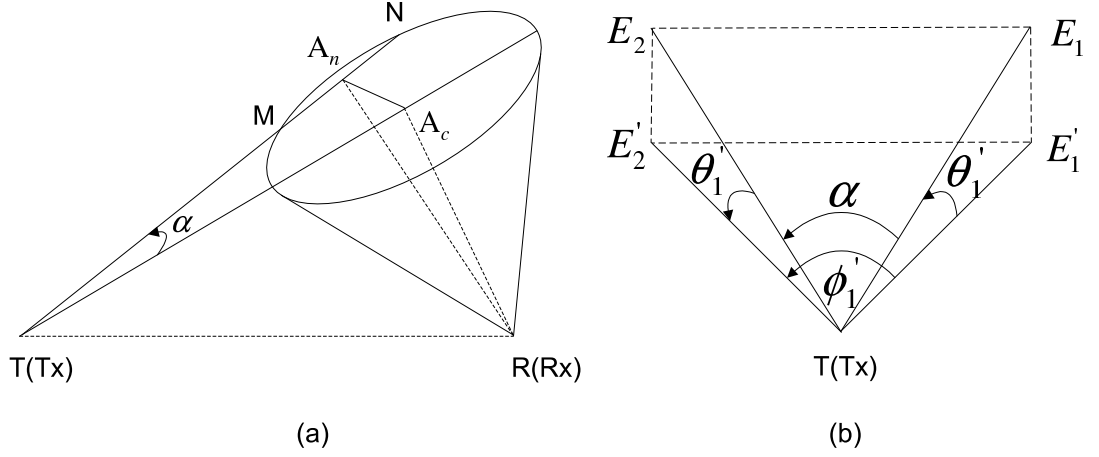


Figure 2.4: (a) The transmit beam and receiver FOV intersection changes as the Tx beam deviates from a coplanar geometry; (b) The relationship between ϕ'_1 and α .

Here, the cone represents the Rx FOV. From the Tx viewpoint the FOV/beam intersection is approximately a circle with beam span within the FOV as its diameter, while the FOV/beam intersection from the viewpoint of the Rx is approximately a frustum with the beam axis segment within the FOV (i.e., MN) as its height. I adopt an approach similar to [23] to approximate the overlap volume and distances of its center to Tx and Rx, respectively. Rather than using α , it is more desirable to use the off-axis angle ϕ'_1 on the horizontal plane to describe the non-coplanarity, defined as the angle between Tx-Rx baseline and the projection of the beam axis onto the horizontal plane. Their relationship is shown in Figure 2.4(b), where TE_1 and TE_2 represent axes of beams in coplanar and non-coplanar directions, respectively. Both of them have the same apex angle θ'_1 . Applying the cosine rule to triangles $\triangle E_1TE_2$ and $\triangle E'_1TE'_2$ and noticing $E_1E_2 = E'_1E'_2$, I obtain

$$\alpha = \arccos(\sin^2 \theta'_1 + \cos^2 \theta'_1 \cos \phi'_1). \quad (2.20)$$

In Figure 2.4(a), TA_c and TA_n represent the directions of beam axis in coplanar and non-coplanar geometry, respectively. Thus $TA_c = r_1$ and the length of TA_n is denoted as r'_1 , which is the distance from the Tx to the center of the overlap volume in non-coplanar geometry. The

point A_n is the midpoint of MN . Obviously, I have $A_c A_n \perp MN$ such that

$$r'_1 = r_1 \cos \alpha. \quad (2.21)$$

The distance between the Rx and the center of overlap volume in non-coplanar geometry is obtained as

$$r'_2 = \sqrt{(A_c A_n)^2 + (R A_c)^2} = \sqrt{(r_1 \sin \alpha)^2 + r_2^2}, \quad (2.22)$$

since $\angle A_n A_c R$ is a right angle. Note that r'_1 decreases as off-axis angle increases, which is consistent with Eqs. (4) and (5) in [1]. r_1 and r_2 are distances in coplanar geometry in the same form as [23], given by

$$r_1 = r \sin \theta'_2 \csc(\theta'_1 + \theta'_2), \quad r_2 = r \sin \theta'_1 \csc(\theta'_1 + \theta'_2). \quad (2.23)$$

Now the overlap volume is considered to be the difference of two cones sharing the same apex as Tx but with heights h'_1 and h'_2 , respectively, where $h'_1 = r'_1 + a'$, $h'_2 = r'_1 - a'$, and

$$a' = \sqrt{(r_2 \varphi'_2 / 2)^2 - (r_1 \sin \alpha)^2}, \quad (2.24)$$

according to right triangles $\triangle T A_c A_n$ and $\triangle M A_c A_n$. The radius of the larger bottom surface is $D_1 = h'_1 \varphi'_1 / 2$ and the radius of the smaller bottom surface is $D_2 = h'_2 \varphi'_1 / 2$. Thus the common volume is $V' = \frac{1}{3} \pi (D_1^2 h'_1 - D_2^2 h'_2)$, which is $\frac{1}{12} \pi (\varphi'_1)^2 [(h'_1)^3 - (h'_2)^3]$. Consider h'_1 and h'_2 are both close to r'_1 . Applying their expressions and expanding $(h'_1)^3 - (h'_2)^3$, I obtain $V' \approx \frac{1}{2} \pi a' (r'_1 \varphi'_1)^2$.

Define the link loss as the ratio of transmitted energy over received energy. According to Eq. (1) of [23], the link loss per unit area becomes

$$L_n \approx \frac{4[1 - \cos(\varphi'_1 / 2)](r'_1 r'_2)^2}{k_s P(\mu) a' (r'_1 \varphi'_1)^2 \cos \zeta \exp\{-k_e(r'_1 + r'_2)\}}. \quad (2.25)$$

ζ is the angle between the FOV axis and a vector from the receiver to the center of the common volume given by

$$\zeta = \arccos(r_2 / r'_2). \quad (2.26)$$

$\mu = \cos \theta_s$, so based on $\triangle A_n TR$, phase angle θ_s equals

$$\theta_s = \arccos\{[r^2 - (r'_1)^2 - (r'_2)^2]/(2r'_1 r'_2)\}. \quad (2.27)$$

Next, I consider a more general case where projections of both the beam axis and FOV axis may deviate from the baseline, described by ϕ_1 and ϕ_2 . Similar to the definition of ϕ'_1 , ϕ_1 and ϕ_2 are defined as angles between the baseline and corresponding axis projections, respectively. The model developed above is the case in which $\phi_2 = 0$. Note that even if ϕ_1 nor ϕ_2 equals zero, I can still apply coordinate transformation (rotation) to transform the full non-coplanar system to the above partial non-coplanar system, as described next.

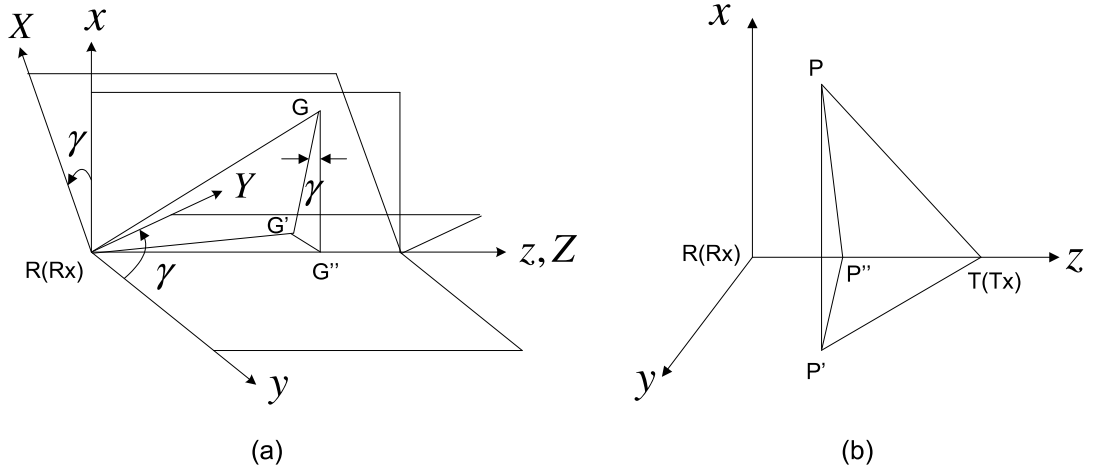


Figure 2.5: Coordinate system rotation.

Figure 2.5(a) explains how these two coordinate systems connect. Here, I adopt a Cartesian coordinate system. The plane yz represents the ground, xz is perpendicular to yz , and coordinate axis z and Z coincide. T_x lies on the coordinate axis z . The FOV axis RG resides in the plane XZ . The angle between xz and XZ is defined as γ . The earlier model and all involved geometric quantities (i.e., $\theta'_1, \theta'_2, \phi'_1, \phi'_2$ and ϕ'_1) are in fact associated with the coordinate system XYZ . In coordinate system xyz , T_x apex angle and R_x apex angle are defined as θ_1 and θ_2 respectively, following the same definitions in coordinate system XYZ . I will transform

the coordinate system $(\theta_1, \theta_2, \phi_1, \phi_2)$ to $(\theta'_1, \theta'_2, \phi'_1, 0)$ in order to apply our results developed earlier.

The projection of RG onto the ground yz is RG' , and onto the plane YZ is RG'' . Thus $\angle GRG' = \theta_2$ and $\angle G'RG'' = \phi_2$, and ϕ_2 is positive when the y coordinate of G' is negative otherwise ϕ_2 is negative. In XYZ , the Rx apex angle θ'_2 is $\angle GRG''$. Considering three right triangles $\triangle RGG'$, $\triangle RG'G''$ and $\triangle GG'G''$, and applying trigonometry, θ'_2 is given by

$$\theta'_2 = \arccos(\cos \theta_2 \cos \phi_2). \quad (2.28)$$

γ equals angle $\angle G'GG''$ since GG' and GG'' are parallel with the coordinate axes x and X respectively. Considering $\triangle GG'G''$, γ is obtained as

$$\gamma = \arctan(\sin \phi_2 / \tan \theta_2). \quad (2.29)$$

Thus, the two coordinate systems axes are related by

$$x = Y \sin \gamma + X \cos \gamma, y = Y \cos \gamma - X \sin \gamma, z = Z. \quad (2.30)$$

In Figure 2.5(b), TP is the beam axis and its projection onto the plane yz is TP' . PP'' is perpendicular to the axis z . Noting that point P is in the common volume, the lengths of baseline TR and TP are r and r_1 , respectively. Following the same system geometry definitions, $\angle PTP'$ is the source apex angle θ_1 , $\angle RTP'$ is the off-axis angle ϕ_1 of the source, and ϕ_1 is positive if the y coordinate of P' is positive otherwise it is negative. Thus the coordinates of the two points T and P can be found as $(0, 0, r)$ and $(r_1 \sin \theta_1, r_1 \cos \theta_1 \sin \phi_1, r - r_1 \cos \theta_1 \cos \phi_1)$, from which beam axis TP is described by

$$\frac{x}{r_1 \sin \theta_1} = \frac{y}{r_1 \cos \theta_1 \sin \phi_1} = \frac{z - r}{-r_1 \cos \theta_1 \cos \phi_1}. \quad (2.31)$$

Simplifying this and substituting Eq. (2.30), I obtain

$$\frac{Y \sin \gamma + X \cos \gamma}{\tan \theta_1} = \frac{Y \cos \gamma - X \sin \gamma}{\sin \phi_1} = \frac{r - Z}{\cos \phi_1}. \quad (2.32)$$

Similarly, in coordinate system XYZ , the line TP can be expressed as follows

$$\frac{X}{\tan \theta'_1} = \frac{Y}{\sin \phi'_1} = \frac{r - Z}{\cos \phi'_1}. \quad (2.33)$$

From the first two equalities of Eqs. (2.31) and (2.32), I can obtain Y/X , equate them and find

$$\theta'_1 = \arctan\left[\frac{\sin \phi'_1 (\tan \theta_1 - \sin \phi_1 \tan \gamma)}{\sin \phi_1 + \tan \theta_1 \tan \gamma}\right]. \quad (2.34)$$

Similarly, from the first and third equalities of Eqs. (2.31) and (2.32), I eliminate the term with Z and obtain one equation for X and Y . Next, applying Y/X obtained previously one can easily find

$$\tan \theta'_1 = \frac{\sin \phi'_1 \cos \gamma - \tan \phi_1 \cos \phi'_1}{\sin \gamma}. \quad (2.35)$$

Substituting Eq. (2.34), I obtain ϕ'_1

$$\phi'_1 = \arctan\left(\frac{\tan \phi_1}{\cos \gamma - \sin \gamma \frac{\tan \theta_1 - \sin \phi_1 \tan \gamma}{\sin \phi_1 + \tan \theta_1 \tan \gamma}}\right). \quad (2.36)$$

This completes the derivations of all required variables to evaluate non-coplanar path loss.

Algorithm Summary: Given $(\theta_1, \theta_2, \phi_1, \phi_2, \varphi_1, \varphi_2, r)$, set $\varphi'_1 = \varphi_1, \varphi'_2 = \varphi_2$. Then successively calculate θ'_2 by Eq. (2.28), γ by Eq. (2.29), ϕ'_1 by Eq. (2.36), θ'_1 by Eq. (2.34); r_1 and r_2 by Eq. (2.23), α by Eq. (2.20); r'_1 by Eq. (2.21), r'_2 by Eq. (2.22), a' by Eq. (2.24); ζ by Eq. (2.26), θ_s using Eq. (2.27). Finally, with these variables I evaluate path loss using Eq. (2.25).

2.2.3 Numerical Results

Figure 2.6 compares path loss versus ϕ_1 for two models: (i) our proposed closed-form approximation for arbitrary non-coplanar geometry, and (ii) the integral-based exact model for Rx vertical pointing developed in [1]. The four subplots correspond to φ_1 equal to $5^\circ, 2^\circ, 0.5^\circ, 0.17^\circ$, while $(\theta_2, \varphi_2, \phi_2, r) = (90^\circ, 30^\circ, 0^\circ, 50m)$. In each subplot, the three curves are parameterized by θ_1 for $30^\circ, 40^\circ$, and 60° . I observe good model agreement when ϕ_1 and θ_1 are both

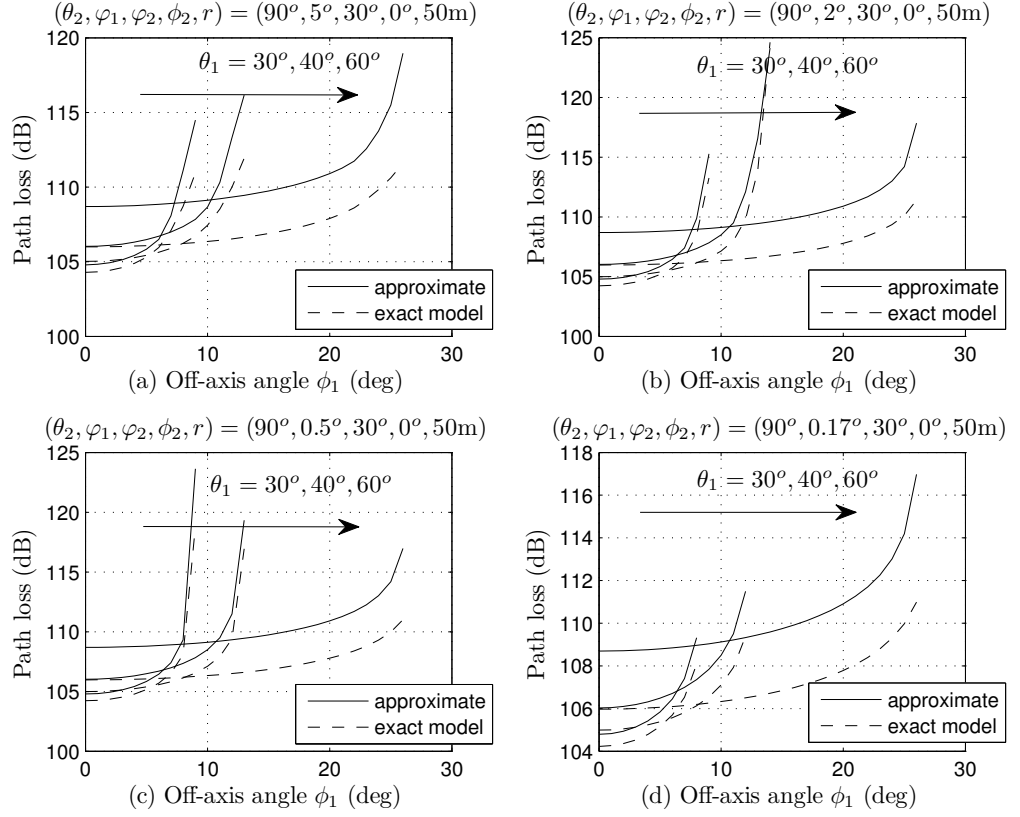


Figure 2.6: Comparison of proposed model and model [1].

small. As ϕ_1 increases, the shape of the beam and FOV intersection becomes more asymmetric and skewed. This results in underestimation of the common volume in our approximation, and the path loss is overestimated. This becomes more evident as the intersection diminishes, with a sharp climb in path loss as ϕ_1 grows. The approximation error also increases as $|\theta_1 + \theta_2 - 90^\circ|$ grows, with underestimation of the intersection height and common volume, resulting in overestimation of the path loss.

2.3 An Empirical Model Incorporating Multiple Scattering

It is necessary to develop a path loss model in a very simple form because the complexity of above two proposed models and other existing ones prevent multi-stage derivations typically

encountered in system and network performance study. In this section, I develop a curve-fitting non-coplanar path loss model based on extensive experiments. Figure 2.7 shows our test-bed for path loss measurements. The FOV, beam angle and Rx pointing angle are illustrated in Figure 2.8. The parameter settings are listed in Table 2.1. I consider Rx pointing angle of 90° to allow a compact transceiver module consisting of multiple switchable LEDs (mounted on side) aiming at different directions and one photodetector on top. This setting also facilitates full duplex discussed in Section 2.4. This design can be easily deployed on the helmets or on top of the moving vehicles.

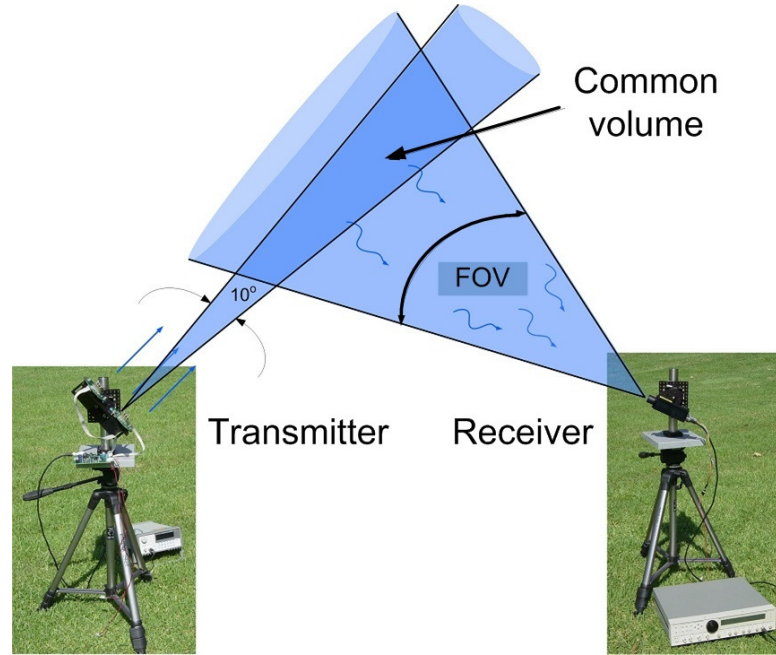


Figure 2.7: Common (overlap) volume between transmission beam and receiving FOV [2].

Different from coplanar settings [23], the new parameter, *off-axis angle*, plays an important role. The off-axis angle ϕ is similar to the traditional pointing angle but emphasizing on the horizontal deviation. It is illustrated in Figure 2.10.

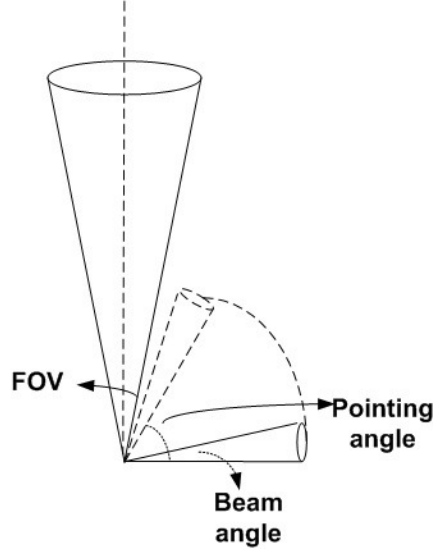


Figure 2.8: Exponential curve fitting (FOV, beam angle and pointing angle).

In [2], short range UV coplanar path loss was proposed to follow the model by Eq. (2.37) and validated by experiments

$$L_{coplanar} = \frac{P_t}{P_r} = \xi r^\alpha, \quad (2.37)$$

where P_t is the transmission power, P_r is the received power at the detector, r is the horizontal distance of the Rx from the Tx, ξ is the path loss factor, and α is the path loss exponent. The last two parameters are functions of pointing angles of Tx and Rx, beam angle, and FOV. It was found α varied from 0.5 to 2.3 [2].

Motivated by (2.37) and new experimental results, the non-coplanar path loss is found to increase almost exponentially with the off-axis angle, as seen from Figure 2.9. Thus the following path loss model can be adopted for the current study

$$L_{noncoplanar} = \xi r^\alpha \exp(b\phi). \quad (2.38)$$

Here ϕ stands for Tx off-axis angle in degree. The Rx off-axis angle is zero since Rx pointing angle is 90° . Without being stated otherwise, all off-axis angles in subsequent discussions in this section refer to Tx off-axis angles. The exponent factor b is not significantly affected by

Table 2.1: Experimental settings

The filter transmission efficiency	0.1
The PMT detection efficiency	0.2
Power of a single LED	0.2 mW
Wavelength	259 nm
Noise	16 photons/s
Filter peak mismatch loss	5%
Beam angle	15°
FOV	30°
Rx pointing angle	90°

the distance r . b is 0.07359, 0.07481, 0.07446 for distance 15m, 30m and 45m respectively as shown in Figure 2.12. However, b decreases with the increasing Tx pointing angle as marked in Figure 2.11. A small b equivalently translates to a slow change of path loss with off-axis angle. Also, b should be a function of Tx/Rx pointing angles, beam divergence angle and FOV if all of them are allowed to vary. If I assume these parameters are the same for all nodes, ξ , α and b are the same for different links as well.

2.4 Full Link Duplexing

Simultaneous transmission and reception for a single transceiver is theoretically feasible as long as there is little self-interference to Rx from backscattering scattering of its co-located Tx. For example, for a vertically pointing Rx with FOV of 30° and a beam angle of 30°, full-duplex is achievable if its own Tx pointing angle is less than 60° to guarantee non-overlapping

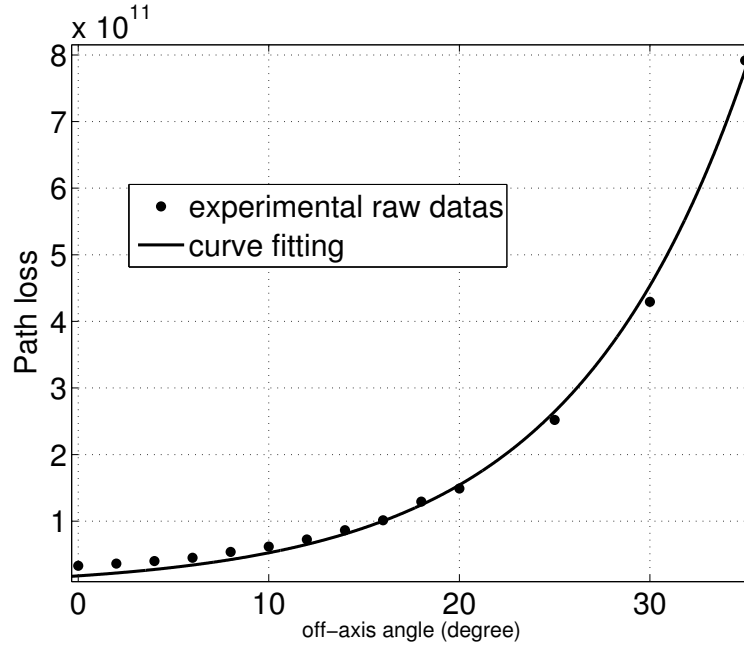


Figure 2.9: Exponential curve fitting (Geometry: pointing angle 15°, distance 15m).

of beam and FOV (see Figure 2.8), and if single scattering from atmospheric particles therein is dominant.

Extensive experiments are performed to test the feasibility of full-duplex. Figure 2.13 demonstrates Rx received power for different remote Tx pointing angles at different distances as well as a reference curve corresponding to its co-located Tx (distance 0m). To ensure high enough received power from one desired remote Tx and low self-interference from its own Tx, small pointing angles (less than 40° at 15m and 34° at 30m) should be selected. Note that, when there are multiple coexisting transmitters, a small pointing angle cannot always guarantee a successful reception since multi-user interference affects the signal quality. When a node transmits at a large pointing angle, received scattering power from its own transmitted signal may overwhelm the desired received signal. In such a case, a half-duplex assumption is mandatory. Thus, this section provides guideline for the transceiver design in order to achieve full-duplex.

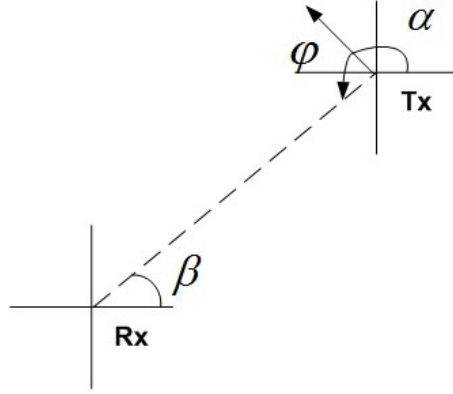


Figure 2.10: An illustration of off-axis angle ϕ . Tx represents a transmitter with four directions; Rx represents an omni-directional receiver.

2.5 Summary

Three link loss models are developed in this chapter. The first developed model is capable of predicting the link loss between a vertical Rx and an arbitrary oriented Tx. The performance is compared with the classic model and achieves a good fit in coplanar geometry. To accommodate truly arbitrary geometry, a simple closed-form expression for single scattering path loss is developed. It is much easier to evaluate than integral-based or Monte Carlo models. The approximation is accurate when θ_1 and ϕ_1 are relatively small. These two models are appropriate for link loss prediction. To facilitate the derivation in system and network analysis, an empirical link loss model is developed based on extensive field experiments. The parameters in the model are derived by curve-fitting method.

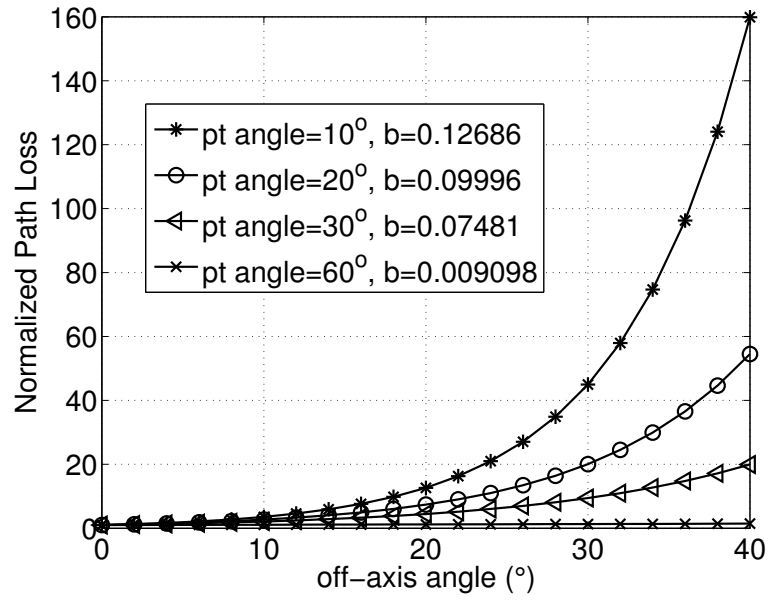


Figure 2.11: The impact of the pointing angle on off-axis angle exponent factor b (distance 30m).

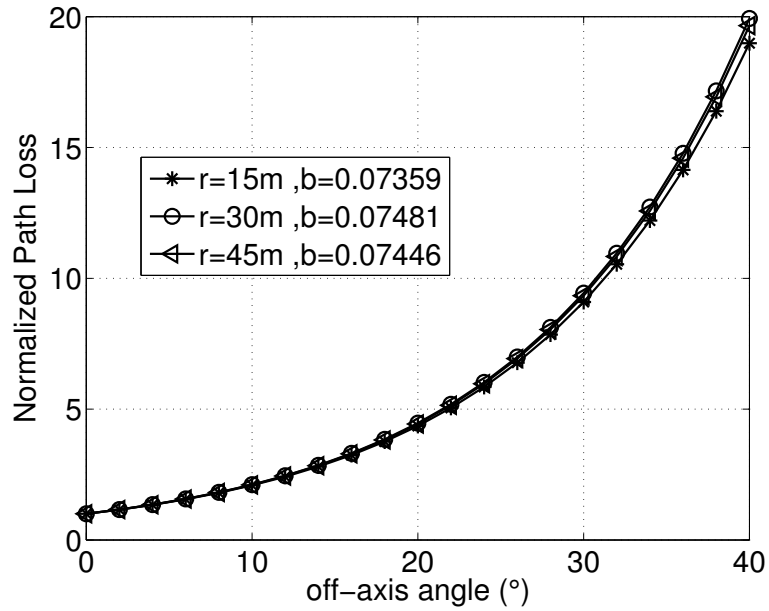


Figure 2.12: The impact of distance on off-axis angle exponent factor b (pointing angle 30°).

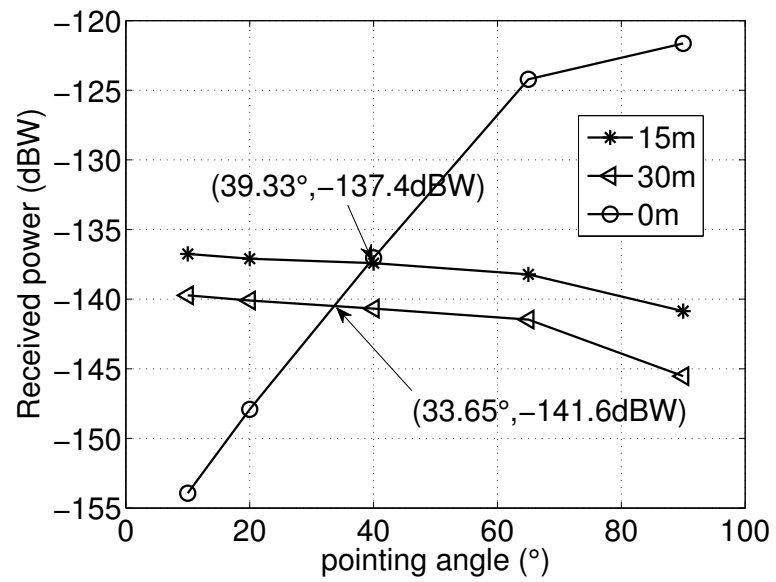


Figure 2.13: Illustration of constraints on the pointing angle at different distance to achieve full-duplex.

Chapter 3

Performance of LED-Based M-PPM

Receivers in NLOS Delay Spread

Channels

Performance of NLOS UV communication receivers has been analyzed under an assumption of no inter-symbol interference (ISI) in the literature. However, ISI may become appreciable when data rate is high in a multiple scattering UV channel. I consider relatively high data rate and develop a performance model with embedded ISI which obviously will degrade the performance but reflect practical conditions. Both analytical derivation and newly reported experimental results on impulse response and path loss are adopted. Results show the relationship among bit error rate (BER), data rate and transmit/receive geometry. These results help us to gain an insight into how an M-ray pulse position modulation (M-PPM) symbol-by-symbol direct detection receiver performs in a UV channel and offer values for advanced receiver design in the future.

3.1 Introduction

UV communication attracts considerable attention from academia [20, 8]. Performance of intensity modulation and direct detection is reported by [15, 29] with and without turbulence effects respectively. Various modulation schemes were considered in the literature. However, none of them considers ISI effect. Since UV signal might encounter multiple scattering during propagation, photons arrive at a detector through different paths. ISI could become severe and lower the maximal potential transmission rate. The pulse broadening effects in NLOS UV multiple scattering channels are experimentally measured by [30]. Thus, in this chapter, I evaluate performance of a symbol-by-symbol detector semi-analytically aided by the measurement data in [2] and [30]. In this analysis, M-PPM scheme is adopted and a typical detector C photomultiplier tube is considered. Results predict the performance of the receiver in the UV channel with ISI effect in different system geometries and data rates.

3.2 System Architecture and NLOS UV Communication System Model

3.2.1 System Architecture

Figure 3.1 shows the system architecture adopted in the analysis of this chapter. The experimental results cited by my work are also obtained from the same system structure. For the completeness of this chapter, the figure is re-introduced as follows.

3.2.2 System Model

References [2] and [30] provided experimental results on NLOS UV channel path loss and impulse response for varying transmit/receive geometry and baseline distance. LED-based

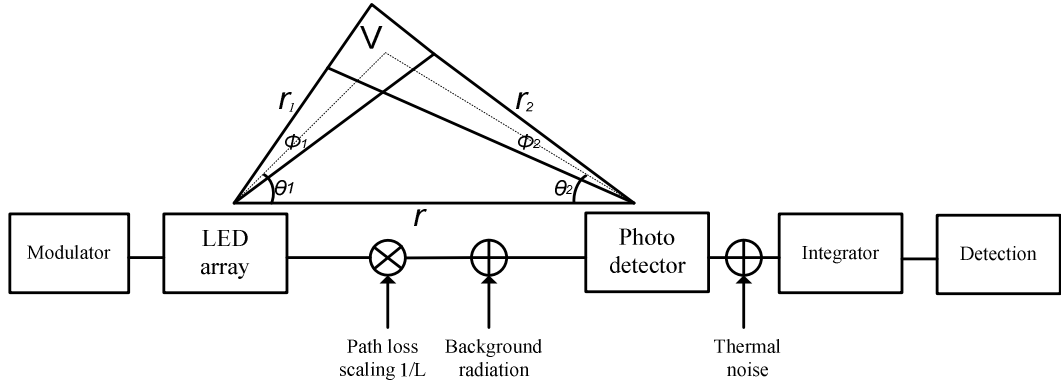


Figure 3.1: UV NLOS communication system model in coplanar geometry.

path loss measurement results will be applied into our performance model for power attenuation calculation. An empirical path loss model is adopted in which model parameters are adjusted according to the measurement. Path loss from 80dB up to 110dB is observed with baseline distance of 100m in different transmit/receive geometries [2].

Laser-based impulse response measurement provides characteristics of pulse broadening induced by channel. Figure 3.2 shows measurement in four typical geometries. Large pointing angles usually lead to longer propagation path such that the pulse broadening is much severer, which is demonstrated in Figure 3.2.

3.3 Performance of PMT Based Receivers without ISI

Reference [15] adopted the results from [2] to analyze the performance of both PMT and avalanche photodiode (APD) based receivers in low data rate scenarios, such that ISI effects do not play an important role. $K_{primary}$ is the photon count (i.e. primary photoelectrons) after integrator but before photon multiplication, which follows a Poisson distribution with photon

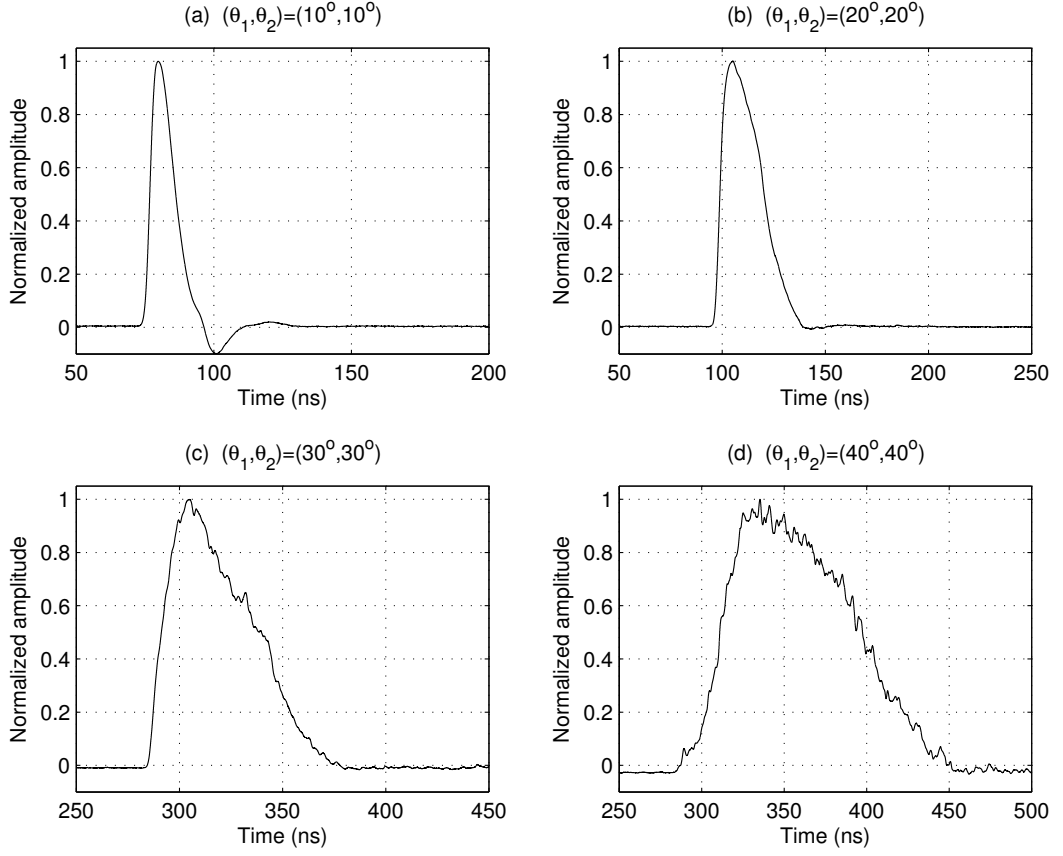


Figure 3.2: Impulse responses of a UV NLOS channel in four different transmit/receive geometries at 100m.

arrival rate λ [31]

$$P_{K_{primary}}(j|\lambda) = \frac{\lambda^j e^{-\lambda}}{j!}. \quad (3.1)$$

The photo multiplication also introduces another stochastic process such that the photon count after multiplication, i.e. the secondary photoelectrons, is random conditioned on $K_{primary}$. Let z be the summation of the output of photoelectrons and thermal noise. The probability density function (PDF) of z is given by [15]

$$p_z(z|\lambda) = \sum_{j=0}^{\infty} P_{K_{primary}}(j|\lambda) G(z, jAe, \sigma^2), \quad (3.2)$$

where A is the detector gain and e is an electron charge. G denotes a standard Gaussian probability density function. σ^2 is contributed by both thermal noise and random gain of the pho-

to detector as follows [15]

$$\sigma^2 = j(\zeta Ae)^2 + (2k_e T/R_L)T_p, \quad (3.3)$$

where ζ is the PMT spreading factor, k_e is the Boltzmann constant, T is the detector operation temperature, R_L is the load resistance and T_p is the duration of transmission pulse.

With the stochastic knowledge of z , the probability of correct detection for M-PPM maximum likelihood (ML) receiver is derived by [15]

$$P_D = \int_{-\infty}^{\infty} p_z(z|\lambda_S + \lambda_b) \left[\int_{-\infty}^z p_z(y|\lambda_b) dy \right]^{M-1} dz, \quad (3.4)$$

where λ_b is the photon count of background noise during one slot time T_p .

3.4 Performance of PMT Based Receivers with ISI

The results in [15] did not rely on channel impulse response model since ISI effect was not involved in analysis. However, based on the experimental result, ISI effects are not negligible when data rate is relatively high (on the order of Mbit/s). Thus, there is no guarantee for [15] to accurately predict performance of a receiver in ISI channel. In this section, I extend the non-ISI derivation in [15] to a new performance model capable of evaluating the ISI effect. Some modifications have to be made to Eq. (3.4) in this new case.

Linear time-invariant (LTI) is the basis of the method of using convolution to obtain received signal from transmission signal and channel impulse response [32]. Channel coherence time T_C is defined as $T_C \approx c/f_c v$ where c , f_c and v are the speed of light, the source frequency, the relative speed of Tx and Rx, respectively [33]. Considering the typical data rate and application scenarios, duration of a symbol T_s normally would be smaller than T_C . Therefore, UV channel can be regarded as a time-invariant channel. Moreover, since UV communication system relies on intensity modulation, the effects from both signal and noise can be summed

together directly, which implies that UV channel can also be considered as a linear channel.

Thus the UV channel is described as a LTI system.

Let T_h represent the length of channel impulse response. Then the duration of received pulse will be extended to $T_p + T_h$ approximately after convolution operation. Since M-PPM is adopted, I have $T_s = MT_p$. As a result, data rate is $R_b = \log_2 M/T_s$. At the receiver, the total number of slots a received pulse can affect is

$$N_{slot} = \text{ceil}[\frac{T_p + T_h}{T_p}], \quad (3.5)$$

where $\text{ceil}(x)$ returns the smallest integer value that is greater than or equal to x . If I define there are maximal N_{symbol} symbols are possible to affect on the present symbol, N_{symbol} can be found as follows

$$N_{symbol} = \text{ceil}[\frac{T_p + T_h}{T_s}]. \quad (3.6)$$

With experimental channel impulse response available and a rectangular transmission pulse shape assumed, received pulse can be numerically obtained via convolution. The received pulse can be partitioned into several parts and each part has a duration of T_p . A vector \mathcal{K} is thus created to define the number of photons in each part

$$\mathcal{K} = [K_1, K_2, \dots, K_{M(N_{symbol}+1)}], \quad (3.7)$$

where $K_i = 0$ when $i > N_{slot}$. Equation (3.4) can be modified as follows

$$P_D = \int_{-\infty}^{\infty} p_z(z|K_s + I_{D_0} + K_b) \prod_{j=1, j \neq D_0}^M \int_{-\infty}^z p_z(y|I_j + K_b) dy dz, \quad (3.8)$$

where K_s and I_j ($j = 1, 2, \dots, M$) is the photon count in the signal slot and the accumulated ISI in the j th slot of the present symbol, respectively. And K_b is the photon count of background noise during T_p . D_0 indicates the position of the signal slot of the present symbol, thus the possible value set of D_0 is $[1, 2, \dots, M]$, which depends on the information bore by the present symbol.

Substitute Equation (3.2) into Equation (3.8) and make some algebra manipulation. I have

$$P_D = \frac{1}{2^{M-1}} \sum_{j=0}^{\infty} \frac{(K_s + I_{D_0} + K_b)^j}{j! e^{K_s + I_{D_0} + K_b}} \int_{-\infty}^{\infty} G(z, jAe, \sigma^2) \prod_{g=1, g \neq D_0}^M [1 + \sum_{k=0}^{\infty} \frac{(I_g + K_b)^k}{k! e^{I_g + K_b}} \text{erf}(\frac{z - kAe}{\sqrt{2}\sigma})] dz, \quad (3.9)$$

where $\text{erf}(x)$ is the Gauss error function defined as

$$\text{erf}(x) = \frac{2}{\sqrt{\pi}} \int_0^x e^{-t^2} dt. \quad (3.10)$$

For K_s and I_j , I have following definitions

$$K_s = K_1, \quad (3.11)$$

and

$$I_j = \begin{cases} \sum_{i=1}^{N_{symbol}} K_{iM-D_i+1+j}, & j \leq D_0 \\ K_{j-D_0+1} + \sum_{i=1}^{N_{symbol}} K_{iM-D_i+1+j}, & \text{otherwise} \end{cases}, \quad (3.12)$$

where index i is the symbol index whose range is $[0, 1, \dots, N_{symbol}]$. D_i represents the position of the signal slot in a previous symbol with $i = 1$ and $i = N_{symbol}$ corresponding to the nearest and farthest symbol respectively. The reason that I_j is a piecewise function is that the slots before the signal pulse within the present symbol are not affected by it. Thus when j is less than D_0 the ISI in the j th slot is only composed of the interference from previous N_{symbol} symbols.

Define $\mathcal{D} = [D_0, D_1, \dots, D_{N_{symbol}}]$ such that \mathcal{D} is random since D_i s are independent and identically-distributed (i.i.d.) variables. P_D is a function of \mathcal{D} , so P_D is also a random variable.

The expected value of P_D is given as

$$E[P_D] = \sum_{i=1}^{M^{N_{symbol}+1}} P_D(\mathcal{D}) \text{prob}(\mathcal{D}), \quad (3.13)$$

where $\text{prob}(\mathcal{D}) = 1/M^{N_{symbol}+1}$ is the probability for each D_i since there are totally $M^{N_{symbol}+1}$ combinations for \mathcal{D} . BER thus is given by [31]

$$E[BER] = \frac{1}{2} \frac{M}{M-1} (1 - E[P_D]). \quad (3.14)$$

Equation (3.14) is numerically evaluated in the next section to show the performance of the UV NLOS M-PPM receiver.

3.5 Numerical Analysis

Different transmit/receive geometry leads to different BER-rate relationship. I investigate four typical scenarios from small pointing angles to relatively large ones. The system parameters are configured as follows: $(\theta_1, \theta_2) = (10^\circ, 10^\circ), (20^\circ, 20^\circ), (30^\circ, 30^\circ), (40^\circ, 40^\circ)$, $P_t = 50\text{mW}$, $N_n = 14500/\text{s}$, $\eta_f = 0.20$, $\eta_{pmt} = 0.30$, $\zeta = 0.10$, $R_L = 5\text{M}\Omega$ and $T = 300\text{K}$. P_t , N_n , η_f and η_{pmt} are Tx average power, background noise count rate, optical filter transmission and PMT quantum efficiency, respectively. Although laser transmitter is operated at 266nm but LED at 259nm, it is reasonable to anticipate similar propagation behavior at these two wavelengths.

Figure 3.3 shows the numerical results for a 4-PPM receiver in four different transmit/receive pointing angles at distance 100m. In the geometry with both θ_1 and θ_2 equal 10° (Figure 3.3(a)), BER of 10^{-3} can be maintained if data rate is lower than 4Mbit/s. Figure 3.3(b) shows that the data rate should be confined within 500kbit/s to achieve a BER smaller than 10^{-3} . If same level of BER is required, possible data rate drops to 40kbit/s in the case of $(\theta_1, \theta_2) = (30^\circ, 30^\circ)$ and 9kbit/s when $(\theta_1, \theta_2) = (40^\circ, 40^\circ)$, respectively. Note that, advanced coding schemes and receivers have not been applied to the system, thus the data rate mentioned above is raw data rate which is possible to be extended to much higher one. This result gives an insight on how to design transmit/receive geometry for a communication link under certain application scenario.

The differences of BER in ISI channel and non-ISI channel are shown in Figure 3.4. The differences between BER increase as the data rate increases because high data rate leads to smaller pulse duration compared to channel delay spread which is fixed such that ISI becomes

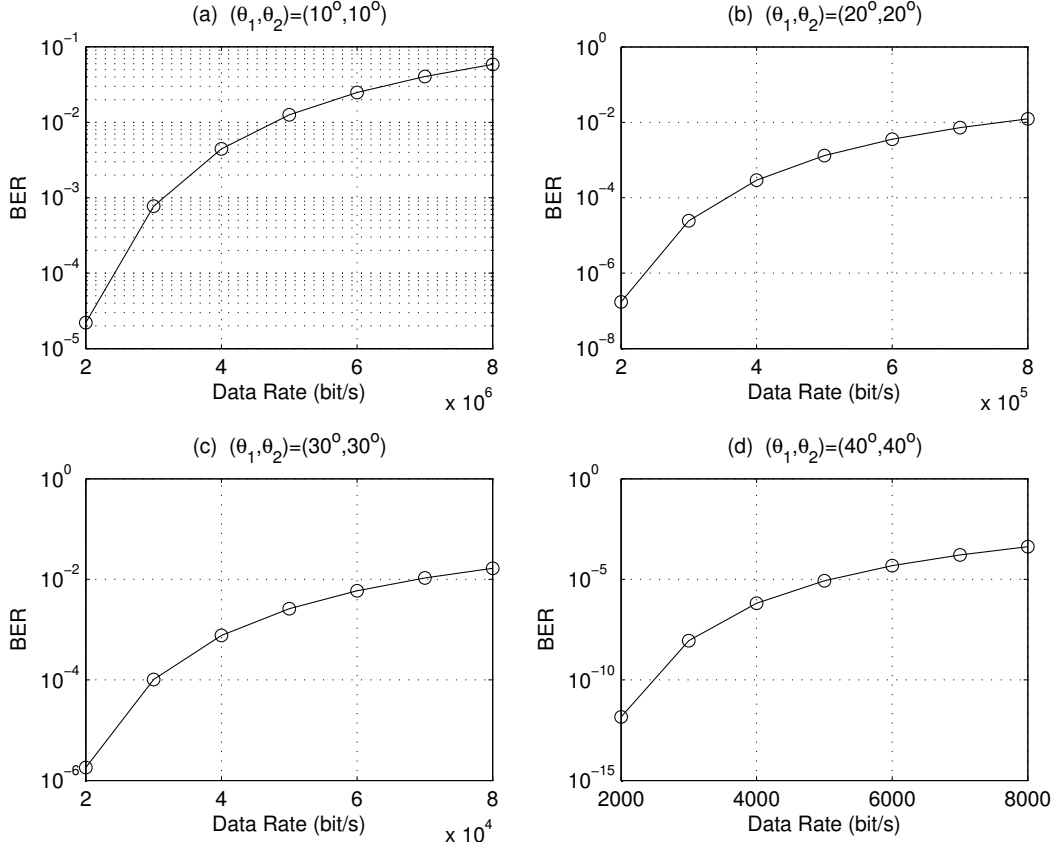


Figure 3.3: BER performance of 4-PPM receiver in ISI NLOS UV channel.

severer.

3.6 Summary

Based on the measurement of channel path loss and impulse response, the performance of NLOS LED-based UV M-PPM receiver is evaluated semi-analytically in delay spread channel. Numerical results illustrate typical operable data rate under different BER requirements in varying transmit/receive geometry. Comparison between the performance of BER with and without ISI effect is conducted. This work can be further extended to a pure analytical study when closed forms of path loss and impulse response are available. Design of advanced receivers which can combat ISI effect is deferred to future study.

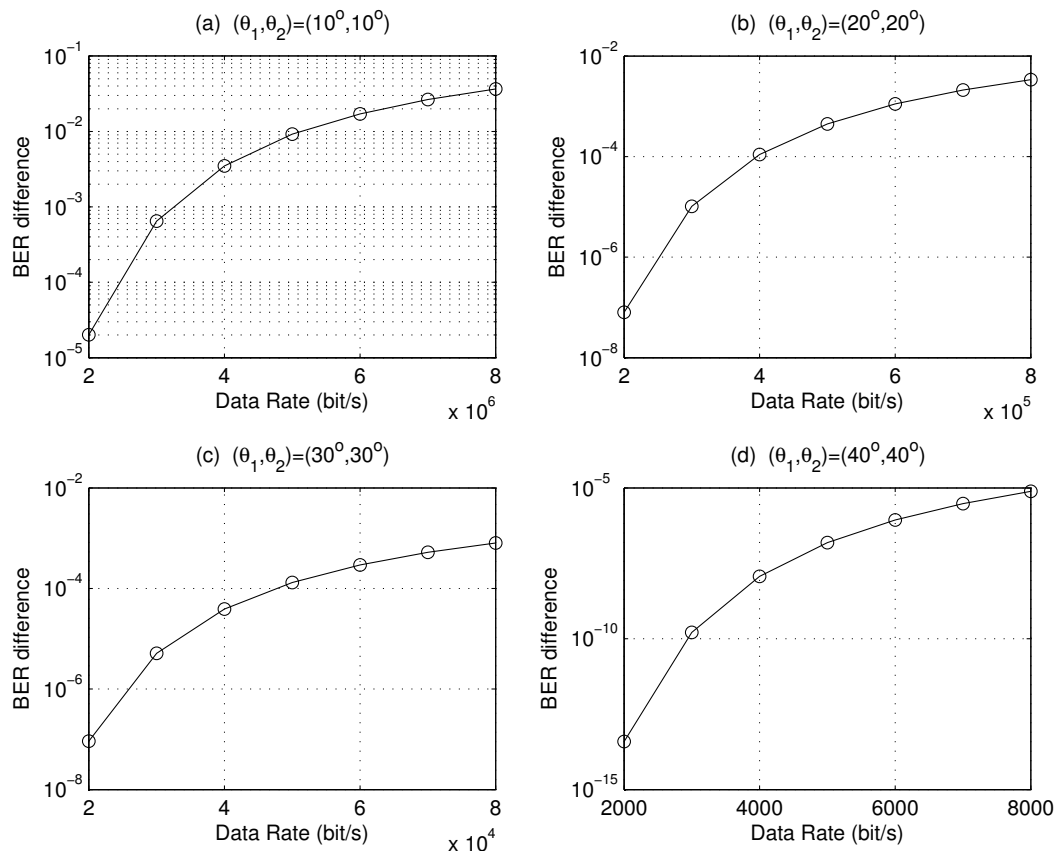


Figure 3.4: BER versus Power in both ISI and non-ISI NLOS UV channel with 4PPM employed.

Chapter 4

Wireless UV Network Models and Performance in Non-coplanar Geometry

Atmospheric scattering for UV signals enables NLOS communication of a transmitter-receiver pair on-the-move and adaptive network configuration. In this chapter, I suggest transmission throughput as a metric to evaluate the performance of a wireless network consisting of randomly distributed nodes operating in such a channel. I further study the effects of some key network parameters including node spatial density, transmission probability and signal detection threshold via the lower bound of the transmission throughput. Performance optimization in the parameter space is performed numerically and simulation results are demonstrated.

4.1 Introduction

Recently, UV spectrum has been re-considered for building a wireless communication network [8], attributed to various more advantageous features than RF. As a fundamental step

towards understanding communication system and network behaviors, channel characteristics have been identified through joint experimental, simulation and theoretical approaches [10, 2, 34, 23]. Despite those efforts, little research has been carried out on NLOS UV communication networks incorporating unique physical layer features.

This chapter focuses on wireless UV networking aspects jointly with NLOS multiple scattering channel modeling under arbitrary Tx and Rx pointing geometry and random node topology. Even though it is a relatively new area, I can draw from related work in centralized or ad hoc RF networking. Paper [35] provided elegant analysis and results in the transport capacity of a wireless network based on a scaling law. The work [36] considered stochastic geometry in designing a performance metric, expected forward progress, to evaluate information transmission and optimum transmission ranges in a direct-sequence spread-spectrum multihop packet radio network, with a closed-form solution in certain channel model (path loss exponent $\alpha = 4$). Weber et al. reported a series of results [37, 38, 39]. The authors proposed and analyzed a metric - transmission capacity which reflects the capacity of single hop network in different cases of fading, power control, and transmission scheduling. The capacity bounds, though analytically intractable when $\alpha \neq 4$, were also derived and studied. However, preliminary study on UV channels reveals that α typically takes a value in the range from 0.5 to 2.3 [2], and this value is not adequately large to meet the requirement imposed by the analysis in the aforementioned work. Therefore it renders RF results therein not directly applicable to UV communication network study. Meanwhile, the NLOS UV path loss behavior appears much more complex [2]. The path loss exponent and path loss factor are both functions of Tx/Rx pointing angles, beam divergence angle, Rx field-of-view (FOV) angle, and Tx/Rx off-axis angles. For short-range UV applications and under typical environmental conditions, channel fading effect is negligible. The randomness is only restricted to node distribution and Tx-Rx geometry.

The unique contributions of this chapter are that I evaluate the network performance and

optimize some key network parameters, i.e., spatial density of nodes, transmission probability and signal to interference ratio (SIR) threshold, to maximize transmission throughput while maintaining a pre-specified outage probability. I show performance by some numerical examples.

4.2 Channel Model

In this chapter, the empirical path loss model developed in [2] is adopted.

4.3 Network Model

A non-coordinated ad hoc network is considered. An aloha MAC protocol is assumed without a central node, so that each node makes independent transmission decisions.

4.3.1 Stochastic Geometry

The performance of a UV network heavily depends on relative locations of nodes and transceiver pointing. To minimize dependence of the model and accommodate most network scenarios of interest, such as unattended ground sensors and small unit communications [8], I do not assume any specific geometry but consider stochastic geometry [40], such that transmission throughput is defined in an average sense. The distribution of node locations follows homogeneous Poisson point process (PPP) with parameter λ as the average number of nodes per unit area. PPP is a uniform distribution in which the expected number of nodes in a region is proportional to the area of this region. If S is the area of a region A , the probability of k nodes in A is given by

$$\Pr[k \text{ in } A] = \frac{\exp(-\lambda S)(\lambda S)^k}{k!}. \quad (4.1)$$

Although applications of a more practical Poisson cluster process (PCP) in military and urban networks with dense hot spots were discussed in [41], PCP introduces higher complexity while performing similarly as PPP in prediction of the transmission capacity in short range. I will adopt homogeneous PPP to describe the positions of the network nodes in this work.

4.3.2 Distribution of Distance and Off-axis Angle

Without loss of generality, a node pair is chosen to build a typical link of interest embedded in the network and study the average outage probability. The rest of the nodes are interference nodes and follow PPP. I assume the receiving node (Rx) is placed at the origin. The distance between the desired Tx and Rx is r_0 , and the distance between the i th interference node and Rx is r_i . The probability density of r_i is

$$f_{r_i}(r) = \begin{cases} \frac{2r}{R^2}, & r \leq R \\ 0, & \text{otherwise} \end{cases}, \quad (4.2)$$

where R is the radius of the network. Similarly, r_0 follows the same distribution but has a different parameter R_0 . The off-axis angle ϕ_i between the i th interference node and Rx follows uniform distribution in $[0, \pi]$

$$f_{\phi_i}(\phi) = \begin{cases} \frac{1}{\pi}, & 0 \leq \phi \leq \pi \\ 0, & \text{otherwise} \end{cases}. \quad (4.3)$$

4.4 Network Performance

A metric of *transmission throughput* is defined to evaluate the performance of the network. It depends on the outage probability.

4.4.1 Outage Probability

Assume each node has a probability p to transmit. Thus equivalently the node density can be viewed as $\lambda_p = p\lambda$. Also assume solar blind condition is applicable and background noise is neglected. Then the network becomes interference limited. For the target link, the SIR conditioned on a realization of relevant random parameters is obtained according to (2.38)

$$SIR = \frac{\frac{P_0}{\xi r_0^\alpha \exp(b\phi_0)}}{\sum_{i=1}^k \frac{P_i}{\xi r_i^\alpha \exp(b\phi_i)} + \frac{pP_s}{L_s}}, \quad (4.4)$$

where P_0 , P_i , and P_s represent the transmission power of desired Tx, the i th interferer, and the transmission power of transmitter co-located with the receiver respectively, k is the total number of interferers, L_s is power loss of the self-interference received by Rx from its co-located transmitter. L_s only depends on the local geometry of the transmitter and receiver within the node and is irrelevant to the network parameters. Therefore L_s is the same for all nodes in the network, but its model is still under investigation. In this work, I rely on measurements. I assume all nodes transmit at the same power level, i.e. $P_0 = P_i = P_s = P$. Considering ξ and α do not change from link to link, r_0 is assumed to be fixed and desired Tx beam axis and Rx FOV are coplanar (successful pointing, i.e. $\phi_0 = 0^\circ$), Eq. (4.4) can be further simplified as

$$SIR = \frac{1/r_0^\alpha}{X + \frac{p\xi}{L_s}}, \quad (4.5)$$

where

$$X = \sum_{i=1}^k X_i, \quad X_i = \frac{1}{r_i^\alpha \exp(b\phi_i)}.$$

From Eq. (4.5), I note SIR is a random variable whose randomness stems from r_0 , r_i , ϕ_i and k . Thus following the traditional definition of outage probability which is the probability that SIR is below a predefined threshold β , this probability is expressed as

$$OP = \Pr(SIR < \beta). \quad (4.6)$$

The value of β is strongly related to the chosen modulation scheme. If I define $x = \frac{1}{r_0^\alpha \beta} - \frac{p\xi}{L_s}$, then Eq. (4.6) becomes

$$OP = \Pr(X > x) = 1 - \Pr(X \leq x). \quad (4.7)$$

In fact, $\Pr(X \leq x)$ is the cumulative distribution function (CDF) of variable X that can be found from its probability density function (PDF). Based on central limit theorem (CLT) [42], X could be approximated as a Gaussian process with mean $k\mu$ and variance $k\sigma^2$, where μ and σ^2 are the mean and variance of X_i . Since X_i is the function of r_i and ϕ_i (assume r_0 and k are fixed), applying their distributions I find

$$\mu = \frac{2[\exp(-b\pi) - 1]}{\pi\alpha b(1 - \frac{2}{\alpha})R^\alpha} + \frac{1 - \exp(-\frac{2b\pi}{\alpha})}{b\pi R^2(1 - \frac{2}{\alpha})}\xi^{1-\frac{2}{\alpha}}. \quad (4.8)$$

$$\sigma^2 = \frac{\exp(-2b\pi) - 1}{2\pi\alpha b(1 - \frac{2}{\alpha})R^{2\alpha}} + \frac{\xi^{2-\frac{2}{\alpha}}}{2b\pi R^2(1 - \frac{1-\exp(-\frac{2b\pi}{\alpha})}{\alpha})}. \quad (4.9)$$

Thus $Z = \frac{X-k\mu}{\sqrt{k\sigma^2}}$ follows a normalized Gaussian distribution, i.e., $Z \sim \mathcal{N}(0, 1)$. The outage probability OP (Eq. (4.7)) can be further derived as

$$OP = \Pr(Z > \psi) = Q(\psi), \quad \psi = \frac{x - k\mu}{\sqrt{k\sigma^2}}, \quad (4.10)$$

where $Q(\cdot)$ is a Q -function. This probability is actually a conditional probability on r_0 and k .

With the known distributions of r_0 and k , its expected value is obtained as

$$\begin{aligned} \overline{OP} &= E_{r_0, k}[OP] \\ &= \int_0^{R_0} \frac{2r_0}{R_0^2} \sum_{k=0}^{\infty} \frac{\exp(-\lambda p R^2 \pi)(\lambda p R^2 \pi)^k}{k!} OP dr_0. \end{aligned} \quad (4.11)$$

4.4.2 Transmission Throughput

In this work, I measure network throughput based on the average performance over a single hop using the above outage probability. From a network point of view, it is desired to have as many simultaneous transmissions as possible while maintaining a low outage probability

per link. For a single link, the probability of successful reception is $1 - OP$. I can define *transmission throughput* (TT) to describe the network performance

$$T = \lambda_p(1 - OP) \ln(1 + SIR). \quad (4.12)$$

The first two items in Eq. (4.12) together represent the number of successful transmission per unit area. The last term $\ln(1 + SIR)$ is proportional to the achievable data rate. It can be observed that T is a function of network parameters λ , p and β . Note that β is the threshold for SIR to ensure successful reception at the desired receiver. Therefore, Eq. (4.12) gives the number of bits exchanged among the nodes in the network per second per unit area. If I replace SIR with β in Eq. (4.13), a lower bound of the transmission throughput is obtained

$$T_l = \lambda_p(1 - OP) \ln(1 + \beta). \quad (4.13)$$

The averaged version is illustrated as follows

$$\overline{T}_l = \lambda_p(1 - \overline{OP}) \ln(1 + \beta). \quad (4.14)$$

4.5 Numerical Results

I study the effects of three key parameters on network performance numerically: the SIR threshold β , spatial density of the nodes λ , and transmission probability p . These parameters are critical: (1) β interacts with the choice of modulation scheme; (2) λ specifies the level of spatial reuse; (3) p stands for the level of temporal reuse. The corresponding results provide us insight into choice of parameter values for the maximum network throughput below certain outage probability.

Table 4.1 shows typical parameter settings if they are not allowed to be variables. The path loss related parameters are obtained through our extensive experiments and [2].

Table 4.1: Parameters settings for numerical evaluation

The range for interferers R	60 m
The range for desired Tx R_0	30 m
Path loss factor ξ	$3/1 \times 10^9$
Path loss exponent α	0.41/1.05
off-axis angle exponent factor b	0.12686/0.009098
Spatial density λ	0.05
Transmission probability p	0.01
SIR threshold β	1dB
Tx pointing angle θ_1	$10^\circ/60^\circ$

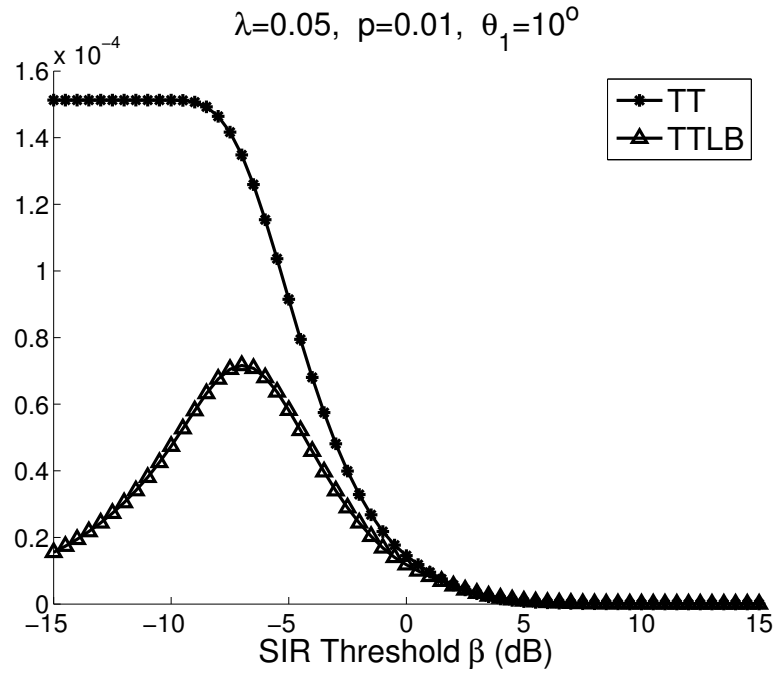


Figure 4.1: Transmission throughput and its lower bound against β for given λ and p .

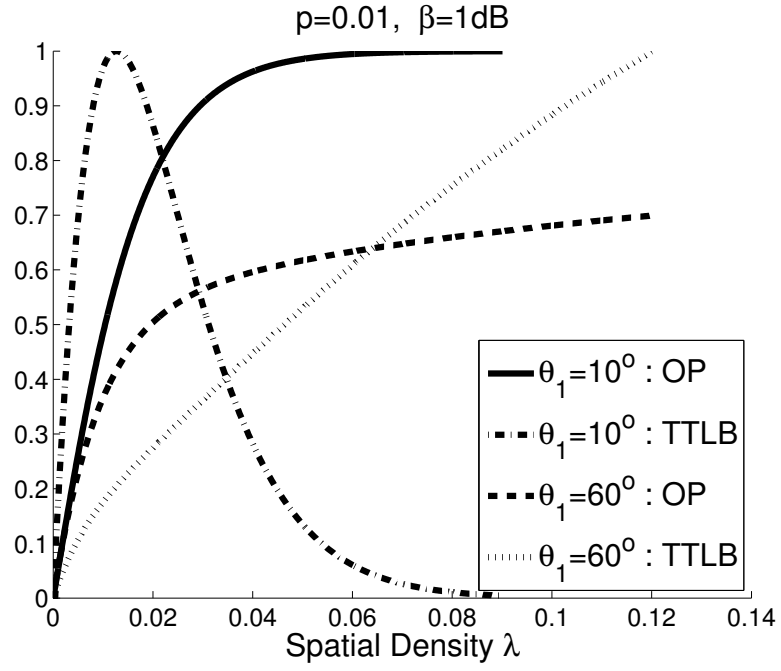


Figure 4.2: Normalized lower bound of transmission throughput and outage probability against λ for given β and p .

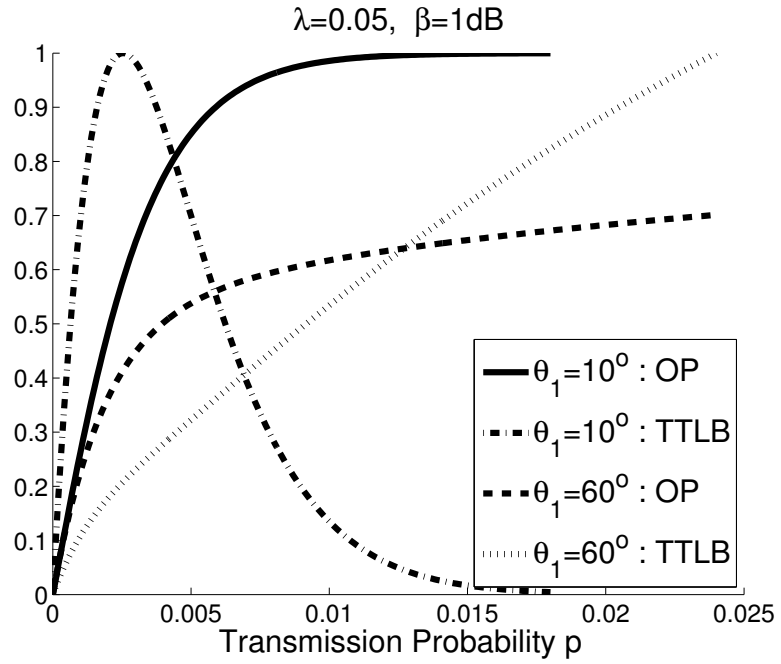


Figure 4.3: Normalized lower bound of transmission throughput and outage probability against p for given λ and β .

Figure 4.1 depicts transmission probability and its lower bound. I notice that the lower bound is tight when β is large, meanwhile the bound is relatively loose with small β because most of the links can achieve higher SIR than β . I adopt the lower bound as a measurement metric to evaluate the effects of λ and p .

I plot the normalized transmission throughput lower bound (TTLB) and outage probability (OP) versus one of the two parameters in one figure. Two sets of curves correspond to Tx pointing angle θ_1 at 10° and 60° respectively. Results are shown in Figs. 4.2 and 4.3. Figure 4.2 shows how TTLB and outage probability change with λ . Although when θ_1 equals 60° , the network could achieve higher transmission throughput in the high spatial density region than that when θ_1 equals 10° , the corresponding outage probability is intolerably high. Therefore, an OP constraint needs to be set and the best λ is numerically obtained from the figure. For example, if I maintain OP to be below a level, I can draw a horizontal line to intersect with the OP curve and find the maximum λ_{max} . Within the feasible range $(0, \lambda_{max})$, the maximum TT can be found with a corresponding optimal λ . In most application scenarios, the network cannot tolerate a high outage probability, especially when the network provides voice or video services. Thus, although high transmission throughput is achievable with relatively large spatial density, one has to sacrifice the transmission throughput to maintain the average OP of each link at a tolerable level. Note that, given the same constraint for outage probability, the case of which $\theta_1 = 10^\circ$ achieves much higher transmission throughput.

For the other figure illustrating the effect of p , one can follow a similar procedure to obtain the best parameter values numerically under a specific outage probability constraint. Unfortunately, analytical solutions are not feasible due to complexity of the function to optimize.

4.6 Summary

In this chapter, I designed a metric called transmission throughput to evaluate the network performance by taking into account the multi-user interference and self-interference due to the full-duplex feature. Although a closed-form solution is not available because of the high complexity of the nonlinear constrained optimization problem, numerical results showed how the transmission throughput changes with the spatial density, transmission probability and SIR threshold. A method was illustrated to obtain the parameter values under the link quality constraint.

Chapter 5

A Leadership-based Neighbor Discovery Protocol for UV Wireless Networks

In this chapter, I propose a neighbor discovery protocol; unlike other protocols, our approach alleviates the negative effects of random access based collisions by choosing a leader that arbitrates the discovery process [43]. Without prior knowledge of the number of nodes in the network, the approach facilitates neighbor discovery in a fast, fair and efficient manner. I perform extensive simulations with a realistic UV PHY layer and demonstrate that the approach reduces the required neighbor discovery time by as much as 90 %. I also examine the impact of various system parameters that can be especially useful to UV network and system designers.

5.1 Introduction

In the applications envisioned, UV communication nodes are likely to be deployed in an ad hoc manner. A node is unlikely to have a priori information about its neighbors or the

network topology. As discussed later, the problem of neighbor discovery is non-trivial since UV communications are likely to use directional transmissions; the node should realize not only the identities of its neighbors but also the best direction in which to transmit in order to effectively communicate with each such neighbor. LOS UV signals are prone to blockage by obstacles; fortunately, nodes can establish possibly multiple NLOS links using which they can communicate.

Our objective in this part, is to design and evaluate an efficient neighbor discovery protocol that (a) allows the fast and efficient discovery of neighbors, (b) can be applied without any prior knowledge of the network topology or configuration, and (c) allows each node to determine the various directions that can be used to communicate with each of its neighbors and *rank* these directions in terms of their effectiveness.

While there have been prior efforts on neighbor discovery for RF wireless networks, they cannot be directly applied in the UV context. First, the unique UV characteristics are different from the propagation effects experienced on an RF channel. Many of the prior approaches (discussed later) rely on GPS or other enhancements which are unlikely to be available in the application scenarios of interest. Secondly, almost all of the previous approaches only discover neighbors using LOS links; neither do they consider NLOS links nor do they provide any assessment on the relative goodness of these links. The design in Reference [3] takes significant time to operate and is inefficient since it uses random access as the basis for neighbor discovery. I propose a much more efficient protocol that can speed up the neighbor discovery process dramatically.

5.2 Related work

There have been a number of efforts on neighbor discovery for RF wireless networks assuming either directional or omni-directional antennas. Vasudevan et al. classify neighbor discovery algorithms into two categories: direct-discovery and gossip-based [44]. They analyze these two possibilities in synchronous and asynchronous scenarios and determine the frequency with which each node should send control packets to maximize the discovery probability within a certain time period. They find that the transmission probability is related to the number of neighbors and transmission beamwidth. The gossip-based algorithms outperform the direct-discovery algorithms. Moreover, the performance of the gossip-based algorithm is not sensitive to the density of the nodes. A handshake-based neighbor discovery algorithm is proposed with a time-division-multiple-access (TDMA) based media-access-control (MAC) protocol in 3D space, in [45]. With an assumption that each node is equipped with GPS or inertial navigation system (INS), the authors suggest that the transmission power can be reduced to first find neighbors nearby and then increased gradually such that the probability of detection is increased. Luo et al. analyzed neighbor discovery in a code-division-multiple-access (CDMA)-like system and assumed each node is aware of its neighbors' names and signatures [46]. It is shown good performance is achieved by applying multiuser detection algorithms; however, the assumptions are unrealistic for an ad hoc network. In [47], methods to save energy in neighbor discovery were researched and a flood-like procedure to achieve neighbor discovery was also suggested. Jakllari et al. proposed an integrated neighbor discovery and MAC protocol for ad hoc networks equipped with directional antennas [48]. The algorithm effectively utilizes directional antennas and accounts for the mobility of the nodes while performing neighbor discovery and maintenance. Vasudevan et al. comprehensively analyzed ALOHA-like neighbor discovery algorithms and proposed a collision detection mechanism to improve the performance in [49]. The algo-

rithm enables each node to know when to terminate the neighbor discovery process without any a priori knowledge of neighbors.

Note that the above algorithms are not directly suitable for a UV ad hoc network. The unique UV scattering channel is fundamentally different from a RF channel. The scenarios are different with both directional and omni-directional antennas. The flexibility in both directional and omni-directional transmissions by a UV source (such as a UV LED) provides degrees of freedom in system design and operation that are not possible with RF. It is possible for a node to know not only the existence of the neighbors but also information about their locations without assistance of GPS or additional devices, contrary to most RF approaches.

The first work (the only work to the best of my knowledge) on neighbor discovery in UV wireless networks is proposed in Reference [3]. A credit-collection protocol is designed to rank the transmission directions of a node for each neighbor, based on packet losses on each directional link. This protocol requires a large number of packet transmissions to achieve stable results and it takes a relatively long time to terminate. Our goal here is to design a much faster protocol for neighbor discovery to obtain the same information about neighbors as in [3].

5.3 UV Communication Link and Transceiver Models

I adopt the empirical path model with multiple scattering assumption developed in Section 2.3. Full-duplexing is supported as demonstrated in Section 2.4.

Figure 5.1 shows the transceiver architecture. The dots on the side facets represent the LED transmitters (a transmitter could consist of multiple simultaneously emitting LEDs) and the dot on the top facet represents the omni-directional photon detecting receiver [50]. With this configuration, the node¹ is a “directionally transmitting” and an “omni-directionally receiving”

¹Without loss of generality, we also refer to a node as a transceiver.

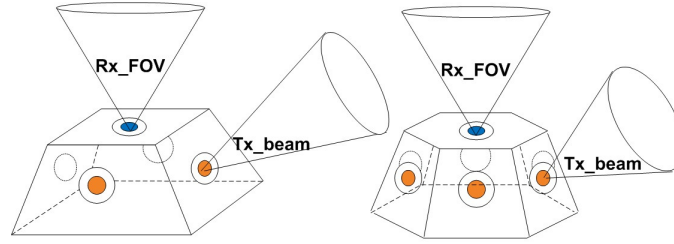


Figure 5.1: A UV transceiver with 4 (left) and 6 (right) transmission directions. Dots on the side facets are the directional LED transmitters; each dot on the top facet is the omni-directional photon receiver.

device. This configuration provides significant benefits in size, cost, and full-duplex communications on links (discussed later). In some cases, it also favors easy installation and deployment (e.g. on the helmet of a soldier or on the top of a vehicle). All following experimental results and the design and evaluation of our neighbor discovery mechanisms are established with this configuration. Note that a practical implementation is not restricted to this shape or the number of facets illustrated in the figure. The number of directions or facets is determined by the transmitting beam angle and is typically chosen so as to maximize spatial coverage and minimize beam overlap simultaneously. For example, if the beam angle of a LED on a side facet of a device is 18° , then this device can have up to 20 side facets. In other words, the number of directions is a system parameter that can be chosen according to source specifications.

5.4 Leadership-based Neighbor Discovery Protocol

In this section, we first elaborate the previously proposed neighbor discovery protocol for a UV network in [3]. We motivate and then, detail the design of our approach.

The first and the only neighbor discovery protocol (to our best knowledge) for a UV network is proposed in [3]. It makes no assumptions about a priori knowledge, such as the number of neighbors or the relative positions of neighbors. The basic procedure is described below:

- The Rx of every node is in a standby state all the time; it can receive anytime thanks to

the full-duplex capability.

- A node randomly chooses a direction to send a packet after waiting for an exponentially distributed period.
- The transmitted packet could be either a request packet or a feedback packet. The request packet contains information about the request sender's ID and the ID of the direction that is being currently used. The feedback packet is composed of feedback sender's ID, request sender's ID, the IDs of the directions, and the total counts of received request packets in corresponding directions.
- When a node receives a request packet from a sender, it schedules a feedback packet to be returned to that sender. If no request packet from other nodes is received within a fixed pre-determined time period, the node will send out a request packet in a randomly chosen direction.
- Each node counts the number of received feedback packets and categorizes them into different groups based on the information carried in such packets. To elucidate, once request sender receives a feedback packet in return, it is aware of the recipient of the request, as well as the corresponding direction in which the request was received. The sender then adds a *credit* to that direction.
- A node ranks the directions for each of its neighbors, based on the number of credits accumulated for each direction. The direction with the highest number of credits is the best direction for that neighbor.

As may be evident from the above description, a node needs to collect a sufficiently large number of credits in order to accurately rank the directions towards a given neighbor. Since the primary mode of communication is random access, collisions occur. This can skew the results

since small sample sets may not yield accurate estimates of the best direction. In other words, this results in short term inaccuracies. Convergence to correct results takes a relatively long period of time.

Given this limitation and the importance of expeditious neighbor discovery, I seek to design an interference-free environment for the process. Our goal here is to enable the discovery of neighbors and the best direction for communications with each neighbor with a *one-time packet exchange*. I later show that our method (proposed below) drastically improves the performance of neighbor discovery in terms of the consumed time, compared to the method proposed in [3].

Proposed approach: In a nutshell, our approach relies on sequential neighbor discovery. A single node (the leader) initially performs neighbor discovery; after that node is done, the leadership is passed on to a second node and so on. I call our approach the “leadership-based neighbor discovery” protocol. In more detail, our approach consists of the following steps:

- Initially, all the nodes are in a standby state. They only receive (listen to) packets but do not transmit anything.
- A pre-chosen leader node (could be randomly chosen) then initiates the neighbor discovery process by sending a request packet in a randomly chosen direction. This request packet includes the ID of the sender and the direction in which it is transmitted.
- The leader waits for a fixed time period T , and then switches to the next direction to send the next request packet. It repeats the process until it performs packet transmissions in all possible directions.
- When a neighbor node receives a request packet from the leader node, it calculates the path loss experienced. Note that this is possible because there is no other concurrent transmission. (This is a key difference from the method in [3]; the path loss cannot be obtained since transmissions are subject to interference.)

- Each such neighbor waits for a period t ; this period is randomly chosen in $[0, T]$. After this period, the neighbor randomly chooses a direction using which it transmits a feedback packet back to the leader. The feedback packet contains the ID of responding node and the path loss estimated using the request packet. The reception of the feedback packets is not guaranteed because contention exists among different neighbors that attempt to send a feedback packet. However as long as the length of feedback packets is much shorter than the maximal waiting time T , it is likely to receive many of these feedback packets with a high probability.
- After the process is complete, the leader node can rank the directions for each discovered neighbor found based on the path loss information contained in feedback packets. It then randomly selects a successor from the nodes in its neighbor list. It sends a notifier packet to the selected successor node, using the best direction recorded for this node. The successor then performs neighbor discovery. All other nodes are made aware, that the neighbor discovery *token* has now been passed on to a different node.

It is possible that the notifier packet gets lost; to account for this, if no request packets are received from the successor for a period $2T$, the former leader node will re-select a new successor. The process may have to be repeated in extreme cases until a successful leadership transfer is achieved. The steps described above are formalized with the pseudo code below:

K = total no. of directions;

Leader:

while rotation not finished yet **do**

if time T is up **then**

 ND_request.source_ID=self_id;

 ND_request.direc_ID=uniformly_choose(K);

```

    send ND_request;

    set  $T$ ;

else

    if receive ND_feedback then

        neighbor_ID=ND_feedback.source_ID;

        prev_direc=ND_feedback.prev_direc;

        PathLoss=ND_feedback.path_loss;

        PathLoss.node[neighbor_ID].direc[prev_direc]=PathLoss;

    end if

end if

end while

# of discovered neighbors is summarized here;

while  $i < \#$  of discovered neighbors do

    order PathLoss.node[ $i$ ].direc[*];

end while

select leader=uniformly_choose(# of discovered neighbors);

send Notifier packet to next leader;

Other nodes:

if receive ND_request then

    dest_ID=ND_request.source_ID;

    prev_direc=ND_request.direc_ID;

    PathLoss=Tx_power/Rx_power;

    set  $t$ =uniformly_choose( $T$ );

    if time  $t$  is up then

        ND_feedback.source_ID=self_id;

```

```

    ND_feedback.prev_direc=prev_direc;

    ND_feedback.path_loss=PathLoss;

    send ND_feedback;

end if

end if

```

Evaluations of our approach: I evaluate the performance of our neighbor discovery protocol via extensive simulations performed using OPNET version 16.0 [51]. The simulation settings are listed in Table 5.1. The chosen transmission power corresponds to the UV transmission range (approximately 50m in Figure 5.2). In all of the following simulations, I assume that the transceiver has 6 directions for transmission operations. The more the directions, the larger the neighbor table maintained and the longer the neighbor discovery process takes. The relation between the number of directions and the time consumed by the neighbor discovery process is discussed later. I adopt the channel model from Section 5.3 to characterize signal propagation. By default, the chosen parameters correspond to the scenario when the transmission pointing angle is equal to 10° . To recall, these parameters are: $\xi = 5 \times 10^9$, $\alpha = 0.4$, $b = 8.7$. The SIR threshold is set to be 1dB; the signal is detectable if the power is larger than the total interference power by this value. The sizes chosen for the three kinds of packets are consistent with that by IEEE 802.11 [52] considering protocols for UV networks are yet to be standardized. Each node is placed randomly in a network area of $1 \times 10^4 \text{m}^2$. The total number of nodes in the network is 10. All the simulation curves are computed as averages of over 10 runs.

I compare the newly proposed protocol (labeled leadership-based) with the previously proposed protocol from [3] (labeled credit-collection) in Figure 5.2. I would like to point out here that this comparison is with the fastest version of the algorithm proposed in [3]. The expected value of the waiting interval λ for credit-collection is set to be 10^{-3}s . The uniformly distributed

Table 5.1: Parameters settings in simulations

Transmission power	4 mW
Number of directions	6
Transmission pointing angle	10°
SIR threshold	1 dB
Collision model	Physical (accumulative) model
Traffic pattern	10000 pkt/sec
Request packet size	32 bits/pkt
Feedback packet size	80 bits/pkt
Notifier packet size	32 bits/pkt
Network size	100 m by 100 m
Number of nodes	10

waiting interval T with the proposed protocol is set to be 2×10^{-3} s; this ensures that the mean is 10^{-3} s and thus, the settings are consistent in both cases. In Fig. 5.2, the leadership-based algorithm leads to the sharp speed up in the neighbor discovery process. It saves about 92% of the time consumed in neighbor discovery, if one were to have a requirement that every node find 70% of its neighbors in the network. It saves about 97% of the time consumed in neighbor discovery if this requirement is stricter and every node has to find about 80% of its neighbors. The credit collection protocol consumes a lot of time to stabilize. These results suggest that interference has a dominant influence on neighbor discovery in UV networks; using a relatively interference-free approach drastically speeds up the neighbor discovery process.

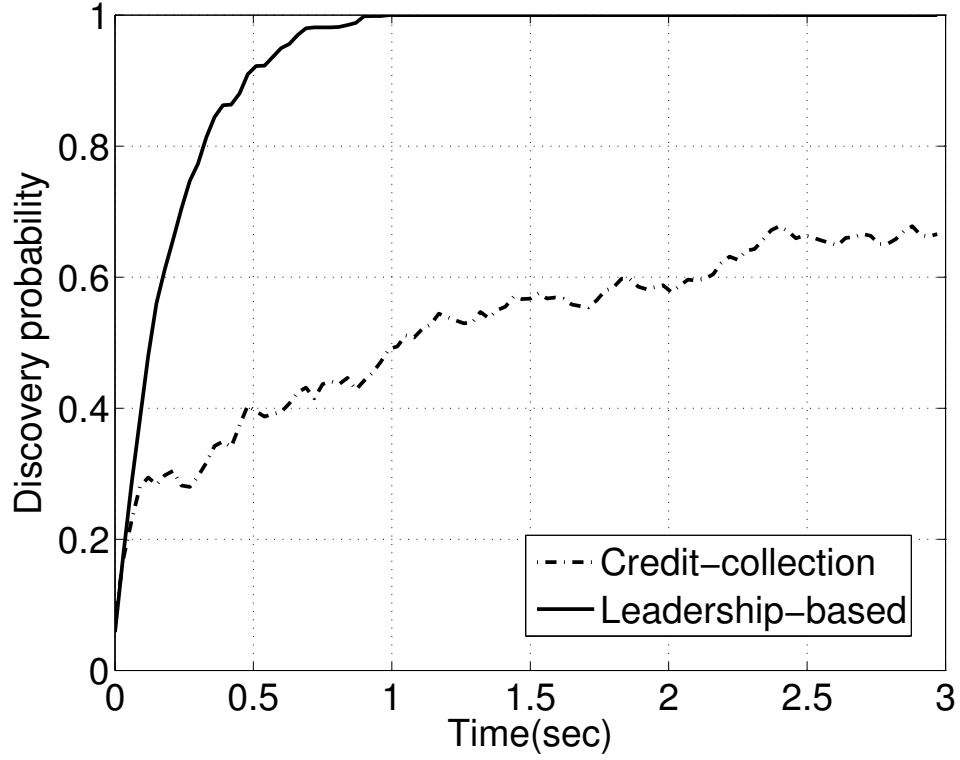


Figure 5.2: Comparison between leadership-based algorithm and credit-collection algorithm proposed in [3].

5.5 Improving fairness

Although not explicitly stated earlier, I wish to point out here that a node can assume the role of the leader multiple times. I expect that the neighbor discovery process is a background process that is continuously executed; this is essential since the neighborhoods of nodes could change either due to link failures, environmental changes (obstacles causing links to fail) or mobility. In this section, I consider the fairness of our approach in terms of the number of times a node gets an opportunity to become the leader.

To examine the fairness of our approach, I perform a simulation experiment, wherein I run the discovery process until all nodes discover almost all of their neighbors ($\geq 99\%$). The total simulation time was 3 seconds and node '0' was arbitrarily chosen to be the initial leader. Table 5.2 shows the number of times that each node is chosen to be the leader (referred to as *leader*

records). It can be seen that certain nodes have a better chance in neighbor discovery; in other words, an imbalance is observed. Node 1 is chosen to be the leader 29 times; however, node 8 is only chosen 12 times. Table 5.3 shows the leader records up to the first 0.54 seconds of the simulation. In this period, the percentage of neighbors discovered is on average 95% and 7 of the nodes had found all of their neighbors. I observe that node 0 and node 4 assumed the role of the leader 6 times each; many other nodes had the opportunity only twice. I also indicate in this table, the percentage of neighbors discovered within this time. Node 8 has discovered all of its neighbors even though it has been a leader just twice. Most nodes find all of their neighbors as long as they become a leader more than twice. This observation is encouraging in that, a node only has to serve as a leader a few times, in order for it to find its neighbors. If a node is chosen as a leader too often, it is likely to waste time and resources. Thus, it appears meaningful to provide equal opportunities of being a leader to all nodes in the network.

Table 5.2: Records of being the leader (time length = 3 secs)

Find 100% neighbors					
Node ID	0	1	2	3	4
Leader counts	22	29	14	13	18
Node ID	5	6	7	8	9
Leader counts	21	22	18	12	25

A modified approach to improve fairness: In order for all nodes to equally share the leadership duties, intuitively it would seem that nodes need to have a *count* of how many times each has served as a leader. Then, the leadership role can be passed onto the neighbor who has served the least number of times. This will ensure that the number of times that each node serves as the leader will be close to each other.

Table 5.3: Records of being the leader (time length = 0.54 secs)

Node ID	0	1	2	3	4
Leader counts	6	4	2	3	6
Neighbor percentage	1	1	0.75	0.89	1
Node ID	5	6	7	8	9
Leader counts	5	3	2	2	5
Neighbor percentage	1	1	0.81	1	1

To achieve this goal, I incorporate what I call *a leader table* in the notifier packet. This enlarges the size of notifier packets compared to what was used earlier (as in Table 5.1). Specifically, the size of the packet will increase by $(\#of\ nodes \times 8\ bits)/packet$. The first leader node (also called trigger node), say node 0, will create this table and mark itself as being the leader once. Once the notifier packet is received by the next leader node (say node 1), a new entry is added into the table to record that node 1 served as the leader once. This leader table is updated at each leadership transfer instance. In this way, I ensure that the current leader node possesses the most up-to-date leader table. Each leader node will choose the next leader with the least *experience* of being the leader. If multiple nodes are qualified to be the next leader, one of them is randomly chosen. The pseudo code below describes the process in detail.

K = total no. of directions;

Leader:

extract Leader_table from Notifier packet;

while rotation not finished yet **do**

if time T is up **then**

 ND_request.source_ID=self_id;

```

    ND_request.direc_ID=uniformly_choose(K);

    send ND_request;

    set  $T$ ;

else

    if receive ND_feedback then

        neighbor_ID=ND_feedback.source_ID;

        prev_direc=ND_feedback.prev_direc;

        PathLoss=ND_feedback.path_loss;

        PathLoss.node[neighbor_ID].direc[prev_direc]=PathLoss;

    end if

end if

end while

# of discovered neighbors is summarized here;

while  $i < \#$  of discovered neighbors do

    order PathLoss.node[ $i$ ].direc[*];

end while

select next_leader=Min(Leader_table[neighbor_ID]);

send Notifier packet to next_leader;

Other nodes:

if receive ND_request then

    neighbor_ID=ND_request.source_ID;

    prev_direc=ND_request.direc_ID;

    ND_feedback.path_loss=Tx_power/Rx_power;

     $t$ =uniformly_choose( $T$ );

    if  $t$  is up then

```

```

ND_feedback.source_ID=self_id;

ND_feedback.prev_direc=prev_direc;

send ND_feedback;

end if

end if

```

Evaluating the modified approach: Next, I present evaluations of our modified approach. Tables 5.4 and 5.5 show the number of times that each node in the network serves as a leader, when the overall percentage of neighbors discovered is approximately 100% and 95%, respectively. The results are from one randomly chosen realization. I observe that the variance in the counts (in Table 5.4) is relatively small; specifically, it is 0.44 compared to 26.84 in Table 5.2 with the original scheme. I see from Table 5.5 that all the nodes have been the leader, the same number of times; this means that the approach is fair. Both Table 5.3 and Table 5.5 reflect scenarios where each node found approximately 95% of its neighbors, successfully. However, the time incurred with the latter algorithm is only 0.42s; this represents a 22% reduction in time compared to the original approach. This reduction is a direct consequence of the increased efficiency with the modified scheme; nodes that have previously served as leaders and have found their neighbors do not waste time in serving as leaders again.

Table 5.4: Records of being the leader (time length = 3 secs)

Find 100% neighbors					
Node ID	0	1	2	3	4
Leader counts	20	19	20	20	18
Node ID	5	6	7	8	9
Leader counts	19	19	19	20	20

Table 5.5: Records of being the leader (time length = 0.42 secs)

Node ID	0	1	2	3	4
Leader counts	3	3	3	3	3
Neighbor percentage	0.89	1	1	1	0.94
Node ID	5	6	7	8	9
Leader counts	3	3	3	3	3
Neighbor percentage	1	1	1	0.71	1

Figure 5.3 depicts how the modified scheme improves the performance of neighbor discovery. I choose a 20-node scenario and the area of deployment is still 100 m \times 100 m. The maximum transmission range and transmission power are 50 m and 0.4 mW, respectively; these are the same as in Table 5.1. From Figure 5.3. I see that the time needed by every node for finding 95% its neighbors on average, with the basic leadership-based algorithm is about 1.62 seconds; this time is reduced to about 0.9 seconds with modified fair scheme. The modified scheme brings about a 45% performance improvement *after* taking into account the increase in packet transmission time due to the expansion of the notifier packet.

Finally, I examine how the time for neighbor discovery varies as I vary the number of nodes in the network. Figure 5.4 shows how the time required to discover 95% of the neighbors changes (on average), as I vary the number of nodes in the network. I retain the coverage area to be 100 m \times 100 m for each simulation point represented in the figure. The notifier packet length is also set to be identical to that in the scenario with 20 nodes; This treatment isolates the impact of node density from the incurred overhead changes from the notifier packets. Figure 5.4 shows that the more the nodes in the network, the longer a node takes for neighbor discovery as one might expect. More importantly, one can conclude that the time consumption is *proportional* to the number of nodes. The relationship is almost linear as seen in the figure.

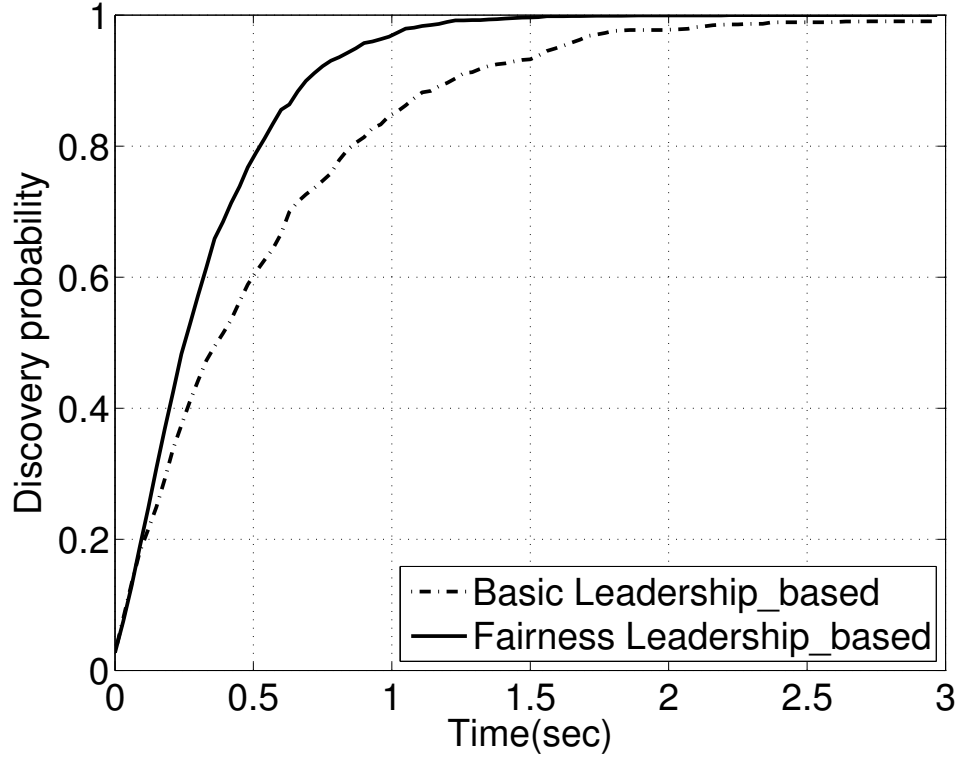


Figure 5.3: Comparison between schemes with or without fairness consideration.

As described earlier, our leadership-based algorithm attempts to construct an interference-free environment for the leader node to find its neighbors. However, with an increase in node numbers or network size, the time taken for neighbor discovery will increase. I further increase the node density (see Figure 5.5) and I find that the time taken grows almost linearly with the number of nodes. For very dense networks, as compared with the credit-collection algorithm, I found that the savings in terms of time get larger with increased node density. I use a curve fitting method to obtain extrapolated results for the leadership-based (solid line) and the credit-collection (dotted line) protocols, respectively. The curve fitting expression for the solid line is $0.4264 \times \exp(0.02799n)$ and the expression for the dotted line is $0.4937 \times \exp(0.03880n)$, where n stands for the number of nodes in the network. The slopes for both curves after differentiation of these expressions are obtained as $0.4264 \times 0.02799 \times \exp(0.02799n)$ and

$0.4937 \times 0.03880 \times \exp(0.03880n)$, respectively. For a fixed value of n , the slope of the curve for the credit-collection protocol is always larger than the one for the newly proposed leadership-based protocols. Thus, one might expect the difference between two curves to grow when the number of nodes increases; this can be observed in Figure 5.5.

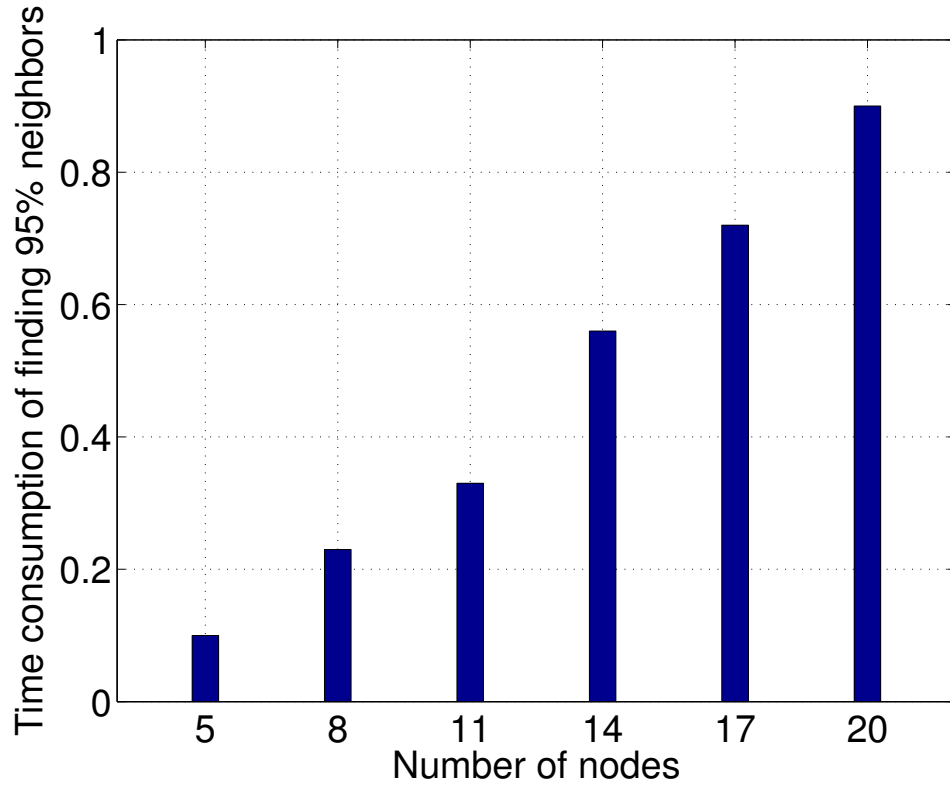


Figure 5.4: The time taken for neighbor discovery varies with number of nodes. The time shown is when 95% of neighbors are discovered.

In order to cover all the directions seamlessly, the number of installed transmitters should be inversely proportional to the transmission beam divergence of each Tx. For example, if the LED beam divergence is 60° , the number of transmitters should at least be 6 to cover all the directions. With more number of transmitters installed, the transmission beam divergence of each Tx can be reduced. Assuming that the transmission power is kept the same, small beam divergence results in longer transmission range and lower interference to other nodes.

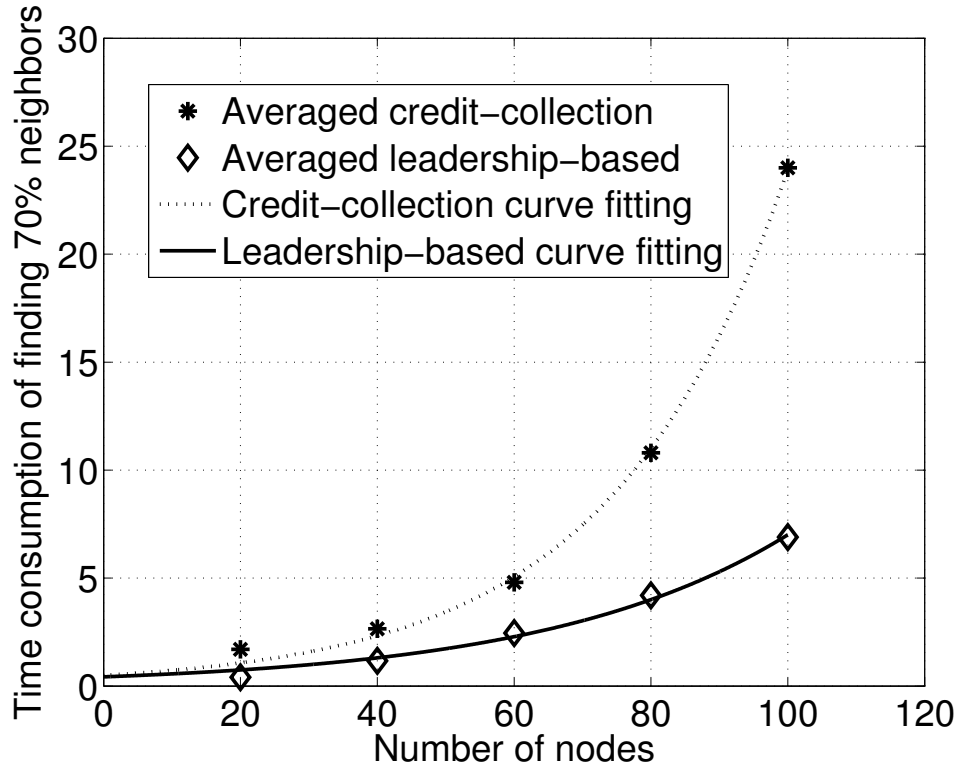


Figure 5.5: The time taken for neighbor discovery varies with number of nodes – a comparison of the leadership-based algorithm and the credit-collection algorithm. The time shown is when 70% of the neighbors are discovered, on average.

However, a large number of transmitters also implies that the time necessary for the neighbor discovery increases because the nodes have to search and rank more directions. Figure 5.6 shows the relationship between the time required and the number of transmitters. Each direction corresponds to one transmitter; for example the plot corresponding to 15 directions represents the scenario where the transceiver is equipped with 15 facets and 15 transmitters. From this figure, I conclude that the more directions, the longer the neighbor discovery process. For the four cases compared in Figure 5.6, in order to find 95% of neighbors on average, it takes 0.9 secs, 1.4 secs, 1.92 secs and 2.39 secs, for the cases with 6 directions, 9 directions, 12 directions, and 15 directions, respectively.

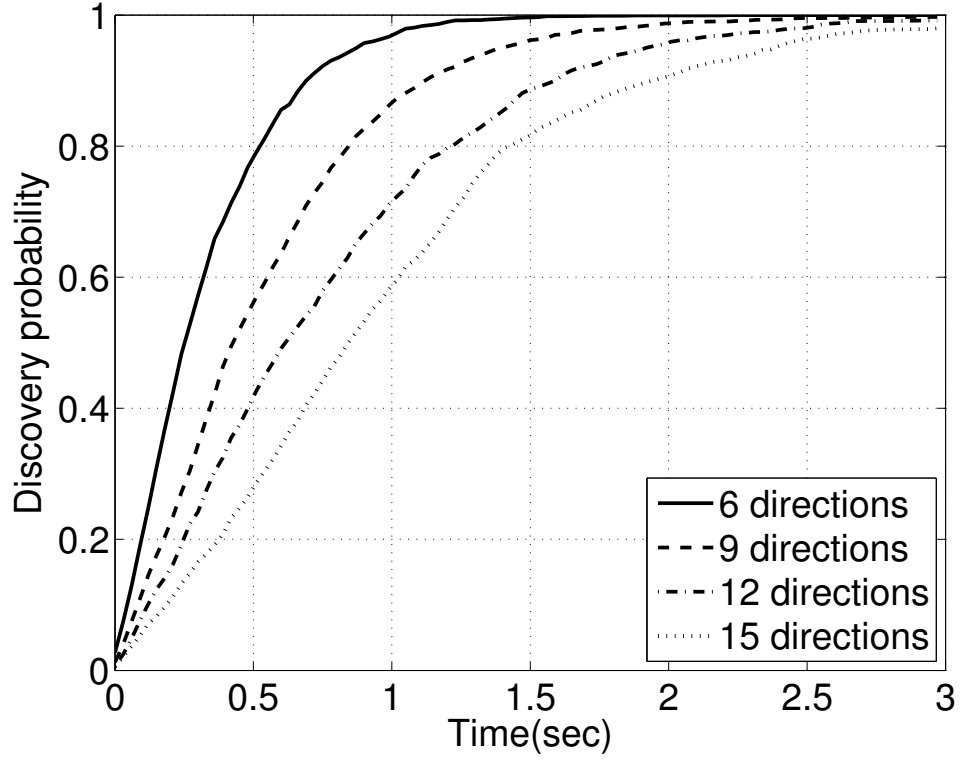


Figure 5.6: Performance with different numbers of directions. 20 nodes in total are distributed in the network.

5.6 Termination of Neighbor Discovery

In most application scenarios, it is important to bootstrap the network within a relatively short period. It is unlikely that a deployer will be able to pre-configure nodes with the specific topology; moreover, link qualities are likely to vary temporally. Our goal here is to determine when a neighbor discovery process can be considered to have terminated.

The scheme for terminating neighbor discovery: Achieving the above goal is far from trivial. Due to multi-user interference, feedback packets may collide, leading to information loss. As a consequence, a leader node is unlikely to collect all its neighborhood information by simply serving as the leader once. Thus, as discussed earlier, a node assumes the role of the leader multiple times. At each instance, it updates its neighborhood information with any data that is newly collected. If a node is unable to obtain new information upon becoming the

leader, it is likely that it has already obtained its complete neighborhood information. In fact, the more times this happens, the more confidence a node has in this conclusion. Thus, I make a modified rule that if a node does not acquire new information for a certain consecutive number of instances when it serves as a leader, it assumes that it does not need to be a leader anymore. It *marks* itself as being done with neighbor discovery. If all nodes have marked themselves as being done, then the procedure terminates. The information on which of the nodes are marked as above is recorded in a termination table. This table is exchanged in the notifier packets; thus, it is globally disseminated. I discuss this table later.

Each node maintains a counter which is initialized to '0'. Whenever it has acted as a leader but has not obtained any new neighborhood information, it increases this counter. If it does obtain new information, the counter is reset. When the counter value reaches a pre-defined threshold N , the node marks itself. When it transfers leadership, it updates the termination table to indicate that it is done with neighbor discovery. A simple bit corresponding to the nodes' IDs can be set to indicate that it is done. In other words, the termination table can simply be a bitmap which is equal in size to the number of nodes in the network.

With the information in the termination table, the current leader has the most up-to-date information and can make a timely and efficient decision on which node to choose as the leader next. Note here that this can be combined with the fairness criterion described earlier; however, I use this as the explicit criteria in the remainder of the section.

Evaluations: Figure 5.7 shows the percentage of neighbors discovered with time for a single realization from the perspective of an arbitrarily chosen node in the network. I simulate the 20-node scenario and other simulation settings are the same as described in Section 5.5. In this figure, I see that the node under consideration found 35% of its neighbors after the first instance of being the leader; this percentage increased to 75% after its second instance of being

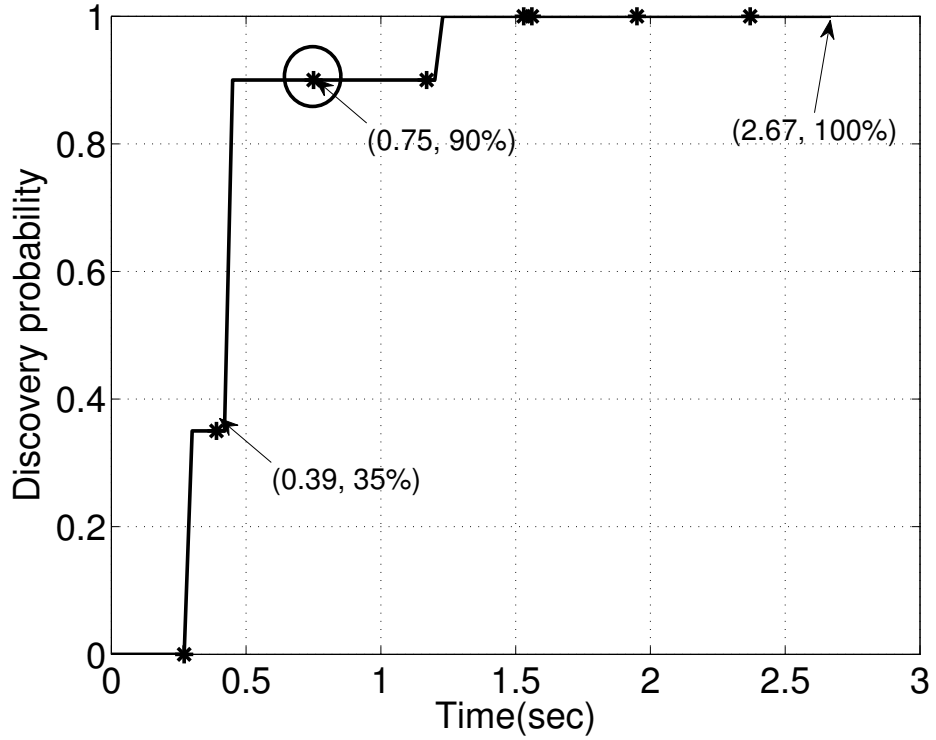


Figure 5.7: Illustrating the termination process. Solid line shows how the percentage of discovered neighbors increases with time; ‘*’s represent the instances when the node starts serving as the leader.

the leader. However, as shown by the circle in the plot, after the node served as the leader for the third time, there was no new information obtained; note however that, the neighbor discovery was not complete for the node. Although the counter increased by 1, it was reset after the node served as a leader for the fourth time, since new information was acquired. The neighbor discovery procedure finally ended at 2.67 seconds because the counter threshold was reached. At that point, the node had indeed discovered all of its neighbors.

Table 5.6 shows the total leader counts *after* every node found 100% of its neighbors. I set the termination counter threshold mentioned above to be 2. Interestingly, from Table 5.6, I observe that all the nodes except the one with node ID of 14 served as the leader without any information update, more than 2 times. This is because, node 14 was the final node in the neighbor

Table 5.6: Leader records after finding 100% neighbors

Node ID	0	1	2	3	4
Leader counts	6	4	5	7	4
Node ID	5	6	7	8	9
Leader counts	5	4	5	6	6
Node ID	10	11	12	13	14
Leader counts	5	6	6	4	2
Node ID	15	16	17	18	19
Leader counts	7	7	7	6	7

discovery process; unless its counter was set to 2, the process could not be terminated. However, node 14 could be assigned to be a leader only by one of its neighbors. In this case, nodes attempted to search for node 14 and interim also served as leaders again (the leadership token was passed around). Finally, the token was passed onto node 14 and the process terminated.

Figure 5.8 shows the performance of the protocol with the termination procedure with six scenarios of different node densities. I see the termination time is proportional to the node density as one may expect.

5.7 Summary

Neighbor discovery in UV networks is an important function that allows nodes to bootstrap the topology and begin operations. While there have been a plethora of proposals for neighbor discovery in the RF context, they are not suitable for a UV network given its unique PHY characteristics. In this chapter, I propose a novel neighbor discovery protocol for UV networks. The key idea is to eliminate interference by arbitrating the discovery process using leaders; a leader

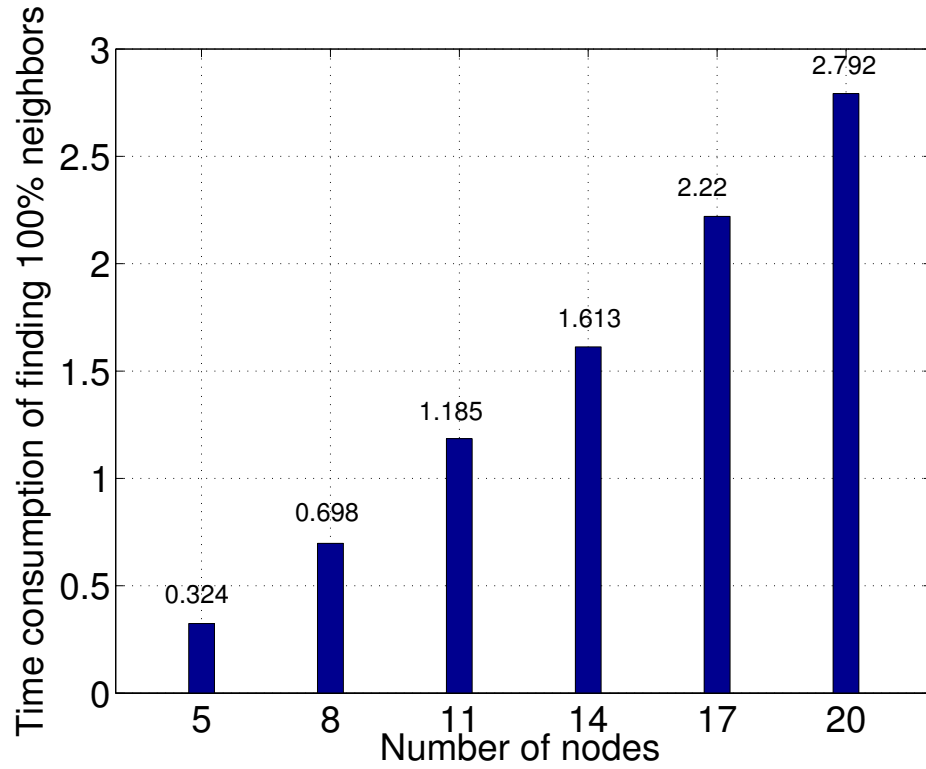


Figure 5.8: Illustration of the performance of the termination process with different node densities. All the nodes in the network find 100% of their neighbors.

is the only node that is allowed to perform neighbor discovery at any given time. The leadership role is passed on from node to node. I demonstrate that the protocol is extremely effective in performing neighbor discovery via extensive simulations that incorporate the UV PHY layer. In particular, the time needed for neighbor discovery process is decreased by as much as 90% as compared to the only existing neighbor discovery scheme for UV networks. I also provide extensive evaluations to capture the impact of various network and system parameters on the performance of our protocol.

Chapter 6

Connectivity of Wireless Ultraviolet Networks

NLOS optical communication can be enabled by modulating signals into an ultraviolet carrier and then transmitting through an atmospheric scattering channel. This chapter investigates some connectivity issues for such ultraviolet communication networks [53]. I discuss k -connectivity in a multi-user interference environment. Compared to the studied case without considering multi-user interference in which more users bring higher probability of k -connectivity, a large number of non-coordinated users cause higher interference and limit the network performance. Thus node density should be carefully designed in accordance with network configurations. Four typical scenarios are discussed, depending on whether each node transmitter is capable of adjusting its pointing angle and tracking a target receiver. They lead to different link losses and consequently the network k -connectivity properties. One of the cases simplifying the transceiver design for adjustable pointing is also illustrated, where each node is equipped with multiple transmitters to be activated via electronic on/off switching. The number of transmitters on a single node then becomes another critical parameter whose effect on

k-connectivity is studied.

6.1 Introduction

In a wireless sensor network (WSN), connectivity is critical for information to follow through the entire network smoothly. One approach is to let each sensor node transmit its collected information to a special node in the near field, named as sink node, where all the information from surrounding nodes is analyzed and/or further sent to a more powerful remote data processing unit. Due to power constraint at each sensor node, its transmission range is usually limited, thus multi-hop links are deployed for successful information delivery. Such an approach is efficient when all nodes and links are reliable. However, nodes and links might be vulnerable either due to the malfunction of a sensor or due to harsh propagation environments. Thus alternatively multiple transmission paths from a source node to a destination node are necessary. This also helps all the nodes to be able to communicate to each other through either a single-hop link or multi-hop links.

To achieve this goal, more than one neighbor is typically preferred in network design to prevent network from disconnection. This requires more nodes to be deployed. However, more nodes would introduce higher multi-user interference, which in turn reduces the transmission range of each node then increases the probability of disconnection. In addition, more nodes bring about higher cost for a given network area. Hence it is preferable to maintain a low node density while maximally covering an area. But an interesting question arises: *how many nodes should be deployed to cover an area to achieve a secured level of connectivity?*

To answer this question, one needs to define the connectivity of a network quantitatively. A terminology, k-connectivity, is defined to evaluate the degree of the network connectivity. The degree of a node is defined as the number of the node's neighbors, which are the nodes within the

transmission range of the node. For example, the degree of a node without any neighbor is zero. From the network point of view, the smallest value, d_{min} , for all the node degrees is defined as the minimum node degree for the entire network. Thus every node with a degree larger than zero is equivalent to $d_{min} > 0$. If a network satisfies $d_{min} > k$, I consider this network as a k -connected network, i.e., I can remove at most $k - 1$ links to ensure that the network is still connected [54].

Very recently, Vavoulas et al. presented the first paper on the connectivity issues of UV network [55]. They discussed the trade-off between node density/transmission power/data rate and k -connectivity, under the assumption that the transmitters and receivers of all the nodes point vertically and no MUI is considered. I further their work by incorporating the effect of MUI in k -connectivity analysis and also extend to multiple different scenarios in terms of Tx and Rx pointing and transceiver design. Various methods have been proposed for network connectivity in radio frequency (RF) communication networks [56, 57, 58, 59, 54, 60]. Since UV communication is different from RF communication due to its unique propagation properties, transceiver design and signal processing techniques, it is necessary to study connectivity for emerging UV networks.

6.2 Path Loss and Network Models

To analyze the connectivity of a network, I have to choose a suitable path loss model first to evaluate the power decay after UV propagation in the atmosphere. Various models have been proposed in the literature including single scattering models [22, 28, 23, 61] and multiple scattering models [24, 62, 25]. In this work, I adopt a simplified empirical path loss model [2] validated by outdoor experiments. The model has been applied in studying UV communication networks [50, 3, 63]. Secondly, the behavior of nodes should be specified. It includes the

location or the spatial distribution of nodes and the rules they have to follow regarding message transmission. I will follow the Poisson spatial distribution widely used in stochastic geometry research [36, 63].

6.2.1 Path Loss Model

I adopt the empirical non-coplanar path loss model proposed in Section 2.3. To make this chapter self-contained, I restate the model as follows

$$L = \xi r^\alpha e^{b\phi}, \quad (6.1)$$

where r is the horizontal distance between Tx and Rx, ξ is the path loss factor, α is the path loss exponent, and b is the off-axis angle exponent factor. This model is capable of describing the non-coplanar geometry, i.e., the transmission beam axis and Rx FOV axis are not on the same plane. ϕ describes the Tx off-axis angle in radians which is the angle between the horizontal base line connecting Tx and Rx and the projection of transmission beam axis onto the ground. Correspondingly, Rx off-axis angle is defined as the angle between the horizontal base line and the projection of FOV axis onto the ground. The above model considers Rx off-axis angle as zero because Rx pointing angle is assumed to be 90° so that the projection of the FOV axis is a point which is always on the Tx-Rx base line. All the subsequent off-axis angles are referring to Tx off-axis angles without being specified otherwise. The analysis in [50] showed that ξ , α and b are only related to Tx/Rx pointing angles, transmission beam and FOV.

This model is able to describe the scenario in which Tx points at an arbitrary direction but Rx points vertically. Although it cannot encompass all possible geometries, to the best of our knowledge, it is one of the most convenient path loss models in network analysis so far. There are mainly two reasons. First, directional Tx with omni-directional Rx is a reasonable configuration for a UV network to maintain low complexities of MAC and network protocol design.

Second, this model is simple and easy to use to account for non-coplanar geometry and multiple scattering. Although some other non-coplanar path loss models are also available [1, 61, 64], they are better for link loss evaluation rather than network analysis because their complexity prevents multi-stage derivations typically encountered in network performance study.

6.2.2 Distribution of Node Location

In practice, the node distribution depends on the specific network. To accommodate most network scenarios of interest, I consider a generic stochastic geometry. The distribution of node locations follows homogeneous Poisson point process (PPP) with parameter λ as the node density, which is the expected number of nodes per unit area. PPP is considered as a uniform distribution if λ is a constant because the expected number of nodes in a region is proportional to the area of this region. The probability of m nodes in a region A with area of S is given by

$$\Pr[m \text{ in A}] = \frac{e^{-\lambda S} (\lambda S)^m}{m!}. \quad (6.2)$$

6.2.3 Distribution of Distance and Off-axis Angle

To study the connectivity and MUI issues, I randomly pick a node and take the position of this node as the origin. The distance between the chosen node and any interference node is r_i .

The probability density function (PDF) of the distance is given as follows

$$f_{r_i}(r) = \begin{cases} \frac{2r}{R^2 - R_o^2}, & R_o \leq r \leq R \\ 0, & \text{otherwise} \end{cases}, \quad (6.3)$$

where R is the radius of the network, and R_o is the guard distance to make two nodes physically separated rather than co-located. Typically, R_o could take a value less than 0.1m.

Since the Tx pointing direction is random, the off-axis angle ϕ_i between the i th interference

node and the chosen node follows the uniform distribution in the range of $[0, \pi]$

$$f_{\phi_i}(\phi) = \begin{cases} \frac{1}{\pi}, & 0 \leq \phi \leq \pi \\ 0, & \text{otherwise} \end{cases}. \quad (6.4)$$

The above two distributions result in the uniform node distribution presented in Section 6.2.2.

These model assumptions are applicable to most scenarios.

6.3 Connectivity Modeling

With above defined models, I can derive the probability of k-connectivity in more detail. Based on the definition of d_{min} , i.e., the smallest node degree within the network, the probability of k-connectivity is expressed as follows

$$\Pr[d_{min} > k] = \prod_{i=1}^n \Pr[d_i > k], \quad (6.5)$$

where n is the total number of nodes in the network and d_i is the connectivity degree of the i th node. Based on Eq. (6.2), I can derive

$$\Pr[d_i > k] = \sum_{m=k+1}^{\infty} \frac{e^{-\lambda S_i} (\lambda S_i)^m}{m!}, \quad (6.6)$$

where S_i represents the area within the transmission range of the i th node. Any nodes in this area are regarded as the neighbors of the i th node. Neighbor node here, is defined as the node which can receive the signal from the center node successfully on average under the effect of MUI from other nodes.

Substituting Eq. (6.6) into Eq. (6.5), I obtain

$$\Pr[d_{min} > k] = \prod_{i=1}^n \sum_{m=k+1}^{\infty} \frac{e^{-\lambda S_i} (\lambda S_i)^m}{m!}. \quad (6.7)$$

As mentioned in Section 6.1, the transceivers can be configured in tremendous ways, which leads to different S_i . Next, I will discuss different scenarios in terms of transceiver configuration in the following subsections.

6.3.1 Scenario I

First, I consider a scenario in which each node is equipped with vertically pointing Tx and Rx. In this case the coverage area of a node is a circle, completely determined by transmission range r_i as

$$S_i = r_i^2 \pi. \quad (6.8)$$

Here, r_i is related to multiple factors and analyzed below.

The network connectivity for this scenario is investigated in [55] but under an assumption of free multi-user interference (MUI). This assumption is acceptable when sophisticated multi-user mechanisms are deployed or coordinated multiple access protocol is developed. However, there is neither suitable multi-user detection scheme nor efficient multiple access scheme for deployment of an inexpensive UV WSN so far. If I neglect MUI or assume it can be controlled to a low level, the more nodes I have in the network, the higher degree of connectivity I can achieve. Unfortunately, in most scenarios, MUI is an inevitable adverse factor to impact network performance. Typically, the number of interference nodes would be relatively large, thus MUI could be modeled as Gaussian noise, i.e., $P_I \sim N(\mu_I, \sigma_I^2)$, where P_I is MUI, μ_I and σ_I^2 are the expected value and the variance of P_I , respectively. I assume Gaussian background noise. In [65], the minimum achievable transmission ranges for both OOK and PPM in Gaussian noise have been derived as follows

$$r_{OOK_G} = \sqrt[\alpha]{\frac{\eta P_t}{\xi Q^{-1}(P_e)} \left(\frac{1}{N_o R_b}\right)^{\frac{1}{2}}}, \quad (6.9)$$

and

$$r_{PPM_G} = \sqrt[\alpha]{\frac{\eta P_t}{\xi Q^{-1}(P_e)} \left(\frac{K \log_2 K}{2 N_o R_b}\right)^{\frac{1}{2}}}, \quad (6.10)$$

where P_t is the transmission power, P_e is the bit error rate (BER), N_o is the power spectral density (PSD) of background noise, R_b is the data rate, K is the number of slots in a PPM

symbol, η is the Rx efficiency, which is the product of optical filter transmission and PMT quantum efficiency, and $Q^{-1}()$ is inverse Q-function.

To incorporate the effect of MUI, Eqs. (6.9) and (6.10) are modified as

$$r_{OOK_G} = \sqrt[\alpha]{\frac{\eta P_t}{\xi Q^{-1}(P_e)} \left(\frac{1}{N_o R_b + \sigma_I^2} \right)^{1/2}}, \quad (6.11)$$

and

$$r_{PPM_G} = \sqrt[\alpha]{\frac{\eta P_t}{\xi Q^{-1}(P_e)} \left[\frac{K \log_2 K}{2(N_o R_b + \sigma_I^2)} \right]^{1/2}}. \quad (6.12)$$

Here I treat MUI as background noise when detecting a signal.

Next, I derive the power of P_I , i.e. σ_I^2 . For simplicity, assume each node transmits at the same power level and all the nodes have the same FOV, filter transmission and Tx/Rx pointing angles. Using the path loss model by Eq. (6.1), P_I is expressed as

$$P_I = \sum_{i=1}^n d_i \frac{\eta P_t}{\xi r_i^\alpha e^{b\phi_i}}, \quad (6.13)$$

Here, $\phi_i = 0$ because both the Tx and Rx pointing angles are 90° . d_i is an indicator which equals 1 when the i th node is transmitting with probability p and 0 if the i th node is idle with probability $1 - p$. Thus the PDF of d_i is

$$f_{d_i}(d) = p\delta(d - 1) + (1 - p)\delta(d), \quad (6.14)$$

Eq. (6.13) is simplified as

$$P_I = \eta \frac{P_t}{\xi} \sum_{i=1}^n d_i \frac{1}{r_i^\alpha}. \quad (6.15)$$

In the above expression, both d_i and r_i are random variables. Thus P_I is a function of these two random variables. I am interested in the mean and variance of P_I . For shorter notations, let $W_i = d_i/r_i^\alpha$ and $Y_i = r_i^\alpha$. Then I have $W_i = d_i/Y_i$. The PDF of Y_i is

$$f_{Y_i}(y) = \begin{cases} \frac{2}{\alpha} \frac{1}{R^2 - R_o^2} y^{\frac{2}{\alpha}-1}, & R_o^\alpha \leq y \leq R^\alpha \\ 0, & \text{otherwise} \end{cases}. \quad (6.16)$$

Since the PDFs of Y_i and d_i are both known, the PDF of W_i is derived as

$$f_{W_i}(w) = \begin{cases} 1 - p, & w = 0 \\ \frac{2}{\alpha} \frac{p}{R^2 - R_o^2} w^{-\frac{2}{\alpha}-1}, & R^{-\alpha} \leq w \leq R_o^{-\alpha} \end{cases}. \quad (6.17)$$

With the PDF of W_i , the expected value and the variance of W_i are derived as follows

$$E[W_i] = \frac{2}{\alpha - 2} \frac{p}{R^2 - R_o^2} (R_o^{2-\alpha} - R^{2-\alpha}), \quad (6.18)$$

and

$$Var[W_i] = \frac{p[R_o^{2(1-\alpha)} - R^{2(1-\alpha)}]}{(\alpha - 1)(R^2 - R_o^2)} - \left[\frac{2p(R_o^{2-\alpha} - R^{2-\alpha})}{(\alpha - 2)(R^2 - R_o^2)} \right]^2. \quad (6.19)$$

Based on Eq. (6.15) and above two equations, the expected value and the variance of P_I are

$$\mu_I = \eta \frac{nP_t}{\xi} E[W_i], \quad (6.20)$$

and

$$\sigma_I^2 = \eta^2 \frac{nP_t^2}{\xi^2} Var[W_i]. \quad (6.21)$$

Substituting Eqs. (6.20) and (6.21) into Eqs. (6.11) and (6.12), I have

$$r_{OOK_G} = \sqrt[\alpha]{\frac{\eta P_t}{\xi Q^{-1}(P_e)} \left(\frac{1}{N_o R_b + \eta^2 \frac{P_t^2}{\xi^2} n Var[W_i]} \right)^{1/2}}, \quad (6.22)$$

and

$$r_{PPM_G} = \sqrt[\alpha]{\frac{\eta P_t}{\xi Q^{-1}(P_e)} \left[\frac{K \log_2 K}{2(N_o R_b + \eta^2 \frac{P_t^2}{\xi^2} n Var[W_i])} \right]^{1/2}}. \quad (6.23)$$

Further substituting Eqs. (6.22) and (6.23) into Eq. (6.8), respectively, and then the expression of S_i into Eq. (6.7), I can obtain the probability of k-connectivity with both OOK and PPM in this scenario.

To evaluate the k-connectivity performance numerically, I choose the parameters in Table 6.1.

Figure 6.1 shows $\Pr[d_{min} > k]$ versus node density λ for OOK modulation when MUI is considered in the proposed approach and neglected in [55]. The two cases have the similar

Table 6.1: Scenario I parameter settings

Tx average power P_t	50 mW
Data rate R_b	10 kbps
PSD of Background noise N_o	1.14×10^{-31} W/Hz
The guard distance R_o	0.05 m
Path loss factor ξ	1.6×10^9
Path loss exponent α	1.23
Transmission probability p	4×10^{-5}
Tx pointing angle	90°
Rx pointing angle	90°
Tx beam full-width angle	17°
FOV	30°
Rx efficiency η	0.045
Number of nodes n	500

performance. Note that the transmission probability p is only 4×10^{-5} . To understand how small this number is, I can multiply p with the total number of nodes in the network, n . The result is 0.02, which is the expected value of the total concurrent transmitting nodes at any time. In other words, a node has to wait for a long time to send a message.

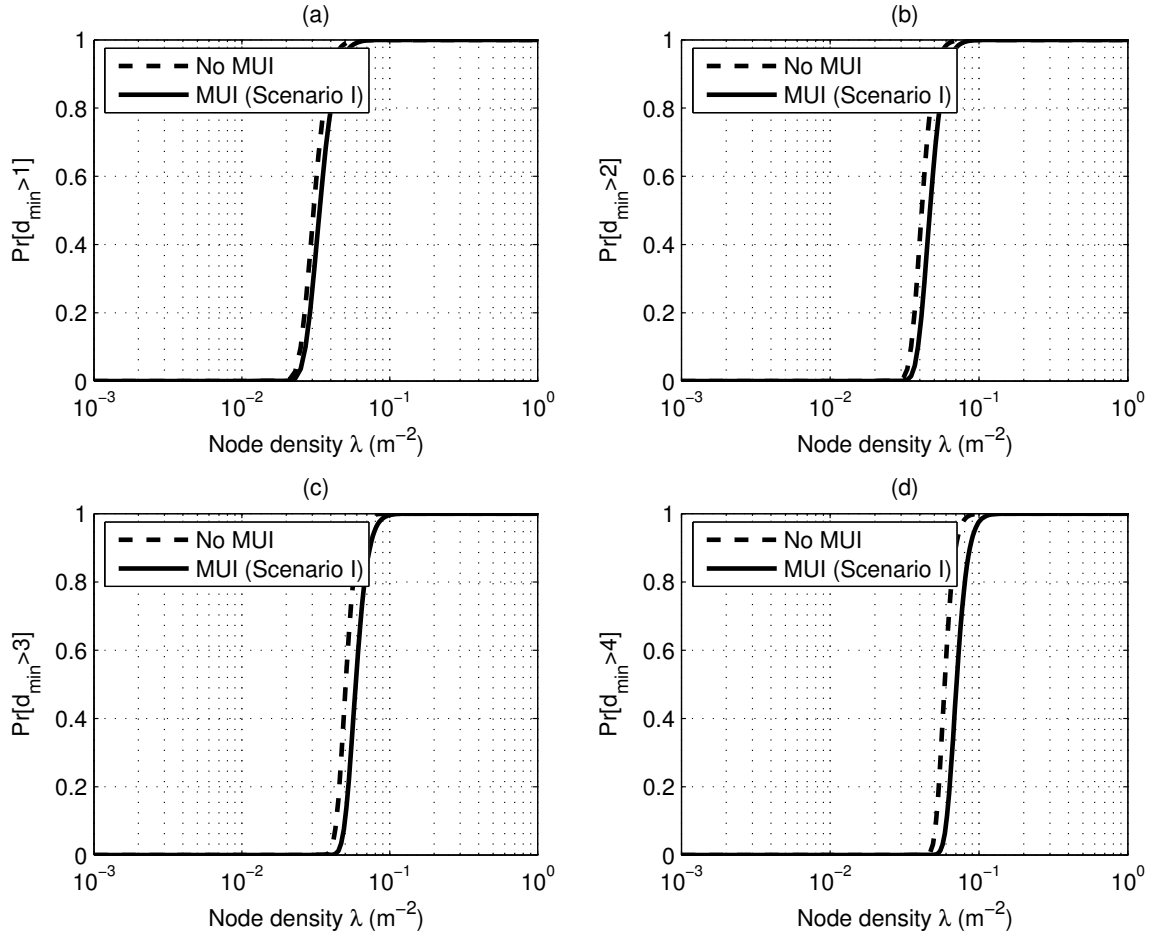


Figure 6.1: $\Pr[d_{min} > k]$ versus node density λ with OOK modulation in Scenario I.

In order to demonstrate how $\Pr[d_{min} > k]$ changes with transmission probability p , I plot Figure 6.2. I observe that the node density λ grows rapidly for $\Pr[d_{min} > 2]$ to achieve 1, which means with the same number of nodes, the covered area is much smaller. From these results, I can conclude that if all the nodes are equipped with omni-directional Tx and Rx and

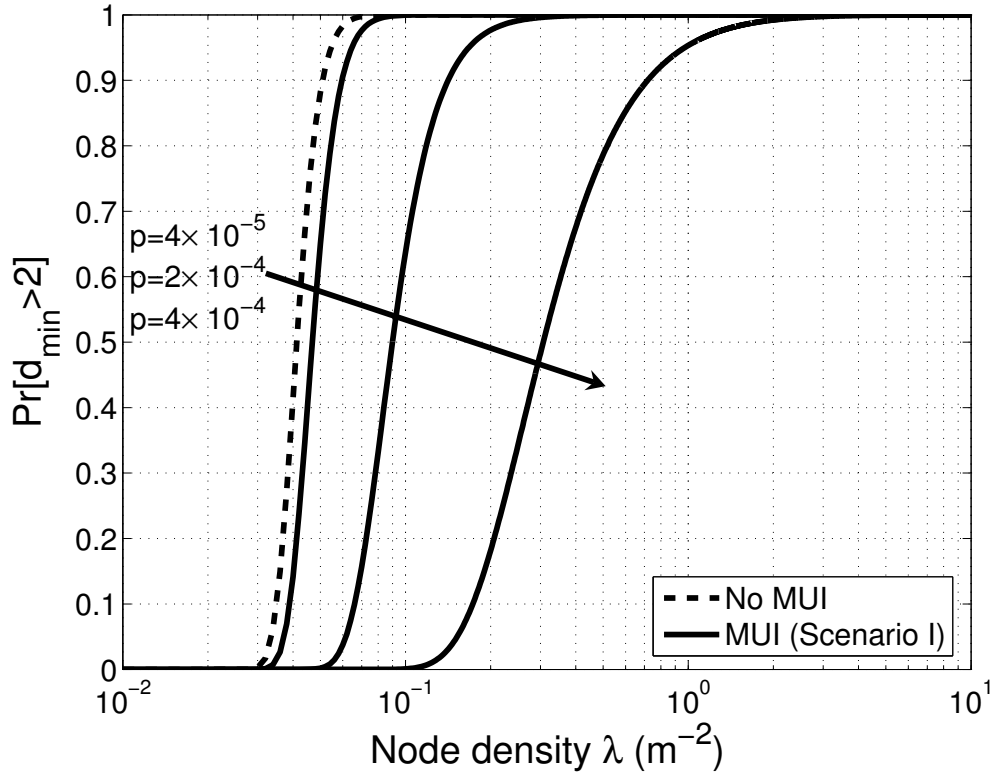


Figure 6.2: Effect of transmission probability on $\text{Pr}[d_{\min} > k]$ in Scenario I.

no multi-access scheme is implemented, the k -connectivity is an expensive task, since I have to deploy too many nodes for just a small area. Take Figure 6.2 as an example, if the transmission probability is 4×10^{-4} , the node density should be at least 2 m^{-2} . Thus 500 nodes can only cover 250 m^2 . This is unaffordable for typical application scenarios.

6.3.2 Scenario II

Based on the results in the previous subsection, I shall discuss another system geometry. In this scenario, the Tx of each node can be driven to any direction and Rx is still vertically pointing. I assume that the nodes have the knowledge of where their target receiving nodes are based on certain algorithms, such as neighbor discovery [3]. Thus, the transmission can be directed exactly to the target node, which means the off-axis angle for the desired link is still

zero. And the link loss decreases because of the aligned transmission. Although the coverage area is not a circle when the direction of Tx is fixed, the area in our analysis is still a circle because Tx can be adjusted to any direction. For transmissions from interference nodes, no coordination is made. So from the network point of view, the distribution of the off-axis angle of an interference node is uniform and follows Eq. (6.4).

The arbitrary and random off-axis angles of interference nodes complicate the analysis and lead to a new expression for P_I simplified as

$$P_I = \eta \frac{P_t}{\xi} \sum_{i=1}^n d_i \frac{1}{r_i^\alpha e^{b\phi_i}}. \quad (6.24)$$

Note that, the term $e^{b\phi_i}$ remains, different from Eq. (6.15).

Next, I will find some statistics of P_I . Let $X_i = d_i/r_i^\alpha e^{b\phi_i}$, $Y_i = r_i^\alpha$, $Z_i = e^{b\phi_i}$ and $W_i = d_i/Y_i$. Thus I have $X_i = W_i/Z_i$. Based on the PDF of ϕ_i , the PDF of Z_i is obtained as

$$f_{Z_i}(z) = \begin{cases} \frac{1}{\pi b z}, & 1 \leq z \leq e^{b\pi} \\ 0, & \text{otherwise} \end{cases}. \quad (6.25)$$

So far, both the PDFs of W_i and Z_i are known. The PDF of X_i is derived as

$$f_{X_i}(x) = \begin{cases} \frac{p(\frac{R^2}{x} - x^{-\frac{2}{\alpha}} e^{-\frac{2}{\alpha} b\pi})}{\pi b(R^2 - R_o^2)}, & \frac{R^{-\alpha}}{e^{b\pi}} \leq x \leq R^{-\alpha} \\ \frac{p(1 - e^{-\frac{2}{\alpha} b\pi})x^{-\frac{2}{\alpha}-1}}{\pi b(R^2 - R_o^2)}, & R^{-\alpha} \leq x \leq \frac{R_o^{-\alpha}}{e^{b\pi}} \\ \frac{p(x^{-\frac{2}{\alpha}-1} - \frac{R_o^2}{x})}{\pi b(R^2 - R_o^2)}, & \frac{R_o^{-\alpha}}{e^{b\pi}} \leq x \leq R_o^{-\alpha} \\ 0, & \text{otherwise} \end{cases}, \quad (6.26)$$

if $R^{-\alpha} < R_o^{-\alpha}/e^{b\pi}$; and if $R^{-\alpha} > R_o^{-\alpha}/e^{b\pi}$, I have

$$f_{X_i}(x) = \begin{cases} \frac{p(\frac{R^2}{x} - x^{-\frac{2}{\alpha}} e^{-\frac{2}{\alpha} b\pi})}{\pi b(R^2 - R_o^2)}, & \frac{R^{-\alpha}}{e^{b\pi}} \leq x \leq \frac{R_o^{-\alpha}}{e^{b\pi}} \\ \frac{p}{\pi b} \frac{1}{x}, & \frac{R_o^{-\alpha}}{e^{b\pi}} \leq x \leq R^{-\alpha} \\ \frac{p(x^{-\frac{2}{\alpha}-1} - \frac{R_o^2}{x})}{\pi b(R^2 - R_o^2)}, & R^{-\alpha} \leq x \leq R_o^{-\alpha} \\ 0, & \text{otherwise} \end{cases}. \quad (6.27)$$

Although it takes different forms for different cases, the expected value and variance of X_i have the same form

$$E[X_i] = \frac{2p(1 - \frac{1}{e^{b\pi}})(R^{2-\alpha} - R_o^{2-\alpha})}{(2 - \alpha)\pi b(R^2 - R_o^2)}, \quad (6.28)$$

and

$$Var[X_i] = \frac{p(1 - \frac{1}{e^{2b\pi}})[R^{2(1-\alpha)} - R_o^{2(1-\alpha)}]}{2(1 - \alpha)\pi b(R^2 - R_o^2)}. \quad (6.29)$$

Thus the expected value and variance of P_I are

$$\mu_I = \eta \frac{P_t}{\xi} n E[X_i], \quad (6.30)$$

and

$$\sigma_I^2 = \eta^2 \frac{P_t^2}{\xi^2} n Var[X_i]. \quad (6.31)$$

Substituting the above two equations into Eqs. (6.11) and (6.12), then into Eqs. (6.8) and (6.7), I can obtain results for the probability of k-connectivity analytically. Numerical performance is presented by Figure 6.3. The parameters taking values different from Table 6.1 are listed in Table 6.2.

Table 6.2: Scenario II parameter settings

Path loss factor ξ	1×10^9
Path loss exponent α	1.05
Off-axis angle exponent factor b	0.5213
Transmission probability p	4×10^{-4}
Tx pointing angle	60°

The probability of k-connectivity in this scenario approaches 1 with even smaller node density λ than the case without considering MUI, and is much better than in Scenario I. The large

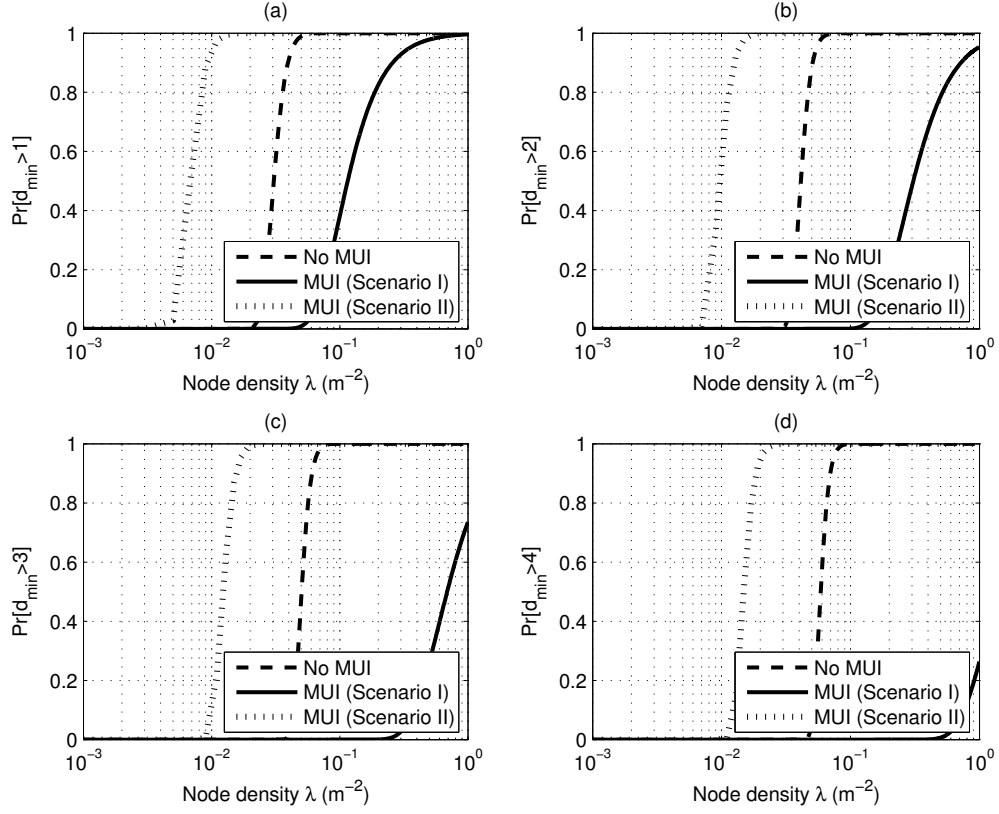


Figure 6.3: $\Pr[d_{min} > k]$ versus node density λ with OOK modulation in both Scenario I and II.

improvement is brought by the directional Tx and the knowledge about target Rx. The directional Tx greatly reduces the link loss and thus increases the transmission range. As mentioned at the beginning of this subsection, Tx can point to any direction. Therefore, the coverage area is still a circle. The increased transmission range means the radius of the circle increases, and consequently the increased coverage area. Moreover, the interference nodes can only interfere one direction at a time, thus the interference level greatly decreases. All these jointly lead to significantly improved k -connectivity. To achieve 2-connectivity, the node density is only required to be $2 \times 10^{-2} \text{m}^{-2}$. So, for example, 500 nodes can cover $25,000 \text{m}^2$, which is one hundred times as that in Scenario I with the same transmission probability.

6.3.3 Scenario III

In Subsection 6.3.2, I analyzed the case in which nodes can track the target Rx. If the Tx is still directional but cannot track the target Rx, the analysis of k-connectivity becomes more complicated. In this case, the off-axis angle of the desired link is not zero any more, thus the corresponding path loss grows, which results in worse probability of k-connectivity. However, if the Tx can point in any direction from 0° up to 360° , there is no difference with Scenario II because the essence of k-connectivity is to have k neighbors at least for each node in the network rather than to communicate to a specific node at specific time. Thus even a node has no idea about where its target receiving nodes are, any nodes around it within certain distance can always finally be in coplanar geometry with it as long as its Tx can adjust its pointing direction.

Therefore, let's assume the Tx of each node cannot rotate, i.e., relaxing the requirement on the hardware of the nodes. The significant change brought by this assumption is that the coverage area is no longer a circle but similar to a sector. Figure 6.4 shows a typical shape of the coverage area in this case. The parameters used are the same as Scenario II. λ is set to be 0.1. The hexagon in the figure stands for the transmission node. The arrow shows the transmission direction. So any node on the boundary of the area can achieve a BER of 1×10^{-3} on average.

Since the off-axis angles of target links are not zero in this scenario, the transmission ranges are re-derived as follows

$$r_{OOK_G} = \sqrt[\alpha]{\frac{\eta P_t}{\xi e^{b\phi} Q^{-1}(P_e)} \left(\frac{1}{N_o R_b + \eta^2 \frac{P_t^2}{\xi^2} n E[X_i]} \right)^{\frac{1}{2}}}, \quad (6.32)$$

and

$$r_{PPM_G} = \sqrt[\alpha]{\frac{\eta P_t}{\xi e^{b\phi} Q^{-1}(P_e)} \left[\frac{K \log_2 K}{2(N_o R_b + \eta^2 \frac{P_t^2}{\xi^2} n \text{Var}[W_i])} \right]^{\frac{1}{2}}}. \quad (6.33)$$

Here, ϕ is the off-axis angle between Tx and desired Rx. The coverage area becomes

$$S_i = 2 \int_0^\pi \int_{R_o}^{r_{OOK_G}} r dr d\phi. \quad (6.34)$$

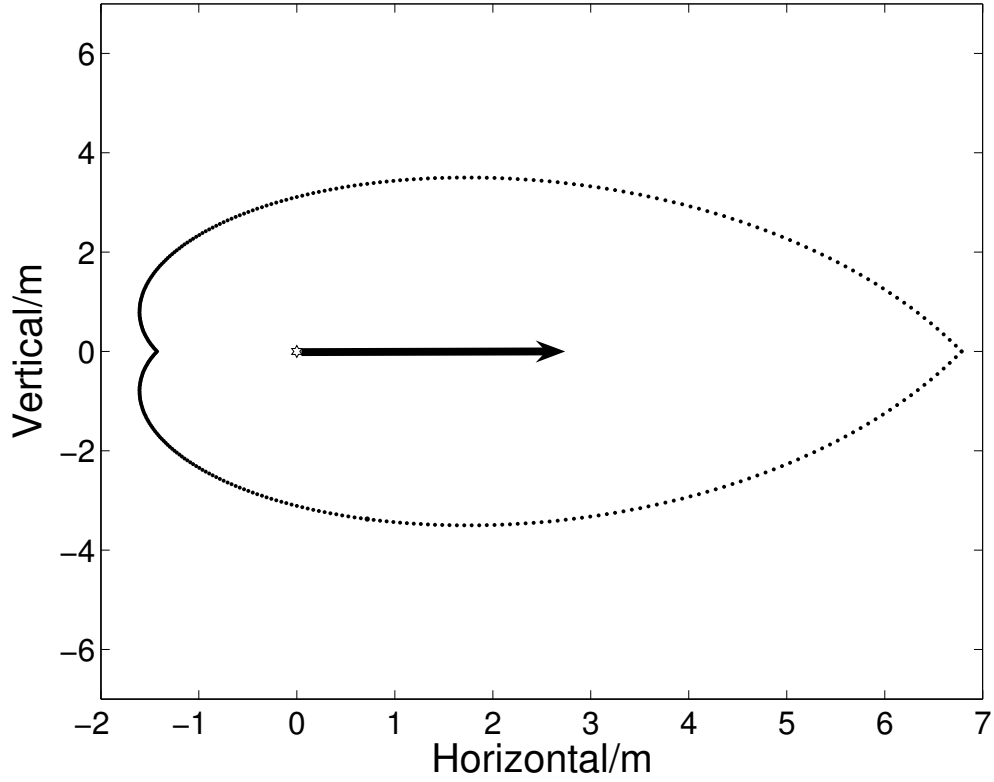


Figure 6.4: The shape of the coverage area with Tx pointing angle 60° .

By substituting Eq. (6.32), Eq. (6.34) is manipulated as

$$S_i = \frac{\alpha}{2b} \left[\frac{\eta P_t}{\xi Q^{-1}(P_e)} \left(\frac{1}{N_o R_b + \sigma_I^2} \right)^{\frac{1}{2}} \right]^{\frac{2}{\alpha}} (1 - e^{-\frac{2}{\alpha} b \pi}). \quad (6.35)$$

Substituting Eq. (6.35) in Eq. (6.7), I obtain the probability of k-connectivity in Scenario III.

The results are compared with Scenarios I and II in Figure 6.5. I observe that in Scenario III, the probability of k-connectivity approaches 1 with a very large node density λ . This is because the Tx cannot change its transmission direction such that the coverage area is much smaller than Scenarios I and II. With above results, I conclude that the abilities to track the direction of the desired node and adjust the transmission direction to the desired direction are very important for a UV network.

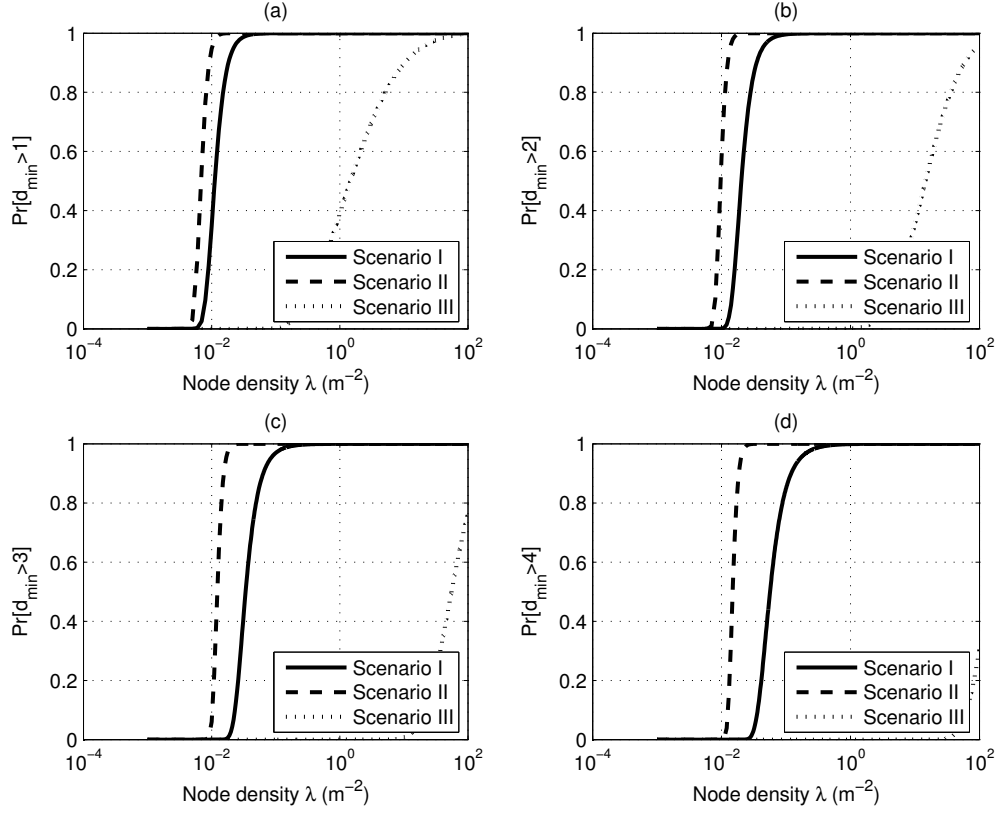


Figure 6.5: $\Pr[d_{min} > k]$ versus node density λ with OOK modulation in Scenarios I, II and III.

6.3.4 Scenario IV

In Scenario II, I assumed a node has only one Tx, which can be rotated to exactly track the desired Rx based on neighbor discovery algorithms [3], such that the off-axis angle ϕ between Tx and target Rx is zero. In Scenario III, I assume the Tx has no ability to track desired Rx at all. Thus ϕ is uniformly distributed within $[0, \pi]$.

However, many cases in practice are actually in between. For Scenario II, the results of neighbor discovery may not be accurate. Even the theoretical results are accurate, the error of mechanical driving devices may still result in a nonzero off-axis angle. Therefore, the distribution of ϕ in practice is

$$f_{\phi_i}(\phi) = \begin{cases} \frac{1}{\Phi}, & 0 \leq \phi \leq \Phi \\ 0, & \text{otherwise} \end{cases}, \quad (6.36)$$

where Φ is the upper bound for the off-axis angle ϕ . The value of Φ is partially determined by the design of neighbor discovery algorithms, which are discussed for the first time for a UV network in [3]. In [3], multiple transmitters are mounted on a node with the same apex angles and transmission beam divergence but different azimuth angles. I call this configuration as switching transmission, rather than rotation transmission as in Scenario II. This design is more reliable because it does not need a mechanical device to drive the rotation. After the neighbor discovery procedure, the node is able to know which Tx should be used to achieve the best link quality. However, even the node chooses the best direction to send, it is very likely that the off-axis angle is still not zero. For example, the number of transmitters in the node is N_t . If N_t approaches infinity, this scenario becomes Scenario II. Thus Scenario II is in fact a special case of Scenario IV being discussed in this section. In practice, N_t is a number less than 10, and 6 is used in [50] and [3]. Intuitively, the inaccuracy of the best direction introduces more power loss for the desired link due to non-coplanar geometry. And the performance of k-connectivity is affected negatively. A large value of N_t increases the complexity of the transceiver design and also the cost, while a small N_t causes performance degradation. It is necessary to analyze how N_t affects the performance of k-connectivity.

Based on the above analysis, I have the relationship between Φ and N_t

$$\Phi = \frac{\pi}{N_t}. \quad (6.37)$$

Following the design of [50] and [3], an individual Tx cannot rotate. The tracking ability is achieved by activating a Tx among all N_t transmitters on a single node to the direction of interest. So the shape of coverage area is different from any above scenario, but assembled by several coverage areas shown in Figure 6.4. In order to simplify the derivation, I approximate the coverage area still as a circle with radius of r_{OOK_G} , which is defined in Eq. (6.32). Since ϕ

is a random variable, the average value of r_{OOK_G} is derived as follows

$$\overline{r_{OOK_G}} = \frac{N_t \alpha}{b\pi} \left[\frac{\eta P_t}{\xi Q^{-1}(P_e)} \left(\frac{1}{N_o R_b + \sigma_I^2} \right)^{\frac{1}{2}} \right]^{\frac{1}{\alpha}} (1 - e^{-\frac{b\pi}{N_t \alpha}}). \quad (6.38)$$

This results can be applied to Eq. (6.8) and then into Eq. (6.7) to obtain the probability of k-connectivity.

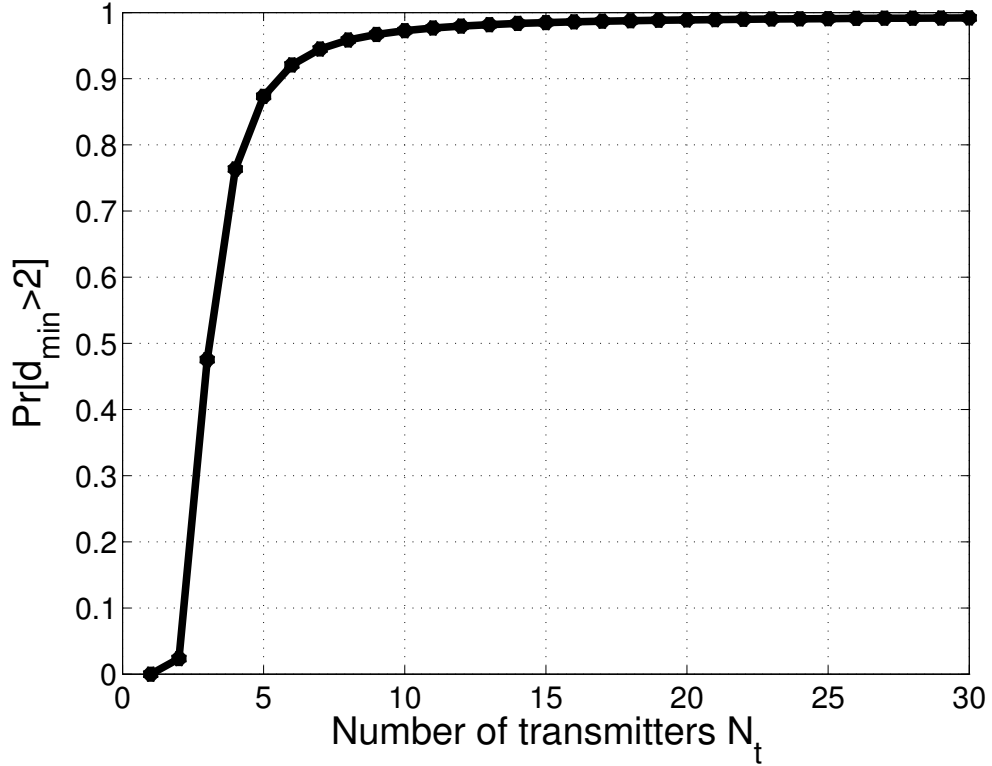


Figure 6.6: $\Pr[d_{\min} > k]$ versus N_t with OOK modulation.

Figure 6.6 shows how the probability of k-connectivity varies with the number of transmitters N_t . All the parameters used in the simulation are the same as Scenario III and λ is 0.1. The probability of k-connectivity $\Pr[d_{\min} > k]$ increases with N_t . When N_t is 1, the current scenario becomes Scenario III; meanwhile, when N_t approaches infinity, it turns to Scenario II. The above statement can be verified by comparing Figure 6.6 and Figure 6.5(b) in which $\Pr[d_{\min} > k]$ is zero and one respectively when λ equals 0.1. The above analysis provides a

guideline for transceiver and network designers to consider how to achieve a balance between k-connectivity and complexity/cost.

In the presence of rotation errors, I can model the errors properly and take a similar approach as in Scenario II to study the corresponding effect.

6.4 Summary

UV communication is a promising technology for NLOS ad hoc communication and wireless sensor networks. This chapter discussed the k-connectivity performance in UV communication networks. I emphasized the effect of multi-user interference on k-connectivity. Different system configurations were discussed and compared with each other and also the scenario without considering multi-user interference. From the results, the node density turns out to be an important design parameter. Trade-offs exist between high probability of k-connectivity and large coverage area with a constant number of nodes deployed. To achieve better performance for k-connectivity, the ability of transmitter to track the desired receiver is critical. At least, a node should be able to change the transmission direction to achieve satisfied k-connectivity performance. A more practical case was analyzed based on multi-Tx transceiver design. The effect of the number of transmitters on k-connectivity was studied. In addition, the shape of coverage area of a directional UV transmitter was presented.

Chapter 7

Conclusions

This thesis explored multiple aspects of UV communication systems and networks, including channel modeling, receiver performance evaluation, network throughput, protocol design and connectivity analysis.

In channel modeling, the research focused on developing ultraviolet path loss models in non-coplanar geometry, analytically and empirically. This is a new area because to the best of my knowledge most work in the existing literature only considers coplanar geometry which is not applicable for a multiple user scenario. The analytical model in the triple-integral form is a good candidate for link budget, and the closed-form analytical model developed greatly reduces the computation complexity and relaxes the constraint for the orientation of a receiver. The empirical non-coplanar path loss model provides a tool for system and network analysis thanks to its greatly simplified form. Meanwhile, the two analytical models are compared with a classic single scattering path loss model developed by Reilly et al and show a good match in most typical co-planar scenarios.

This thesis analyzed the performance of LED-based ultraviolet communication M-PPM receiver in delay spread channel. Due to the relatively wide transmission beam angle of com-

mercially available ultraviolet LED and scattering based propagation, inter-symbol interference introduced by channel spread is not negligible. Its effect becomes pronounced at a high data rate. However, most of the previous studies ignore the effect of inter-symbol interference. The results for the M-PPM receiver performance show the interaction among data rate, bit error rate and transmit/receive geometry.

The thesis further extended a point-to-point scenario to a multiple user case, and a UV communication network. A metric, transmission throughput, was designed to evaluate performance of an ultraviolet wireless network consisting of multiple nodes. The study incorporated newly proposed empirical path loss model and stochastic geometry theory. The lower bound of the transmission throughput was shown to be a function of node spatial density, transmission probability and signal detection threshold. Thus we are able to evaluate how these network parameters affect the network performance.

In order to connect the nodes in a network, each node should be aware of the information of its neighbors. A leadership based neighbor discovery protocol drastically shortened the time required by neighbor discovery procedure by creating an interference-free broadcast environment. This protocol could achieve the same information for each node and the nodes are able to determine when to terminate its search distributively.

The thesis fully analyzed the connectivity issues of ultraviolet communication networks in different scenarios, i.e., different transceiver structures, depending on whether each node transmitter is capable of adjusting its pointing angle and tracking a target receiver. The research is the first work to bring the multiple user interference into consideration in the study of connectivity of ultraviolet communication networks, to the best of my knowledge.

Bibliography

- [1] L. Wang, Z. Xu, and B. M. Sadler. Non-line-of-sight ultraviolet link loss in non-coplanar geometry. *Opt. Lett.*, 35(8):1263–1265, April 2010.
- [2] G. Chen, Z. Xu, H. Ding, and B. M. Sadler. Path loss modeling and performance trade-off study for short-range non-line-of-sight ultraviolet communications. *Opt. Express*, 17(5):3929–3940, March 2009.
- [3] Y. Li, L. Wang, Z. Xu, and S. V. Krishnamurthy. Neighbor discovery for ultraviolet ad hoc networks. 2011.
- [4] D. M. Reilly. Atmospheric optical communications in the middle ultraviolet. Master’s thesis, Massachusetts Institute of Technology, 1976.
- [5] D. E. Sunstein. A scatter communications link at ultraviolet frequencies. Master’s thesis, Massachusetts Institute of Technology, 1968.
- [6] M. Razeghi. Deep ultraviolet light-emitting diodes and photodetectors for uv communications. In *Proc. SPIE*, volume 5729, pages 30–40, 2005.
- [7] D. M. Reilly, D. T. Moriarty, and J. A. Maynard. Unique properties of solar blind ultraviolet communication systems for unattended ground sensor networks. In *Proc. SPIE*, 5611, pages 244–254, 2004.
- [8] Z. Xu and B. M. Sadler. Ultraviolet communications: Potential and state-of-the-art. *Communications Magazine, IEEE*, 46(5):67–73, May 2008.
- [9] G. A. Shaw, A. M. Siegel, and M. L. Nischan. Demonstration system and applications for compact wireless ultraviolet communications. In *Proc. SPIE*, volume 5071, pages 241–252, September 2003.
- [10] G. Chen, F. Abou-Galala, Z. Xu, and B. M. Sadler. Experimental evaluation of led-based solar blind nlos communication links. *Opt. Express*, 16(19):15059–15068, 2008.
- [11] J. M. Kahn and J. R. Barry. Wireless infrared communications. *Proc. IEEE*, 85:265–298, 1997.
- [12] W. O. Popoola and Z. Ghassemlooy. Bpsk subcarrier intensity modulated free-space optical communications in atmospheric turbulence. *J. Lightwave Technol.*, 27(8):967–973, 2009.

- [13] Y. Li and Z. Xu. Transmitted reference schemes for wireless optical communications. In *Prof. IEEE Globecom*, San Francisco, CA, November 2006.
- [14] M. L. B. Riediger, R. Schober, and L. Lampe. Blind detection of on-off keying for free-space optical communications. In *CCECE/CCGEI*, pages 1361–1364, Niagara Falls, Canada, 2008.
- [15] Q. He, Z. Xu, and B. M. Sadler. Performance of short-range non-line-of-sight led-based ultraviolet communication receivers. *Opt. Express*, 18(12):12226–12238, 2010.
- [16] G. A. Shaw and M. Nischan. Short-range nlos ultraviolet communication testbed and measurements. In *Proc. SPIE*, volume 4396, pages 31–40, 2001.
- [17] G. A. Shaw, M. L. Nischan, M. A. Iyengar, S. Kaushik, and M. K. Griffin. Nlos uv communication for distributed sensor systems. In *Proc. SPIE*, volume 4126, pages 83–96, 2000.
- [18] G. A. Shaw, A. M. Siegel, and J. Model. Extending the range and performance of non-line-of-sight ultraviolet communication links. In *Proc. SPIE*, volume 62310C, pages 1–12, 2006.
- [19] G. A. Shaw, A. M. Siegel, J. Model, and D. Greisokh. Recent progress in short-range ultraviolet communication. In *Proc. SPIE*, volume 5796, pages 214–225, 2005.
- [20] G. A. Shaw, A. M. Siegel, J. Model, and M. L. Nischan. Field testing and evaluation of a solar-blind uv communication link for unattended ground sensors. In *Proc. SPIE*, volume 5417, pages 250–261, 2004.
- [21] D. Kedar. Multiaccess interference in a non-line-of-sight ultraviolet optical wireless sensor network. *Appl. Opt.*, 46(23):5895–5901, 2007.
- [22] M. R. Luetngen, J. H. Shapiro, and D. M. Reilly. Non-line-of-sight single-scatter propagation model. *J. Opt. Soc. Am. A*, 8(12):1964–1972, 1991.
- [23] Z. Xu, H. Ding, B. M. Sadler, and G. Chen. Analytical performance study of solar blind non-line-of-sight ultraviolet short-range communication links. *Opt. Lett.*, 33(16):1860–1862, August 2008.
- [24] H. Ding, G. Chen, A. Majumdar, B. M. Sadler, and Z. Xu. Modeling of non-line-of-sight ultraviolet scattering channels for communication. *IEEE J. Sel. Areas Commun.*, 27(9):1535–1544, December 2009.
- [25] D. Kedar and S. Arnon. Non-line-of-sight optical wireless sensor network operating in multiscattering channel. *Appl. Opt.*, 45(33):8454–8461, November 2006.
- [26] D. T. Gillespie. Stochastic-analytic approach to the calculation of multiply scattered lidar returns. *J. Opt. Soc. Am. A*, 2(8):1307–1324, 1985.
- [27] H. Ding, G. Chen, A. K. Majumdar, and Z. Xu. A parametric single scattering channel model for non-line-of-sight ultraviolet communications. In *Proc. SPIE*, volume 7091, San Diego, CA, August 2008.
- [28] D. M. Reilly and C. Warde. Temporal characteristics of single-scatter radiation. *J. Opt. Soc. Am.*, 69(3):464–470, December 1979.

- [29] X. Zhu and J. M. Khan. Free-space optical communication through atmospheric turbulence channels. *Communications, IEEE Transactions on*, 50(8):1293–1300, Aug 2002.
- [30] G. Chen, Z. Xu, and B. M. Sadler. Experimental demonstration of ultraviolet pulse broadening in short-range non-line-of-sight communication channels. *Opt. Express*, 18(10):10500–10509, 2010.
- [31] R. M. Gagliardi and S. Karp. *Optical Communications*. New York : Wiley, 2nd edition, 1995.
- [32] J. G. Proakis and D. G. Manolakis. *Digital Signal Processing*. Upper Saddle River, N.J. : Pearson Prentice Hall, 4 edition, 2007.
- [33] D. Tse and P. Viswanath. *Fundamentals of wireless communication*. Cambridge ; New York : Cambridge University Press, 2005.
- [34] S. Karp, R. M. Gagliardi, S. E. Moran, and L. B. Scotts. *Optical Channels, Fiber, Clouds, Water and Atmosphere*. New York: Plenum, 2nd edition, 1980.
- [35] P. Gupta and P. R. Kumar. The capacity of wireless networks. *IEEE Trans. Info. Theory*, 46(2):388–404, March 2000.
- [36] E. S. Sousa and J. A. Silvester. Optimum transmission ranges in a direct-sequence spread-spectrum multihop packet radio network. *IEEE J. Sel. Areas Commun.*, 8(5):762–771, June 1990.
- [37] S. Weber, J. G. Andrews, and N. Jindal. The effect of fading, channel inversion, and threshold scheduling on ad hoc networks. *IEEE Trans. Info. Theory*, 53(11):4127–4149, November 2007.
- [38] S. Weber, J. G. Andrews, X. Yang, and G. de Veciana. Transmission capacity of wireless ad hoc networks with successive interference cancellation. *IEEE Trans. Info. Theory*, 53(8):2799–2814, August 2007.
- [39] S. Weber, X. Yang, J. G. Andrews, and G. de Veciana. Transmission capacity of wireless ad hoc networks with outage constraints. *IEEE Trans. Info. Theory*, 51(12):4091–4102, December 2005.
- [40] D. Stoyan, W. Kendall, and J. Mecke. *Stochastic Geometry and Its Applications*. John Wiley and Sons, 2 edition, 1996.
- [41] R. K. Ganti and M. Haenggi. Interference and outage in clustered wireless ad hoc networks. *IEEE Trans. Info. Theory*, 55(9):4067–4086, September 2009.
- [42] A. Leon-Garcia. *Probability and Random Processes for Electrical Engineering*. Addison Wesley, 2nd edition, 1994.
- [43] L. Wang, Y. Li, Z. Xu, and S. V. Krishnamurthy. A novel neighbor discovery protocol for ultraviolet wireless networks. In *Proc. ACM MSWiM*, Miami, Florida, USA, November 2011.
- [44] S. Vasudevan, J. Kurose, and D. Towsley. On neighbor discovery in wireless networks with directional antennas. In *IEEE INFOCOM*, March 2005.

- [45] G. Pei, M. Albuquerque, J. Kim, D. Nast, and P. Norris. A neighbor discovery protocol for directional antenna networks. In *MILCOM*, October 2005.
- [46] J. Luo and D. Guo. Neighbor discovery in wireless ad hoc networks based on group testing. In *46th Annual Allerton Conf.*, September 2008.
- [47] M. J. McGlynn and S. A. Borbash. Birthday protocols for low energy deployment and flexible neighbor discovery in ad hoc wireless networks. In *Mobihoc*, September 2001.
- [48] G. Jakllari, W. Luo, and S. V. Krishnamurthy. An integrated neighbor discovery and mac protocol for ad hoc networks using directional antennas. *IEEE Trans. on Wireless Communications*, 6(3):1–12, March 2007.
- [49] S. Vasudevan, D. Towsley, R. Khalili, and D. Goeckel. Neighbor discovery in wireless networks and the coupon collector’s problem. In *ACM Mobicom*, 2009.
- [50] Y. Li, J. Ning, Z. Xu, S. V. Krishnamurthy, and G. Chen. Uvoc-mac: A mac protocol for outdoor ultraviolet networks. In *18th IEEE International Conference on Network Protocols (ICNP 2010)*, Kyoto, Japan, October 2010.
- [51] OPNET User’s Documentation. <http://www.opnet.com>.
- [52] IEEE Std 802.11 2007. Wireless LAN medium access control (MAC) and physical layer (PHY) specifications. <http://standards.ieee.org/getieee802/download/802.11-2007.pdf>.
- [53] L. Wang, Y. Li, and Z. Xu. On connectivity of wireless ultraviolet networks. *J. Opt. Soc. Am. A*, 2011.
- [54] X. Wang, G. Xing, Y. Zhang, C. Lu, R. Pless, and C. Gill. Integrated coverage and connectivity configuration in wireless sensor networks. In *ACM SenSys*, Los Angeles, CA, November 2003.
- [55] A. Vavoulas, H. G. Sandalidis, and D. Varoutas. Connectivity issues for ultraviolet uv-c networks. *J. Opt. Commun. Netw.*, 3(3):199–205, March 2011.
- [56] C. Bettstetter. On the connectivity of wireless multihop networks with homogeneous and inhomogeneous range assignment. In *Proc. of IEEE VTC Fall*, Vancouver, BC, Canada, September 2002.
- [57] C. Bettstetter. On the minimum node degree and connectivity of a wireless multihop networks. In *Proc. ACM MobiHoc*, Lausanne, Switzerland, June 2002.
- [58] D. Miorandi and E. Altman. Coverage and connectivity of ad hoc networks in presence of channel randomness. In *Proc. of IEEE INFOCOM*, Miami, FL, March 2005.
- [59] M. D. Penrose. On k-connectivity for a geometric random graph. *Rand. Struct. Alg.*, 15(2):145–164, September 1999.
- [60] L. Zhang, B. H. Soong, Y. Zhang, M. Ma, and Y. Guan. An analysis of k-connectivity in shadowing and nakagami fading wireless multi-hop networks. In *Proc. of IEEE VTC Spring*, Singapore, May 2008.
- [61] M. A. Elshimy and S. Hranilovic. Non-line-of-sight single-scatter propagation model for noncoplanar geometries. *J. Opt. Soc. Am. A*, 28(3):420–428, March 2011.

- [62] H. Ding, Z. Xu, and B. M. Sadler. A path loss model for non-line-of-sight ultraviolet multiple scattering channels. *EURASIP: Special Issue on Optical Wireless Communications and Networking*, 2010.
- [63] L. Wang, Y. Li, Z. Xu, and B. M. Sadler. Wireless ultraviolet network models and performance in noncoplanar geometry. In *IEEE Globecom Workshop on Optical Wireless Communications*, Miami, FL, December 2010.
- [64] L. Wang, Z. Xu, and B. M. Sadler. An approximate closed-form link loss model for non-line-of-sight ultraviolet communication in non-coplanar geometry. *Optics Letters*, 36(7):1224–1226, April 2011.
- [65] Q. He, B. M. Sadler, and Z. Xu. Modulation and coding tradeoffs for non-line-of-sight ultraviolet communications. In *Proc. of SPIE Photonics and Optics - Free Space Laser Communications IX*, San Diego, CA, August 2009.
- [66] M. D. Audeh, J. M. Kahn, and J. R. Barry. Decision-feedback equalization of pulse-position modulation on measured nondirected indoor infrared channels. *IEEE Trans. Commun.*, 47(4), June 1999.
- [67] M. D. Audeh, J. M. Kahn, and J. R. Barry. Performance of pulse-position modulation on measured non-directed indoor infrared channels. *IEEE Trans. Commun.*, 44:654–659, 1996.
- [68] V. Cellini and G. Donati. A novel multi-user interference statistics estimator for uwb-ir based on gaussian mixture model. In *Proc. Int. IST Summit*, Dresden, Germany, June 2005.
- [69] I. B. Djordjevic, S. Denic, J. Anguita, B. Vasic, and M. A. Neifeld. Ldpc-coded mimo optical communication over the atmospheric turbulence channel. *J. Lightwave Technol.*, 26(5):478–487, 2008.
- [70] Q. He, B. M. Sadler, and Z. Xu. Modulation and coding tradeoffs for non-line-of-sight ultraviolet communications. In Arun K. Majumdar and Christopher C. Davis, editors, *Proc. SPIE*, volume 7464, page 74640H, San Diego, CA, USA, 2009. SPIE.
- [71] B. Hu and N. C. Beaulieu. On characterizing multiple access interference in th-uwb systems with impulsive noise models. In *Proc. IEEE Radio and Wireless Symp.*, pages 879–882, Orlando, FL, January 2008.
- [72] T. Komine, J. H. Lee, S. Haruyama, and M. Nakagawa. Adaptive equalization system for visible light wireless communication utilizing multiple white led lighting equipment. *IEEE Trans. Wireless Commun.*, 8(6):2892–2900, June 2009.
- [73] W.O. Popoola, Z. Ghassemlooy, J.I.H. Allen, E. Leitgeb, and S. Gao. Free-space optical communication employing subcarrier modulation and spatial diversity in atmospheric turbulence channel. *IET Optoelectronics*, 2(1):16–23, 2008.
- [74] G. Prati and R. M. Gagliardi. Decoding with stretched pulses in laser ppm communications. *IEEE Trans. Commun.*, 31:1037–1045, September 1983.
- [75] M. K. Simon and V. A. Vilnrotter. Alamouti-type space-time coding for free-space optical communication with direct detection. *IEEE Trans. Wireless Commun.*, 4(1):35–39, January 2005.

- [76] X. Zhu, J.M. Kahn, and J. Wang. Mitigation of turbulence-induced scintillation noise in free-space optical links using temporal-domain detection techniques. *Photonics Technology Letters, IEEE*, 15(4):623–625, 2003.
- [77] J. G. Proakis. *Digital Communications*. New York : McGraw-Hill, Inc., 4ed edition, 2001.
- [78] D. Kedar and S. Arnon. Backscattering-induced crosstalk in wdm optical wireless communication. *IEEE/OSA J. Lightw. Technol.*, 35(8):2023–2030, June 2005.
- [79] G. Jakllari, W. Luo, and S. V. Krishnamurthy. An integrated neighbor discovery and MAC protocol for ad hoc networks using directional antennas. *IEEE Trans. on Wireless Communications*, 6(3), 2007.